

## Review

# A Review of physics-based and data-driven models for real-time control of polymer electrolyte membrane fuel cells

Jian Zhao <sup>a</sup>, Xianguo Li <sup>a,\*</sup>, Chris Shum <sup>b</sup>, John McPhee <sup>b</sup>

<sup>a</sup> Department of Mechanical and Mechatronics Engineering, University of Waterloo, Waterloo, Ontario, Canada

<sup>b</sup> Department of Systems Design Engineering, University of Waterloo, Waterloo, Ontario, Canada



## HIGHLIGHTS

- Reviewed control-oriented PEMFC models with high computing speed and accuracy.
- Compared 1D physical models by incorporating transport & electrochemical phenomena.
- Examined 0D analytical & empirical models with low computing resource requirements.
- Scrutinized data-driven models with AI algorithms for real-time control.

## ARTICLE INFO

## Keywords:

Polymer electrolyte membrane fuel cell  
 Physics-based model  
 Real-time control  
 Reduced dimensionality  
 Empirical model  
 Data-driven model  
 Artificial intelligence

## ABSTRACT

The real-time model-based control of polymer electrolyte membrane (PEM) fuel cells requires a computationally efficient and sufficiently accurate model to predict the transient and long-term performance under various operational conditions, involving the pressure, temperature, humidity, and stoichiometry ratio. In this article, recent progress on the development of PEM fuel cell models that can be used for real-time control is reviewed. The major operational principles of PEM fuel cells and the associated mathematical description of the transport and electrochemical phenomena are described. The reduced-dimensional physics-based models (pseudo-two-dimensional, one-dimensional numerical and zero dimensional analytical models) and the non-physics-based models (zero-dimensional empirical and data-driven models) have been systematically examined, and the comparison of these models has been performed. It is found that the current trends for the real-time control models are (i) to couple the single cell model with balance of plants to investigate the system performance, (ii) to incorporate aging effects to enable long-term performance prediction, (iii) to increase the computational speed (especially for one-dimensional numerical models), and (iv) to develop data-driven models with artificial intelligence/machine learning algorithms. This review will be beneficial for the development of physics or non-physics based models with sufficient accuracy and computational speed to ensure the real-time control of PEM fuel cells.

## 1. Introduction

The polymer electrolyte membrane (PEM) fuel cell has reached its early stage of commercialization in vehicular, portable, and stationary applications due to its advantageous features such as low gas emission, quiet operation, fast load response, and high energy conversion efficiency [1–3]. Significant efforts have been devoted to developing PEM fuel cells with reduced cost, improved performance, and increased durability, which remain the three major technical challenges to its successful commercialization [4,5]. PEM fuel cells are extensively

studied through experimental and modeling approaches. The experimental approach is costly, time-consuming, and skill-dependent. For instance, a target lifetime of 40,000 h [6] set by the U.S. Department of Energy (DOE) for stationary fuel cells by 2020 requires around 4.6 years of non-stop operations, while for vehicles, the target lifetime of 25,000 h for buses requires over 3.4 years of testing by running the fuel cell buses (275 kW) 20 h every day with the fuel cost of USD \$800,000 at the hydrogen price of USD \$4/kg [7].

Numerical modeling has been demonstrated to be a useful alternative to experiments for the fuel cell studies in various ways, e.g., understanding physical phenomena that are difficult or expensive to be

\* Corresponding author.

E-mail address: [Xianguo.Li@uwaterloo.ca](mailto:Xianguo.Li@uwaterloo.ca) (X. Li).

<https://doi.org/10.1016/j.egyai.2021.100114>

Received 20 May 2021; Received in revised form 6 September 2021; Accepted 7 September 2021

Available online 9 September 2021

2666-5468/© 2021 The Authors.

Published by Elsevier Ltd.

This is an open access article under the CC BY-NC-ND license

(<http://creativecommons.org/licenses/by-nc-nd/4.0/>).

Nomenclature			
$a$	water activity	$\lambda$	water content in ionomer
$A$	area [ $\text{m}^2$ ]	$\mu$	dynamic viscosity [ $\text{N}\cdot\text{s}\cdot\text{m}^{-2}$ ]
$c$	molar concentration [ $\text{kmol}\cdot\text{m}^{-3}$ ]	$\nu$	kinetic viscosity [ $\text{m}^2\cdot\text{s}^{-1}$ ]
$C$	electric capacity [ $\text{F}\cdot\text{m}^{-2}$ ]	$\rho$	density [ $\text{kg}\cdot\text{m}^{-3}$ ]
$c_p$	specific heat [ $\text{J}\cdot\text{kg}^{-1}\cdot\text{K}$ ]	$\sigma$	surface tension [ $\text{N}\cdot\text{m}^{-1}$ ]
$d$	pore diameter or characteristic length of water diffusion [m]	$\tau$	tortuosity
$D$	mass diffusivity [ $\text{m}^2\cdot\text{s}^{-1}$ ]	$\varphi$	potential [V]
$EW$	equivalent weight of membrane [ $\text{kg}\cdot\text{kmol}^{-1}$ ]	$\Phi$	volume fraction
$f$	interfacial drag coefficient	$\omega$	volume fraction of ionomer in catalyst layer
$F$	Faraday's constant [ $\text{C}\cdot\text{kmol}^{-1}$ ]	<i>Subscripts</i>	
$g$	Gibbs function of formation [ $\text{J}\cdot\text{kmol}^{-1}$ ]	a	anode
$h$	latent heat [ $\text{J}\cdot\text{kg}^{-1}$ ]	act	activation
$i$	current density [ $\text{A}\cdot\text{cm}^{-2}$ ]	ave	average
$j$	volumetric reaction rate [ $\text{A}\cdot\text{m}^{-3}$ ]	c	cathode
$j_0$	volumetric exchange current density [ $\text{A}\cdot\text{m}^{-3}$ ]	ca	capillary
$J$	mass flux [ $\text{kg}\cdot\text{m}^{-2}\cdot\text{s}^{-1}$ ]	cl	catalyst layer
$k$	thermal conductivity [ $\text{W}\cdot\text{m}^{-1}\cdot\text{K}^{-1}$ ]	cond	condensation
$K$	permeability [ $\text{m}^2$ ]	conv	convection
$\dot{m}$	mass flow rate [ $\text{kg}\cdot\text{s}^{-1}$ ]	d	dissolved water
$M$	molecular weight [ $\text{kg}\cdot\text{kmol}^{-1}$ ]	diff	diffusion
$n_d$	electro-osmotic drag coefficient ( $\text{H}_2\text{O}$ per $\text{H}^+$ )	d-l	dissolved water to liquid
$p$	pressure [Pa]	d-v	dissolved water to vapor
$R$	universal gas constant = 8314 [ $\text{J}\cdot\text{kmol}^{-1}\cdot\text{K}^{-1}$ ]	eff	effective
$RH$	relative humidity	ele	electronic
$s$	entropy [ $\text{J}\cdot\text{kmol}^{-1}\cdot\text{K}^{-1}$ ]	eod	electro-osmotic drag
$S$	source terms in governing equations	equil	equilibrium
$S_{pc}$	latent heat function for water phase change [ $\text{W}\cdot\text{m}^{-3}$ ]	evap	evaporation
$S_h$	dimensionless phase transfer rates of condensation and evaporation	fl	fluid phase
$T$	temperature [K]	g	gas phase
$T_0$	operation temperature [K]	gdl	gas diffusion layer
$u$	superficial velocity [ $\text{m}\cdot\text{s}^{-1}$ ]	$\text{H}_2$	hydrogen
$V$	electrical potential [V]	$\text{H}_2\text{O}$	water
$X$	mole fraction	$i, j$	the $i^{\text{th}}$ and $j^{\text{th}}$ components
$Y$	mass fraction	in	inlet
<i>Greek Letters</i>		ion	ionic
$\alpha$	transfer coefficient	l	liquid water
$\beta$	diffusibility (defined as the effective diffusivity over bulk diffusivity)	m	mass (for source term)
$\delta$	thickness [m]	mem	membrane
$\epsilon$	porosity	$\text{O}_2$	oxygen
$\zeta$	water transfer rate [ $\text{s}^{-1}$ ]	out	outlet
$\eta$	over potential [V]	ref	reference state
$\theta$	contact angle [ $^\circ$ ]	rev	reversible
$\kappa$	electrical conductivity [ $\text{S}\cdot\text{m}^{-1}$ ]	sat	saturation
		sl	solid phase
		T	energy (for source term)
		u	momentum (for source term)
		v	water vapor
		v-l	vapor to water liquid

captured by experimental techniques [4,8] and providing the basis of the control and diagnosis strategies for PEM fuel cells [9,10]. The actual PEM fuel cell operation involves complex transport phenomena of neutral species (e.g., hydrogen, air, vapor and liquid water), charged species (e.g., electron and ion) and thermal energy within a multiscale region (e.g., flow channels with the dimensions from a few millimeters to tens of centimeters and porous media with length scales of nanometers and micrometers), which makes it challenging to accurately predict the output performance and precisely control the operation in a real-time environment. For a stable, efficient, and robust operation of PEM fuel cells, it is necessary to effectively control the reactant supply, water management, humidification, cooling and power electronic subsystems [9]. Many control strategies have been employed for PEM fuel cells,

including proportional integral derivative (PID) control, adaptive control, and model predictive control [9,11–13]. PID can be implemented by manipulating different operating conditions (e.g., stoichiometry ratio, pressure, and temperature) via classic feedback or feed forward control strategies. Although the implementation of PID is simple and cost effective, the slow, inaccurate, and offset issues as well as the non-linear and complicated fuel cell dynamics require more advanced control strategies to achieved optimal performance of fuel cells. Adaptive control can be implemented in a PID controller, which allows the systems to modify its operating conditions and maintain optimal performance with sensor signals. In the model predictive control, fuel cell models can be implemented to update the control action of various operational variables by comparing the actual and predicted output

variables. The model predictive control is suitable to achieve optimal performance and to avoid harmful operating conditions [9].

An accurate and computationally efficient control-oriented model is the core of the real-time model-based control of fuel cell systems. Various empirical models, analytical models, and non-physics-based models are extensively studied in literature [14–31]; however, due to various simplifications, these models are challenged to estimate the fuel cell performance over the entire range of operation. To achieve high prediction accuracy for the entire operational range, a large database is needed for model validation, modification, and calibration. However, the PEM fuel cell performance may vary significantly depending on the design and manufacturing processes, and different fuel cell developers would obtain different performance data for the seemingly similar fuel cells they make and test, which are often kept confidential. As a result, there are no benchmark experimental data for PEM fuel cells available in the open literature. Therefore, the models developed in literature are typically compared with a particular set of experimental data with limited information available on how the data were measured for what details of the particular cell [14–31]. This state of the art in the field forced the present review to be focused on the models that are potentially useful for the control purpose at the qualitative rather than quantitative anchoring to any type of data or evidence.

The physical and electrochemical phenomena within the PEM fuel cell components are complicated with multi-facets. A typical PEM fuel cell consists of a membrane, two catalyst layers (CLs), two gas diffusion layers (GDLs, with each GDL composed of a microporous layer and a macro-porous substrate layer, e.g., carbon fibre paper or cloth), two flow channels, and two bipolar plates (a.k.a. flow field or distribution plates) [32], as presented in Fig. 1. The pressurized hydrogen fuel in manifolds is supplied to anode flow channels and arrived at the anode CLs through

anode GDLs. In the anode CL, hydrogen gas is transported in void regions, diffused in ionomers, and finally adsorbed on the catalyst surface, where hydrogen is oxidized into protons and electrons. The protons pass through the membrane and arrive at the cathode CL. The electrons travel in the opposite direction through anode GDLs, anode distribution plates, external circuits, cathode distribution plates, and cathode GDLs, and finally arrive at the cathode CLs. In cathode CLs, the protons and electrons are combined with supplied oxygen gas (passing through void regions of flow channels and cathode electrodes as well as the ionomer film covered on the catalyst surface), simultaneously producing water and heat. The complex gas reactant transport, water and heat management, electrochemical reactions, as well as the transport of charged species are challenging for modeling over the entire fuel cell operational range.

Significant efforts have been devoted to the development of physics-based and non-physics-based (or data-driven) models aiming to accurately predict the fuel cell performance. These models can be classified based on spatial dimensions into three-dimensional (3D), pseudo-3D, two-dimensional (2D), pseudo-2D, one-dimensional (1D), and zero-dimensional (0D) models. 3D and pseudo-3D models consider the fuel cells in all directions [8,33–35], which requires fewer assumptions with high fidelity. However, the 3D and pseudo-3D models are computationally expensive depending on the meshes, accuracies and numbers of governing equations applied to the computational domain [8,36–38]. To minimize the computing cost but maintain the ability to analyze the physical and electrochemical phenomena, 2D models are often applied by ignoring the transport phenomena in the direction along or transverse to the channel [39–44]. However, 2D models are theoretically less accurate than 3D models and not fast enough for real-time control purposes. Many studies further decouple one spatial dimension from the other to accelerate the computing speed, which is known as the pseudo-2D model [45,46]. By considering only the through-the-membrane direction, 1D models can further reduce the computational time for real-time control but retain the majority of the physics-based phenomena [10,14,45–56]. 0D analytical or empirical correlation models can be used in model predictive control due to their fast computation speed. However, owing to the limited experimental data availability, these models are often validated under a narrow range of operational conditions; therefore, these models are questionable when utilized for the performance prediction over the entire operational range. To overcome this barrier, many advanced data-driven models including statistical and artificial-intelligent models [17,57,58] have been incorporated in the control-oriented model development. As a result, the simplified PEM fuel cell models, with reduced spatial dimensionality under various simplifications for real-time control purposes, have gained considerable research interest as the PEM fuel cell is being commercialized. It should be pointed out that the computational speed of a specific PEM fuel cell model can be further enhanced by many tools, such as reduced-order modeling, efficient numerical calculation, and code and algorithm optimization, which are excluded in this review due to limited information availability.

Although 3D and 2D models have demonstrated excellent capabilities of performance prediction and comprehension of local transport and electrochemical phenomena, these models usually involve a long iteration with a large number of meshes to achieve acceptable simulation accuracy, which makes the computation usually very expensive and unsuitable for real-time control applications to meet actual computing resource limitations. Therefore, 3D and 2D fuel cell models are excluded from this review. In this article, recent progress on the modeling techniques for the real-time control of PEM fuel cells is reviewed. The physical and electrochemical phenomena in PEM fuel cells as well as their mathematical formulation and length and time scales are discussed in Section 2. Pseudo-2D numerical models that combine the flow channel and single-cell models are reviewed in Section 3. 1D numerical models that involve the transport phenomena and electrochemical reactions are scrutinized in Section 4. 0D analytical models with simplified

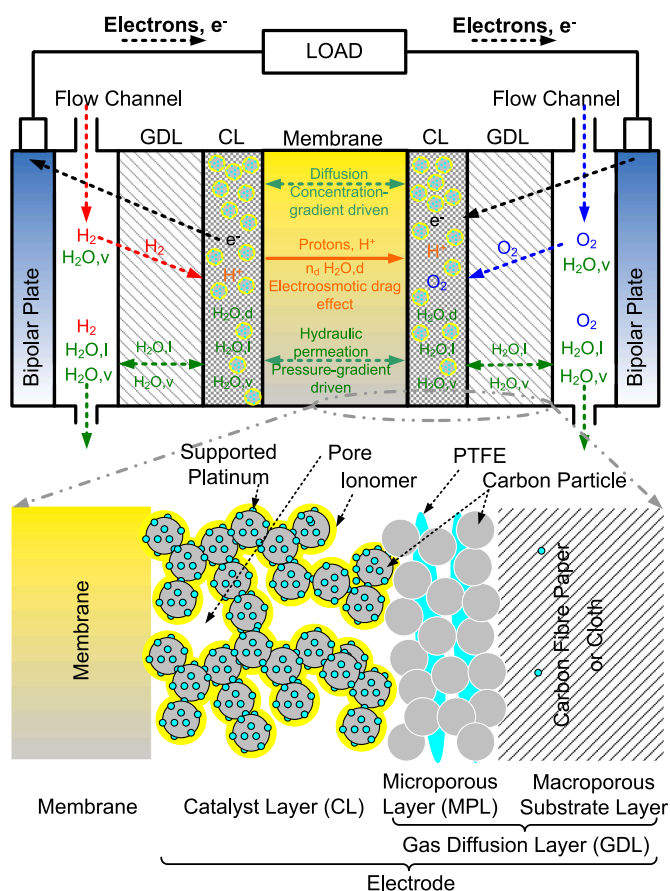


Fig. 1. Schematic of PEM fuel cell components and transport phenomena. Image not to scale.

conservation laws are reviewed in Section 5, followed by OD empirical models in Section 6. OD data-driven models with a focus on machine learning and artificial intelligence are examined in Section 7. A comparison of various fuel cell models in terms of accuracy and computing speed is conducted in Section 8. The challenges and future prospects of control-oriented fuel cell models are discussed in Section 9. Finally, a summary of these control-oriented PEM fuel cell models is given in Section 10.

## 2. Mathematical description of transport and electrochemical phenomena

Recent research interests have been directed to the control of PEM fuel cell stacks and systems for further optimization of the fuel cell operation in terms of energy efficiency, reliability, and durability. This new focus has led to an urgent need for PEM fuel cell models with high computational speed and sufficient prediction accuracy. A high-fidelity PEM fuel cell model should take the balance equations for state variables based on conservation of mass, momentum, energy, and elements (or species), as well as the electrochemical reaction kinetics into account. Therefore, a comprehensive and critical review of the vital physico-chemical phenomena and the corresponding mathematical description is conducted in this section, including the conservation and transport of mass, momentum, energy, gas species, liquid water, dissolved water, and charged species, as well as the electrochemical reaction kinetics and cell potential. Finally, the length and time scales of the key transport phenomena are discussed in this section.

### 2.1. Conservation and transport of mass

The gas reactants and products in a PEM fuel cell system follow the law of mass conservation. In flow channels, the gas flow is dominated by convection along the channel direction driven by the pressure gradient [59,60]. In electrodes, the gas mixture is transported via convection and diffusion due to the gradients of pressure and species concentration [8].

The mass conservation in PEM fuel cells is governed by the continuity equation with a source term representing the mass change due to reactions or phase changes [61–64],

$$\frac{\partial}{\partial t} [\varepsilon(1 - \Phi_l)\rho_g] + \nabla \cdot (\rho_g \vec{u}_g) = S_m \quad (1)$$

**Table 1**  
Source terms in the governing equations.

Cell Component	Source terms	$S_0$ ( $\text{kg}\cdot\text{m}^{-3}\cdot\text{s}^{-2}$ )	$S_T$ ( $\text{W}\cdot\text{m}^{-3}$ )	$S_i$ ( $\text{kg}\cdot\text{m}^{-3}\cdot\text{s}^{-1}$ )	$S_l$ ( $\text{kg}\cdot\text{m}^{-3}\cdot\text{s}^{-1}$ )	$S_d$ ( $\text{kg}\cdot\text{m}^{-3}\cdot\text{s}^{-1}$ )	$S_{ele}$ ( $\text{A}\cdot\text{m}^{-3}$ )	$S_{ion}$ ( $\text{A}\cdot\text{m}^{-3}$ )
Distribution plate	0	0	$\ \nabla\varphi_{ele}\ ^2\kappa_{ele}^{eff}$	0	0	0	0	0
Channel	$-S_{v-1}$	0	$S_{pc}$	$S_v = -S_{v-1}$	0	0	0	0
GDL	$-S_{v-1}$	$-\frac{\mu_g}{K_g}\vec{u}_g$	$\ \nabla\varphi_{ele}\ ^2\kappa_{ele}^{eff} + S_{pc}$	$S_v = -S_{v-1}$	$S_{v-1}$	0	0	0
Anode CL	$-\frac{j_a}{2F}M_{H_2} + S_{d-v} - S_{v-1}$	$-\frac{\mu_g}{K_g}\vec{u}_g$	$-\frac{j_a T \Delta s}{2F} + j_a \eta_{act} + \ \nabla\varphi_{ele}\ ^2\kappa_{ele}^{eff} + \ \nabla\varphi_{ion}\ ^2\kappa_{ion}^{eff} + S_{pc}$	$S_{H_2} = \frac{j_a}{2F}M_{H_2}$ $S_v = S_{d-v} - S_{v-1}$	$S_{v-1} + S_{d-1}$	$-S_{d-v} - S_{d-1}$	$-j_a$	$j_a$
Cathode CL	$-\frac{j_c}{4F}M_{O_2} + S_{d-v} - S_{v-1}$	$-\frac{\mu_g}{K_g}\vec{u}_g$	$-\frac{j_c T \Delta s}{4F} + j_c \eta_{act} + S_{pc} + \ \nabla\varphi_{ele}\ ^2\kappa_{ele}^{eff} + \ \nabla\varphi_{ion}\ ^2\kappa_{ion}^{eff}$	$S_{O_2} = -\frac{j_c}{4F}M_{O_2}$ $S_v = S_{d-v} - S_{v-1}$	$S_{v-1} + S_{d-1}$	$\frac{j_c}{2F}M_{H_2O} - S_{d-v} - S_{d-1}$	$j_c$	$-j_c$
Membrane	0	0	$\ \nabla\varphi_{ion}\ ^2\kappa_{ion}^{eff}$	0	0	0	0	0

Note:  $S_{v-1}$ ,  $S_{d-v}$  and  $S_{d-1}$  are water vapor-to-liquid phase, dissolved-water-to-vapor, and dissolved-water-to-liquid phase change rates in [ $\text{kg}\cdot\text{m}^{-3}\cdot\text{s}^{-1}$ ], respectively;  $j_a$  and  $j_c$  are the anodic and cathodic reaction rates per unit volume in [ $\text{A}\cdot\text{m}^{-3}$ ], respectively;  $M$  denotes the molecular weight in [ $\text{kg}\cdot\text{kmol}^{-1}$ ];  $F$  represents the Faraday's constant in [ $\text{C}\cdot\text{kmol}^{-1}$ ];  $\mu_g$  denotes the dynamic viscosity of gas mixture in [ $\text{N}\cdot\text{s}\cdot\text{m}^{-2}$ ];  $\vec{u}_g$  is the superficial velocity in [ $\text{m}\cdot\text{s}^{-1}$ ];  $K_g$  is the permeability of gas phase in [ $\text{m}^2$ ] in the electrodes;  $\varphi_{ele}$  and  $\varphi_{ion}$  are the electric potentials of the electron- and ion-conducting phases in [V];  $\kappa_{ele}^{eff}$  and  $\kappa_{ion}^{eff}$  represent effective electrical conductivity of the corresponding phases taking the pore structure into account in [ $\text{S}\cdot\text{m}^{-1}$ ];  $S_{pc}$  is the latent heat function for phase changes of water in [ $\text{W}\cdot\text{m}^{-3}$ ];  $\eta_{act}$  denotes the activation overpotential in [V];  $T$  is the temperature in [K];  $\Delta s$  denotes the entropy change of reaction in [ $\text{J}\cdot\text{kmol}^{-1}\cdot\text{K}^{-1}$ ]; and  $S_v$ ,  $S_{H_2}$  and  $S_{O_2}$  denote the volumetric mass generation rates in [ $\text{kg}\cdot\text{m}^{-3}\cdot\text{s}^{-1}$ ] of water vapor, hydrogen, and oxygen gases, respectively.

where  $\varepsilon$  is the porosity;  $\Phi_l$  is the volumetric fraction of liquid in the void regions;  $\rho$  is the density in [ $\text{kg}\cdot\text{m}^{-3}$ ];  $u$  means the superficial velocity in [ $\text{m}\cdot\text{s}^{-1}$ ]; the subscript  $g$  represents the gas mixture; and  $S_m$  is the source term in [ $\text{kg}\cdot\text{m}^{-3}\cdot\text{s}^{-1}$ ]. The first term denotes the transient mass accumulation taking the porosity and liquid water into account based on the volume-average method, while the second term is the volumetric mass change rate of the gas mixture due to convection. The source terms represent the gas-phase mass change due to phase change or electrochemical reaction. Detailed mathematical description of the source terms in different cell components is indicated in Table 1.

In flow channels and electrodes, the mass of vapor varies due to condensation or evaporation [35,62]. The vapor-to-liquid phase change rate,  $S_{v-1}$  [ $\text{kg}\cdot\text{m}^{-3}\cdot\text{s}^{-1}$ ], can be calculated as follows [36,61,65,66].

$$S_{v-1} = \begin{cases} \gamma_{cond}\varepsilon(1 - \Phi_l)(\rho_v - \rho_{sat}), & \text{if } \rho_v \geq \rho_{sat} \\ \gamma_{evap}\varepsilon\Phi_l(\rho_v - \rho_{sat}), & \text{if } \rho_v < \rho_{sat} \end{cases} \quad (2)$$

where  $\gamma_{cond}$  and  $\gamma_{evap}$  denote the rates of condensation and evaporation (typically  $1.0\text{--}10^4 \text{ s}^{-1}$  [61,65,66]), respectively;  $\varepsilon$  is the porosity;  $\Phi_l$  is the volumetric fraction of liquid in the void regions; and  $\rho_v$  and  $\rho_{sat}$  are the actual and saturated vapor density in [ $\text{kg}\cdot\text{m}^{-3}$ ], respectively. If the actual vapor density is larger than the saturated value, the excess water vapor condenses, and the rate of condensation is affected by the effective pore volume (excluding liquid water volume); Otherwise, evaporation takes place when liquid water pre-exists, and the rate of evaporation is affected by the liquid volume in the pores.

In CLs, when the dissolved water content in CLs is larger than the equilibrium value, dissolved water can be transferred to vapor, and vice versa [67,68]. The dissolved-water-to-vapor phase change in the void regions of CLs,  $S_{d-v}$  [ $\text{kg}\cdot\text{m}^{-3}\cdot\text{s}^{-1}$ ], can be calculated from [8,61,67,69],

$$S_{d-v} = \zeta_{d-v} \frac{\rho_{mem} M_{H_2O}}{EW} (\lambda_d - \lambda_{eq}) \quad (3)$$

where  $\zeta_{d-v}$  is the rate of phase change between dissolved water and vapor in [ $\text{s}^{-1}$ ];  $\rho_{mem}$  is the membrane density in [ $\text{kg}\cdot\text{m}^{-3}$ ];  $M_{H_2O}$  is the molecular weight of water in [ $\text{kg}\cdot\text{kmol}^{-1}$ ];  $EW$  denotes the equivalent weight of membrane in [ $\text{kg}\cdot\text{kmol}(\text{SO}_3\text{H})^{-1}$ ], representing the weight of dry membrane per kmol of ionic group; and  $\lambda_d$  and  $\lambda_{eq}$  are the actual and equilibrium dissolved water content in ionomer in [ $\text{kmol}(\text{H}_2\text{O})\cdot\text{kmol}(\text{SO}_3\text{H})^{-1}$ ], respectively.  $\lambda_{eq}$  can be calculated by an empirical correlation derived by [70] based on the experimental data on the water uptake of various membranes, such as Nafion, Aciplex, and Flemion [71].

$$\frac{\partial}{\partial t} \left[ \frac{\rho_g \vec{u}_g}{\varepsilon(1-\Phi_l)} \right] + \nabla \cdot \left( \frac{\rho_g \vec{u}_g \vec{u}_g}{\varepsilon^2(1-\Phi_l)^2} \right) = -\nabla p_g + \left\{ \mu_g \nabla \cdot \left[ \nabla \left( \frac{\vec{u}_g}{\varepsilon(1-\Phi_l)} \right) + \left[ \nabla \left( \frac{\vec{u}_g}{\varepsilon(1-\Phi_l)} \right) \right]^T \right] - \frac{2}{3} \mu_g \nabla \left[ \nabla \cdot \left( \frac{\vec{u}_g}{\varepsilon(1-\Phi_l)} \right) \right] \right\} + S_u \quad (6)$$

$$\lambda_{eq} = 0.3 + 6a[1 - \tanh(a - 0.5)] + 3.9\sqrt{a} \left[ 1 + \tanh\left(\frac{a - 0.89}{0.23}\right) \right] \quad (4)$$

where  $a$  represents the water activity, which is defined as [44,72]

$$a = \frac{X_v p_g}{p_{sat}} \quad (5)$$

where  $X_v$  is the molar fraction of water vapor in the gas mixture, and  $p_g$  and  $p_{sat}$  are the actual and saturated vapor partial pressure in [Pa], respectively.

It should be noted that the vapor and liquid water can become ice under certain circumstances, especially during the cold start of PEM fuel cells [64,73,74]; however, the formation of ice is not taken into account in most reduced-dimension models, which are excluded in this article. In addition, the membrane is often assumed impermeable to gas due to neglected pore size and volume when the gas crossover is insignificant, which is the case under the operating conditions.

## 2.2. Conservation and transport of momentum

The conservation of momentum, a.k.a. the Navier-Stokes equation, is modified based on the volume-average approach with superficial velocity for flows in porous media in fuel cell modeling. The Navier-Stokes equation is established based on Newton's second law of mechanics, describing the effect of body forces (such as gravitational, electric, or magnetic forces) and surface forces (such as pressure and viscous stresses) on the flow velocity [8,61]. The gas flow in the electrodes can be affected by the fluid-solid interaction in the complicated pore structure. The fluid-solid interaction is macroscopically expressed by Darcy's law, by which the relation of gas mixture velocity and the flow resistance across the porous media can be quantified [75–77].

The conservation of momentum is expressed by the following equation [61,64,78],

where  $\rho_g$  is the density of gas mixture in [ $\text{kg}\cdot\text{m}^{-3}$ ];  $p_g$  is the pressure in [Pa];  $\mu_g$  is the dynamic viscosity of gas mixture in [ $\text{N}\cdot\text{s}\cdot\text{m}^{-2}$ ];  $\vec{u}_g$  is the superficial velocity in [ $\text{m}\cdot\text{s}^{-1}$ ];  $\varepsilon$  is the porosity;  $\Phi_l$  is the volumetric fraction of liquid in the void regions; and  $S_u$  represents the source term due to Darcy's effect in [ $\text{kg}\cdot\text{m}^{-2}\cdot\text{s}^{-2}$ ]. The transient term denotes the volumetric accumulation rate of momentum, while the second term represents the net momentum increase due to convection. The first term on the right-hand side means the gas-phase pressure gradient, and the second term is the viscous stresses. The last term,  $S_u$  [ $\text{kg}\cdot\text{m}^{-2}\cdot\text{s}^{-2}$ ], is the source term, denoting the increase of pressure gradient due to Darcy's effect in the electrodes. In many reduced-dimensional models, the convective and viscous are omitted in porous media with the assumption that Darcy's effect and diffusion dominate in the pore region. A detailed mathematical description of the source terms is shown in Table 1.

## 2.3. Conservation and transport of energy

The heat generation in PEM fuel cells originates from the entropic heat of reaction, the irreversibility of reaction, Joule heating (due to ohmic resistance), and phase change [44,64], and the heat can be transported via convection and conduction [8]. The most common form of energy equation utilized in fuel cell modeling is as shown below [61, 64,78]

$$\frac{\partial}{\partial t} [(\rho c_p)_{fl,sl}^{\text{eff}} T] + \nabla \cdot [(\rho c_p)_{fl}^{\text{eff}} \vec{u}_g T] = \nabla \cdot (k_{fl,sl}^{\text{eff}} \nabla T) + S_T \quad (7)$$

where  $\rho$  is the density in [ $\text{kg}\cdot\text{m}^{-3}$ ];  $c_p$  denotes the specific heat in [ $\text{J}\cdot\text{kg}^{-1}\cdot\text{K}$ ];  $T$  denotes the temperature in [K]; the subscripts fl and sl denote fluid and solid phase properties;  $k$  is the thermal conductivity in [ $\text{W}\cdot\text{m}^{-1}\cdot\text{K}^{-1}$ ];  $S_T$  is the source term of the energy equation in [ $\text{W}\cdot\text{m}^{-3}$ ]; and the superscript eff is the effective properties. It should be pointed out that the effective properties of  $\rho c_p$  and  $k$  are assumed to be the average values of the solid and fluid phases taking into account all materials including gas mixture, water, ionomer, catalyst, and other substances in the computational domain, and mathematical equations can be found elsewhere [61,64,79]. The first term on the left-hand side is the transient volumetric energy accumulation rate, while the second term represents the energy accumulation rate due to convection when the gas flows through the void region of channels and porous media. The first term on the right-hand side is the heat conduction through fluid and solid phases, and the source term,  $S_T$ , is the heat generation and consumption due to reaction, Joule heating, and phase changes. A detailed explanation of the source terms in the energy equation is summarized in Table 1.

## 2.4. Conservation and transport of gas species

The transport of gas species (e.g., oxygen, nitrogen, hydrogen, and vapor) in channels and porous electrodes, involves two major mechanisms – convection and diffusion [65,77,80,81]. The convection-diffusion process in a fuel cell is often expressed as follows [44,69],

$$\frac{\partial}{\partial t} [\varepsilon(1-\Phi_l)\rho_g Y_i] + \nabla \cdot (\rho_g \vec{u}_g Y_i) = \nabla \cdot (\rho_g D_i^{\text{eff}} \nabla Y_i) + S_i \quad (8)$$

where  $Y$  represents the mass fraction of the  $i^{\text{th}}$  species in the gas mixture, and  $D$  is the diffusion coefficients in [ $\text{m}^2\cdot\text{s}^{-1}$ ]. The first term on the left-hand side denotes the accumulation rate of specific gas species, while the second term refers to the net increase of gas species due to convection. The first term on the right-hand side represents the net accumulation of gas species due to diffusion. The source term,  $S_i$  [ $\text{kg}\cdot\text{m}^{-3}\cdot\text{s}^{-1}$ ], represents the reactant gas species consumption due to reaction as well as the water vapor generation or consumption due to phase change among vapor, liquid, and dissolved water. Detailed mathematical description of the source terms in gas species transport equations is presented in Table 1.

It should be noted that the catalyst surface may be covered by a thin layer of ionomer in actual CLs, and the concentration of the dissolved  $\text{O}_2$  and  $\text{H}_2$  in ionomer can be determined by Henry's Law [61,69].

$$c_i = \frac{p_i}{H_i} \quad (9)$$

where  $p$  is the partial pressure of species  $i$  (i.e.,  $\text{O}_2$  or  $\text{H}_2$ ) on the gas side in [Pa],  $H$  is the Henry's constant in [ $\text{Pa}\cdot\text{m}^3\cdot\text{kmol}^{-1}$ ], and  $c$  is the gas species concentration on the ionomer side in [ $\text{kmol}\cdot\text{m}^{-3}$ ]. The dissolved species is transported mainly via diffusion through the thin ionomer layer.

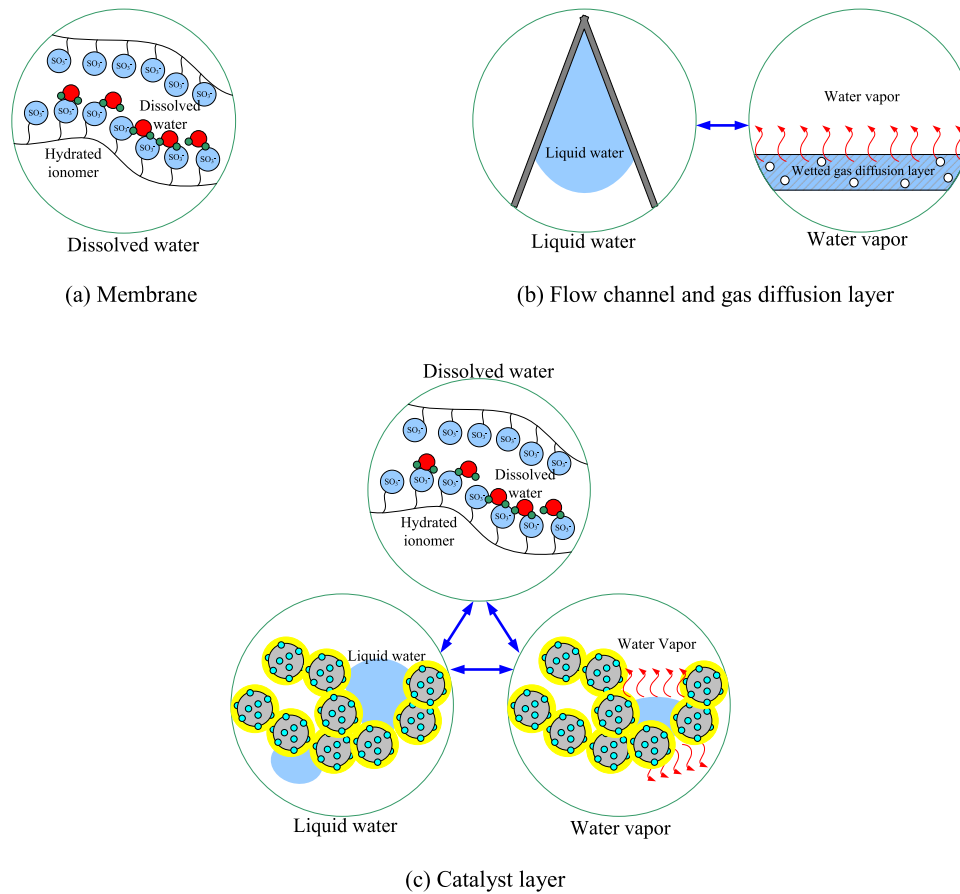


Fig. 2. Schematic of phase changes of water in different cell components: (a) membrane, (b) flow channel and gas diffusion layer, and (c) catalyst layer.

### 2.5. Conservation and transport of liquid water

The transport of liquid water is caused by the capillary pressure gradient in the porous media and the drag effect by the gas flow. The liquid water can originate from dissolved water in membrane and vapor in the gas mixture, as shown in Fig. 2. Dissolved water in membrane (or ionomer) can be generated by either reactions or absorption of liquid and vapor in pores [59,67,82]. When the content of dissolved water in membrane is greater than the equilibrium value, the excess membrane water is transferred to liquid or vapor [61,79]. When the vapor concentration is larger than the saturated concentration, the excess water vapor will be transferred to liquid or membrane water via phase change, and vice versa [83]. It should be pointed out that phase change pathways in fuel cell modeling can be inconsistent. For instance, the phase change between liquid and dissolved water is neglected with the assumption that the reaction product water is in the dissolved phase, excess dissolved water is transferred to vapor, and excess vapor is transferred to liquid in [8], while the phase change among dissolved, vapor and liquid water is assumed to occur simultaneously with different phase change rates in [79]. The impact of phase change pathways and rates on cell performance remains debated. In addition, although many fuel cell models assume the product water is dissolved in the membrane [8,34,59,64,67,79,82], the product water can also be in liquid and vapor phases. Wu et al. [84] compared the three water production mechanisms via 3D numerical models. The modeling results suggest that the water production mechanism has a significant impact on the non-equilibrium behaviors of fuel cells, while at equilibrium state, the water production mechanisms have a negligible effect on the final fuel cell performance [84]. For simplicity, only the dissolved water production mechanism is considered in this review.

The transport of liquid water can be numerically determined by the

following equation, derived by applying Darcy's law to the transport of liquid in porous media [34,64]:

$$\frac{\partial}{\partial t} (\varepsilon \Phi_l \rho_l) + \nabla \cdot (f \rho_l \vec{u}_g) = \nabla \cdot (\rho_l D_l \nabla \Phi_l) + S_l \quad (10)$$

where the subscript l is the properties of liquid water, and  $f$  denotes the dimensionless interfacial drag coefficient, which is defined as [66,85]

$$f = \frac{K_l \mu_g}{K_g \mu_l} \quad (11)$$

where  $K$  is the permeability coefficient in [m<sup>2</sup>]. The capillary diffusion coefficients of the liquid phase,  $D_l$  [m<sup>2</sup>•s<sup>-1</sup>], in GDLs and CLs can be derived from [8]

$$D_l = -\frac{K_l}{\mu_l} \frac{dp_{ca}}{d\Phi_l} \quad (12)$$

where  $p_{ca}$  is the capillary pressure in [Pa]. Many empirical models have been developed to estimate the capillary pressure in porous media [2,61, 66,86,87], and the Leverett function is the most commonly employed in fuel cell studies taking the surface tension,  $\sigma$  [N•m<sup>-1</sup>], intrinsic permeability,  $K_0$  [m<sup>2</sup>], porosity,  $\varepsilon$ , contact angle,  $\theta$  [°], and volume fraction of liquid water,  $\Phi_l$ , as variables [2,61]:

$$p_{ca} = \begin{cases} \sigma \cos \theta \left( \frac{\varepsilon}{K_0} \right)^{0.5} [1.42(1 - \Phi_l) - 2.12(1 - \Phi_l)^2 + 1.26(1 - \Phi_l)^3], & \theta < 90^\circ \\ \sigma \cos \theta \left( \frac{\varepsilon}{K_0} \right)^{0.5} [1.42\Phi_l - 2.12\Phi_l^2 + 1.26\Phi_l^3], & \theta > 90^\circ \end{cases} \quad (13)$$

The first term on the left-hand side of Eq. (10) is the accumulation

rate of liquid water, while the second term is the water transported by gas-phase inertial drag. The first term on the right-hand side represents the capillary flow due to saturation gradient in the electrodes, and the source term,  $S_l$ , means the liquid water generation rate due to phase change (see Table 1 for detailed mathematical description).

The source term of liquid water generation as a result of phase change from dissolved water,  $S_{d-1}$  in  $[\text{kg}\cdot\text{m}^{-3}\cdot\text{s}^{-1}]$ , can be calculated based on the following equation [34,79].

$$S_{d-1} = \zeta_{d-1} \frac{\rho_{\text{mem}} M_{\text{H}_2\text{O}}}{EW} (\lambda_d - \lambda_{\text{eq}}) \quad (14)$$

where  $\zeta_{d-1}$  is the phase change rate from the dissolved water to liquid in  $[\text{s}^{-1}]$ ;  $\rho$  is the density in  $[\text{kg}\cdot\text{m}^{-3}]$ ;  $M_{\text{H}_2\text{O}}$  denotes the molecular weight of water in  $[\text{kg}\cdot\text{kmol}^{-1}]$ ;  $EW$  denotes the equivalent weight of membrane in  $[\text{kg}\cdot\text{kmol}(\text{SO}_3\text{H})^{-1}]$ ;  $\lambda_d$  and  $\lambda_{\text{eq}}$  are the actual and equilibrium dissolved water content in ionomer in  $[\text{kmol}(\text{H}_2\text{O})\cdot\text{kmol}(\text{SO}_3\text{H})^{-1}]$ .

## 2.6. Conservation and transport of water in the membrane

The transport mechanisms of dissolved water in membranes are typically described by the Nernst-Planck equation [88] where the water transport arising from the electrostatic force acting on the hydronium ion [44,89], diffusion as a result of concentration gradients [90], and convection (or hydraulic permeation) owing to pressure gradients [44, 85]. The transport of water due to electrostatic force is also referred to as the electro-osmotic drag (EOD) effect, which is the phenomenon that a certain amount of dissolved water will accompany protons transported from anode to cathode [53,68]. The diffusion of dissolved water is driven by concentration gradients across the membrane, while the convective transport is mainly driven by the liquid-phase pressure gradient. The transport of water dissolved in the membrane (and ionomer) can be expressed as [8,36,65,67,85]:

$$\frac{\partial}{\partial t} \left( \frac{\rho_{\text{mem}} M_{\text{H}_2\text{O}} \omega \lambda_d}{EW} \right) + \nabla \cdot \left( \frac{J_{\text{ion}} n_d M_{\text{H}_2\text{O}}}{F} \right) = \nabla \cdot \left( D_d^{\text{eff}} \nabla \left( \frac{\rho_{\text{mem}} M_{\text{H}_2\text{O}} \lambda_d}{EW} \right) \right) + S_d \quad (15)$$

where  $\rho$  is the density in  $[\text{kg}\cdot\text{m}^{-3}]$ ;  $EW$  denotes the equivalent weight of membrane in  $[\text{kg}\cdot\text{kmol}(\text{SO}_3\text{H})^{-1}]$ ;  $M_{\text{H}_2\text{O}}$  denotes the molecular weight of water in  $[\text{kg}\cdot\text{kmol}^{-1}]$ ;  $\omega$  denotes the volume fraction of the ionomer in the computational domain;  $\lambda_d$  is the actual dissolved water content in ionomer in  $[\text{kmol}(\text{H}_2\text{O})\cdot\text{kmol}(\text{SO}_3\text{H})^{-1}]$ ;  $n_d$  is the number of water molecules accompanied with each proton ( $n_d = 2.5/22\lambda_d$ );  $J_{\text{ion}}$  is the proton current density in  $[\text{A}\cdot\text{m}^{-2}]$ ;  $F$  represents the Faraday's constant in  $[\text{C}\cdot\text{kmol}^{-1}]$ ; and  $D_d^{\text{eff}}$  is the effective diffusion coefficient of dissolved accounting for the ionomer fraction and distribution in  $[\text{m}^2\cdot\text{s}^{-1}]$ . A detailed explanation of the source terms,  $S_d$   $[\text{kg}\cdot\text{m}^{-3}\cdot\text{s}^{-1}]$ , of the dissolved water transport equation can be found in Table 1.

## 2.7. Conservation and transport of charged species

The transport of charged species, including electrons and protons in PEM fuel cells, is dominated by conduction via Ohm's law. In anode CLs, electrons and protons are generated by hydrogen oxidation reaction (HOR) on the catalyst surfaces. In cathode CLs, electrons and protons are diminished owing to the oxygen reduction reaction (ORR), where the charged species are combined with oxygen, generating water in the form of dissolved water in ionomer [34,91]. The transport of electrons in the conductive components of CLs, GDLs, bipolar plates, and external electric devices is dominated by Ohm's law of conduction, while the transport of protons only occurs in the ionomer phase of CLs and membrane [44,92,93]. Jiao and Li [61] performed a time constant analysis of various transient phenomena in PEM fuel cells, and the results indicate that the time constant for the migration of protons and electrons is only around 0.2  $\mu\text{s}$ , which is much faster than gas transport (0.004 s), liquid water transport (0.04 s), membrane water transport (17 s), and heat

transfer (0.004 s). This suggests that the electrons and protons can quickly achieve an equilibrium state, and thus the transient terms in the governing equations are often omitted [48,64,94,95].

Therefore, ionic and electronic charge transport can be formulated as follows [59,96],

$$0 = \nabla \cdot (\kappa_{\text{ion}}^{\text{eff}} \nabla \varphi_{\text{ion}}) + S_{\text{ion}} \quad (16)$$

$$0 = \nabla \cdot (\kappa_{\text{ele}}^{\text{eff}} \nabla \varphi_{\text{ele}}) + S_{\text{ele}} \quad (17)$$

where  $\kappa_{\text{ion}}^{\text{eff}}$  and  $\kappa_{\text{ele}}^{\text{eff}}$  denote the ionic and electronic conductivity in  $[\text{S}\cdot\text{m}^{-1}]$ , and  $\varphi_{\text{ion}}$  and  $\varphi_{\text{ele}}$  are the electric potential of the electron- and ion-conducting phases, respectively. A detailed mathematical description of the source terms is shown in Table 1.

## 2.8. Electrochemical reaction rate

The rate of oxygen and hydrogen consumption, water production, and heat generation is governed by the reaction rate [10,66,97,98]. The most commonly employed electrode kinetics in fuel cell modeling is the so-called Butler-Volmer equation as follows [99]:

$$i = i_0 \left[ \exp\left(\frac{\beta F \eta_{\text{act}}}{RT}\right) - \exp\left(-\frac{\alpha F \eta_{\text{act}}}{RT}\right) \right] \quad (18)$$

where  $i$  and  $i_0$  are the actual and exchange current density in  $[\text{A}\cdot\text{m}^{-2}]$ , respectively;  $\alpha$  and  $\beta$  is the charge transfer coefficients;  $F$  is Faraday's constant in  $[\text{C}\cdot\text{kmol}^{-1}]$ ;  $R$  is the universal gas constant in  $[\text{J}\cdot\text{kmol}^{-1}\cdot\text{K}^{-1}]$ ;  $T$  is the temperature in  $[\text{K}]$ ; and  $\eta_{\text{act}}$  is the activation over-potential in  $[\text{V}]$ . The definition of transfer coefficient significantly varies in different studies [100,101], and the present form is employed for simplicity as recommended by the IUPAC in 2014 [100]. The exchange current density can be calculated as follows [102],

$$i_0 = i_0^{\text{ref}} r_f \left( \frac{c_r}{c_{\text{ref}}} \right)^\gamma \exp\left[ -\frac{E_{\text{act}}}{RT} \left( 1 - \frac{T}{T_{\text{ref}}} \right) \right] \quad (19)$$

where  $i_0^{\text{ref}}$  is the reference exchange current density at the reference temperature and pressure per unit catalyst surface area in  $[\text{A}\cdot\text{cm}_{\text{Pt}}^{-2}]$ ;  $r_f$  is the electrode roughness factor in  $[\text{m}_{\text{Pt}}^2\cdot\text{m}^{-2}]$ ;  $c_r$  and  $c_{\text{ref}}$  are the actual and reference reactant molar concentration in  $[\text{kmol}\cdot\text{m}^{-3}]$ , respectively;  $\gamma$  is reaction order (ranging from 0.5 for HOR to 1.0 for ORR); and  $E_{\text{act}}$  is the activation energy in  $[\text{J}\cdot\text{kmol}^{-1}]$ . The transfer coefficient and reaction order employed in fuel cell modeling significantly vary in different studies [99]. The electrode roughness factor for a dry CL is defined as the ratio of catalyst surface area to the geometric area. The electrode roughness factor can also be affected by liquid water coverage on the electrode surface, and a correction factor is often applied to account for the liquid water saturation in CLs [45,61,102,103].

$$r_f = (1 - \Phi_1)^m \frac{A_{\text{Pt}}}{A_{\text{geo}}} = (1 - \Phi_1)^m a L_{\text{Pt}} \quad (20)$$

where  $\Phi_1$  is the volumetric fraction of liquid water in the CL pores,  $m$  is the correction factor accounting for the liquid-occupied catalyst surface,  $A_{\text{Pt}}$  is the active surface area of the Pt catalyst in  $[\text{m}^2]$ ,  $A_{\text{geo}}$  is the geometric area of the overall electrode in  $[\text{m}^2]$ ,  $a$  is the electrochemical surface area (ECSA) in  $[\text{cm}^2\cdot\text{mg}_{\text{Pt}}^{-1}]$ , and  $L_{\text{Pt}}$  is the Pt loading in  $[\text{mg}_{\text{Pt}}\cdot\text{cm}^{-2}]$ .

Springer et al.'s [14,99] model assumes zero anode overpotential and simplifies the cathode kinetics as the Tafel law,

$$i_c = i_{0,c} \exp\left(-\frac{\alpha_c F \eta_{\text{act}}}{RT}\right) \quad (21)$$

Um et al. [44] employs the Tafel law for cathode kinetics and a linear equation for cathode polarization as follows with the assumption that the anode overpotential is very small,

$$i_a = i_{0,a} \frac{(\beta_a + \alpha_a) F \eta_{act}}{RT} \quad (22)$$

It should be noted that the Butler-Volmer equation and its variant forms are theoretically valid based on transition state theory for elementary reaction steps. However, the application of these equations on HOR and ORR reaction remains debated [1,99].

## 2.9. Potential

There exists a maximum achievable voltage, a.k.a. reversible voltage, which can only be obtained as the operation of PEM fuel cells is thermodynamically reversible. The reversible voltage,  $V_{rev}$  [V], can be calculated via Nernst equation [16,34,79,104] below

$$V_{rev} = \frac{\Delta g_{ref}}{2F} + \frac{\Delta s_{ref}}{2F} (T_0 - T_{ref}) + \frac{RT_0}{2F} \ln \left[ \left( \frac{p_{H_2}^{in}}{p_{ref}} \right) \left( \frac{p_{O_2}^{in}}{p_{ref}} \right)^{1/2} \right] \quad (23)$$

where  $g$  is the Gibbs function of reaction formation in  $[J \cdot kmol^{-1}]$ ,  $s$  is entropy in  $[J \cdot kmol^{-1} \cdot K^{-1}]$ , and the subscript, ref, represents the parameters taken at the reference state of given temperature and pressure.

However, in a practical fuel cell, the actual operating voltage can be far below the reversible one, and the voltage losses rise as the operating current is increased due to four primary types of irreversible losses - the losses due to fuel crossover and internal currents as well as activation, ohmic, and concentration losses, as shown in Fig. 3. Fuel crossover and internal currents are caused by the unused fuels and electrons transported through the membrane as the diffusion of a small amount of the fuel and electrons is inevitable [1]. This diffusion process has a significant impact on the open-circuit voltage (OCV), which is smaller than the reversible voltage. However, this impact will be substantially reduced as the current is increased. Activation loss is resulted from the sluggish electrochemical reaction rate occurring on the electrode surface, and a small portion of energy has to be consumed to accelerate the electrochemical reactions. The activation loss can lead to a rapid voltage drop at the small current density region. Ohmic loss arises from electrical resistance in the fuel cells, including proton- and electron-conductive components [61]. The ohmic loss causes a linear drop of voltage at the intermediate current density region. The ohmic loss is affected by many factors, including membrane materials, hydration conditions, design of the electrodes, and interfacial conditions. Concentration loss is important in high current density region as a result of the mass transport resistance from external supply to reaction sites. The mass transport limitation results in the depletion of reactants on the electrode surface and can be further affected by the accumulated reaction water, which can either block the reactant transport pathways or occupy the reaction surface [8].

The cell output voltage is, therefore, calculated as a function of the

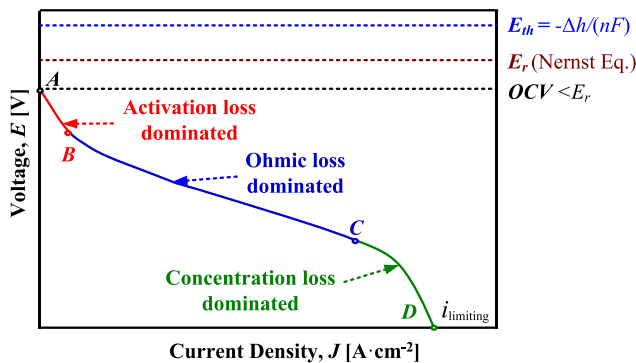


Fig. 3. A typical polarization curve of polymer electrolyte membrane (PEM) fuel cells ( $E_{th}$  denotes the thermo-neutral voltage,  $E_r$  represents the reversible voltage, and OCV is the open-circuit voltage) (Reprinted from [105] with permission from Zhao).

thermodynamically reversible potential, activation over-potential, and ohmic over-potential, with the mass transport limitations implicitly incorporated into the three terms.

$$V_{cell} = V_{rev} - \eta_{act} - \eta_{ohm} \quad (24)$$

where  $V_{cell}$  is the cell output voltage in [V];  $\eta_{act}$  is the activation over-potential in [V] in CLs; and  $\eta_{ohm}$  represents the total ohmic overpotential in [V] resulted from the ohmic resistance in all electron- and proton-conductive components. The mass transport resistance can affect the reactant availability and water content in the ionomer of the catalyst layer and membrane. The reactant availability directly impacts the reversible voltage and activation losses, while the water content can significantly affect the ionic conductivity of the ionomers, which determines the ohmic resistance of the fuel cell.

It should be noted that the accuracy of physics-based models depends on many transport and electrochemical coefficients, which are often determined by experiments [77,81,106–110] and theoretical analysis [80,107,111–117].

## 2.10. Length and time scale

The operation of PEM fuel cells involves complex transport and electrochemical phenomena within multiple length and time scales. Table 2 summarizes the typical length and time scales of the key fundamental phenomena in PEM fuel cells, including gas transport, liquid water transport, dissolved water transport in ionomer, heat transport, electrochemical double layer charging and discharging, and aging effect.

The thicknesses of the major components of membrane (25  $\mu m$ ), CLs (8.6–34  $\mu m$ ), GDLs (222  $\mu m$ ), and channels (1 mm) are taken from the experimental data from [8]. The time constants for the gas diffusion in channels and electrodes are in the range of  $1.3 \times 10^{-4}$ – $3.4 \times 10^{-2}$  s, and the transport of liquid water in GDLs and CLs is about  $0.7 \times 10^{-4}$ – $4.9 \times 10^{-2}$  s [61,69]. It should be noted that liquid water accumulation is relatively slow, and the time scale is reported to be about 3 min [118]. The dissolved water transport in ionomers is about 1 s, while it takes about 8.7 s for the membrane water content to change by  $\Delta \lambda = 10$  at the current density of  $1 A \cdot cm^{-2}$ . The heat transport in electrodes and membranes are in the order of  $10^{-5}$  and  $10^{-3}$  s, respectively, while the heat accumulation with the temperature increase of 10 K takes about 0.4–0.7 s. It can be seen that the migration of protons and electrons in CLs can be as small as 0.1  $\mu s$ , which is why most fuel cell models ignore the transient transport of protons and electrons [119]. In contrast, the time scale of the aging effect due to various mechanisms, including mechanical, thermal, chemical, and electrochemical degradations [120–122] varies significantly from 100 to 20,000 h based on experimental studies [4].

## 3. Pseudo-two-dimensional numerical model

Pseudo-2D models [45,46], a.k.a. 1+1 D models [27], are commonly employed in fuel cell studies due to their faster computing speed than 3D and 2D numerical models and higher fidelity than 1D and 0D models. Recent studies demonstrated that the calculation of pseudo-2D PEM fuel cell models can be twice faster than real time under various simplifications [45]. Therefore, pseudo-2D numerical models would become a viable option for real-time control applications with first-principles physics in the model formulation, representing the important physical and electrochemical processes involved in the fuel cells. Instead of solving the coupled governing equations (depicted in Section 2) in a 2D domain, most pseudo-2D models account for the changes in reactant composition along the flow channel and the physical and electrochemical phenomena in the through-the-membrane direction [39,40,44,62,91,123–125], which is the focus of this section.



**Table 2**  
Length and time scale of various phenomena in PEM fuel cells.

Phenomenon	Length scale	Typical values	Time constant	Equation source	Time scale
Gas diffusion in CL	$\delta_{CL}=8.6\text{--}34\ \mu\text{m}^*$	$D_{O_2, CL}^{eff} \approx 4.4\text{--}5.5 \times 10^{-7}\ \text{m}^2\cdot\text{s}^{-1}^*$	$\frac{\delta_{CL}^2}{D_{O_2, CL}^{eff}}$	N/A	$(0.13\text{--}2.6) \times 10^{-3}\ \text{s}$
Gas diffusion in GDL	$\delta_{GDL}=222\ \mu\text{m}^*$	$D_{O_2, GDL}^{eff} \approx 2.7 \times 10^{-6}\ \text{m}^2\cdot\text{s}^{-1}^*$	$\frac{\delta_{GDL}^2}{D_{O_2, GDL}^{eff}}$	[61,69]	$1.8 \times 10^{-2}\ \text{s}$
Gas diffusion in channel	$\delta_{channel}=1\ \text{mm}^*$	$D_{O_2, channel}^{eff} \approx 2.9 \times 10^{-5}\ \text{m}^2\cdot\text{s}^{-1}^*$	$\frac{\delta_{channel}^2}{D_{O_2, channel}^{eff}}$	N/A	$3.4 \times 10^{-2}\ \text{s}$
Liquid water transport in CL	$\delta_{CL}=8.6\text{--}34\ \mu\text{m}^*$	$D_{lq, CL}^{eff} \approx 10^{-6}\ \text{m}^2\cdot\text{s}^{-1}^{**}$	$\frac{\delta_{CL}^2}{D_{lq, CL}^{eff}}$	N/A	$(0.07\text{--}1.2) \times 10^{-3}\ \text{s}$
Liquid water transport in GDL	$\delta_{GDL}=222\ \mu\text{m}^*$	$D_{lq, GDL}^{eff} \approx 10^{-6}\ \text{m}^2\cdot\text{s}^{-1}^{**}$	$\frac{\delta_{GDL}^2}{D_{lq, GDL}^{eff}}$	[61]	$4.9 \times 10^{-2}\ \text{s}$
Liquid water accumulation	N/A	N/A	$\frac{D_{lq, GDL}^{eff}}{N/A}$	[118]	3 min
Water diffusion in membrane	$\delta_{mem} \approx 25\ \mu\text{m}^*$	$D_{lq, mem}^{eff} \approx 6.3 \times 10^{-10}\ \text{m}^2\cdot\text{s}^{-1}^*$	$\frac{\delta_{mem}^2}{D_{lq, mem}^{eff}}$	[118]	1 s
Water accumulation in membrane	$\delta_{mem} \approx 25\ \mu\text{m}^*$	$\rho_{mem}=1980\ \text{kg}\cdot\text{m}^3; \Delta\lambda=10; I=1\ \text{A}\cdot\text{cm}^{-2}; EW=1100\ \text{kg}\cdot\text{kmol}^{-1}; F=9.6487 \times 10^7\ \text{C}\cdot\text{kmol}^{-1}^{***}$	$\frac{D_{lq, mem}^{eff}}{2F\delta_{mem}\Delta\lambda\rho_{mem}}$	[119]	8.7 s
Heat transfer in electrode	$\delta_{electrode}=230.6\text{--}256\ \mu\text{m}^*$	$(\rho C_p)_{electrode}^{eff} \approx 1105\ \text{kJ}\cdot\text{m}^{-3}\cdot\text{K}^{-1}^{***}; k_{electrode}^{eff} \approx 1\ \text{W}\cdot\text{m}^{-1}\cdot\text{K}^{-1}$	$\frac{\delta_{electrode}^2 (\rho C_p)_{electrode}^{eff}}{k_{electrode}^{eff}}$	[119]	$(5.9\text{--}7.2) \times 10^{-5}\ \text{s}$
Heat accumulation in electrode	$\delta_{electrode}=230.6\text{--}256\ \mu\text{m}^*$	$(\rho C_p)_{electrode}^{eff} \approx 1105\ \text{kJ}\cdot\text{m}^{-3}\cdot\text{K}^{-1}^{***}; V=0.4\ \text{V}; I=1\ \text{A}\cdot\text{cm}^{-2}; \Delta T=10\ \text{K}$	$\frac{\delta_{electrode} (\rho C_p)_{electrode}^{eff} \Delta T}{VI}$	[119]	0.6–0.7 s
Heat transfer in membrane	$\delta_{mem} \approx 25\ \mu\text{m}^*$	$(\rho C_p)_{mem}^{eff} \approx 4840\ \text{kJ}\cdot\text{m}^{-3}\cdot\text{K}^{-1}^{***}; k_{mem}^{eff} \approx 1\ \text{W}\cdot\text{m}^{-1}\cdot\text{K}^{-1}^{**}$	$\frac{\delta_{mem}^2 (\rho C_p)_{mem}^{eff}}{k_{mem}^{eff}}$	[61,119]	$3 \times 10^{-3}\ \text{s}$
Heat accumulation in membrane	$\delta_{mem}=25\ \mu\text{m}^*$	$(\rho C_p)_{mem}^{eff} \approx 4840\ \text{kJ}\cdot\text{m}^{-3}\cdot\text{K}^{-1}^{***}; V=0.4\ \text{V}; I=1\ \text{A}\cdot\text{cm}^{-2}; \Delta T=10\ \text{K}$	$\frac{\delta_{mem} (\rho C_p)_{mem}^{eff} \Delta T}{VI}$	[119]	0.4 s
Electrochemical double layer charging and discharging	$\delta_{CL}=8.6\text{--}34\ \mu\text{m}^*$	$A_{specific} \approx 10^5\ \text{m}^{-1}; C \approx 0.2\ \text{F}\cdot\text{m}^{-2}; \kappa_{ele}^{eff} \approx 50\ \text{S}\cdot\text{cm}^{-1}; \kappa_{ion}^{eff} \approx 0.1\ \text{S}\cdot\text{cm}^{-1}^{**}$	$\delta_{CL}^2 A_{specific} C \left( \frac{1}{\kappa_{ele}^{eff}} + \frac{1}{\kappa_{ion}^{eff}} \right)$	[61,69,118]	$(0.1\text{--}2.3) \times 10^{-6}\ \text{s}$
Aging effect	N/A	N/A	$\frac{1}{N/A}$	[4]	100–20,000 h

Note: \* denotes values calculated from [8]; \*\* denotes values taken from [61]; and \*\*\* denotes values taken from [119]; The meaning of symbols refers to the nomenclature table.

### 3.1. Model development

Fuller and Newman [39] developed a pseudo-2D model for the membrane and electrode assembly (MEA) with a co-current flow of air and reformed methanol streams (cathode mixture of water vapor, nitrogen, and oxygen, and anode mixture of vapor, carbon dioxide, and hydrogen). The transport phenomena were solved in the direction of across the cell, and the mass balance was solved in the flow channels. Both isothermal and non-isothermal cases were examined, and the results indicated that the water and thermal management are interrelated

and heat removal strongly affects the cell operation. Nguyen and White [40] developed a steady-state pseudo-2D fuel cell model, accounting for the physics across the membrane and along the flow channels. The liquid water was assumed to present as tiny droplets with negligible volume. The voltage drop along the channels was neglected with the high electronic conductivity of current collectors, and the pressure gradient was set zero along the channels. Various humidification strategies were examined, and the results suggested the air should be humidified when used as cathode streams and anode humidification can be employed to compromise the inadequate back diffusion of water in membrane.

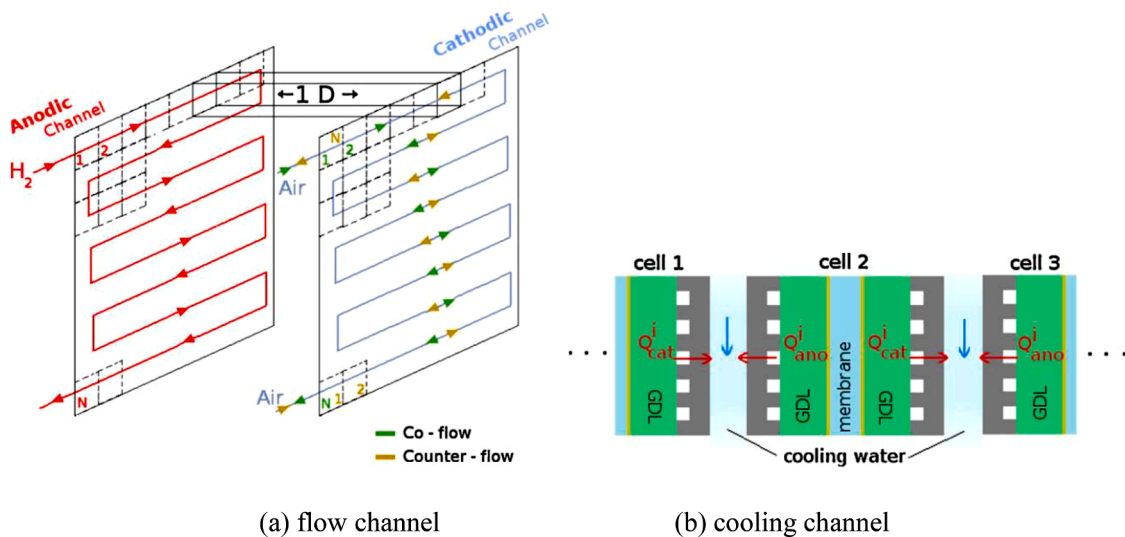


**Fig. 4.** Schematic of the pseudo-2D PEM fuel cell model by Chupin et al.: (a) flow channel and (b) cooling channel. (Reprinted from [124] with permission of Elsevier).

Shamardina et al. [123] established a pseudo-2D fuel cell model taking into account the transport phenomena across the membrane and the oxygen depletion along the flow channels. A pseudo-crossover current density was employed to account for the permeation of oxygen and hydrogen through the membrane. However, in the membrane, the effect of water content on the conductivity was ignored, and this major assumption may bring significant errors when the model is applied to conditions beyond the validation range. The computing speed was reported to be a few seconds in response to changes in operational conditions based on a modern computer (specification of the computing resources was not specified).

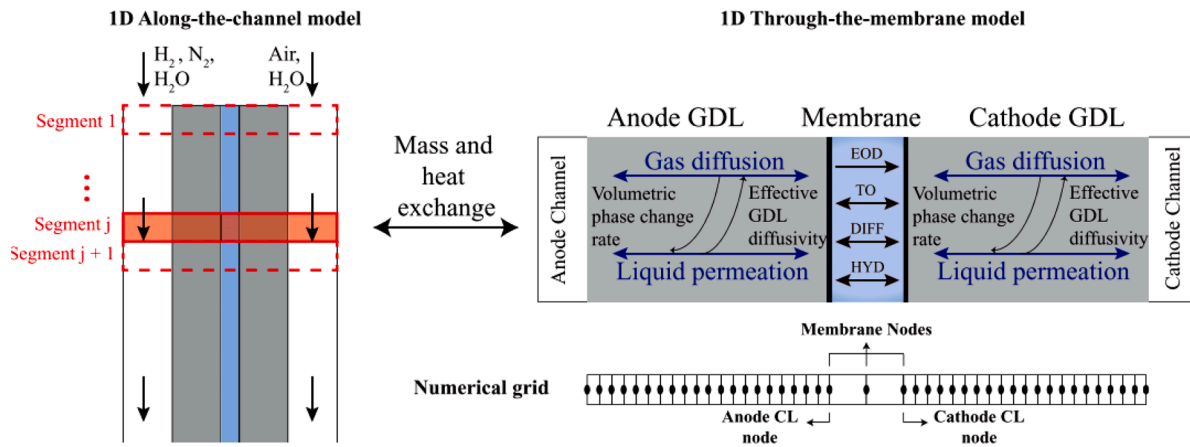
Chupin et al. [124] developed a pseudo-2D fuel cell model by integrating the two-phase flow with an agglomerate CL model. The transport and electrochemical phenomena between the anodic and cathodic channels were included in a 1D fuel cell model, while the mass balance was applied to the gas flow in channels (see Fig. 4a). The simulation results suggested that the effect of coolant flow direction (see Fig. 4b) on the global fuel cell performance is insignificant, although the current density distribution is changed substantially along the channel. Both co-

and counter-flow of air and hydrogen were also examined, and the counter-flow mode is suggested to be preferable for a stable operation. The CLs were treated as interfaces for water transport to accelerate the computing speed; however, the computing speed is not reported.

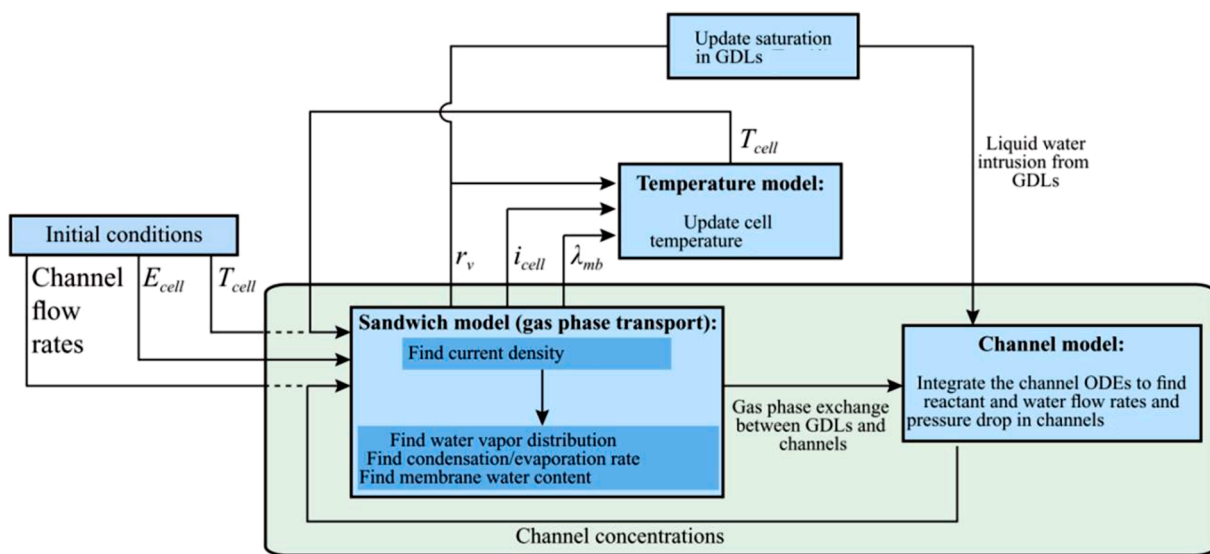
Goshtasbi et al. [45] developed a semi-empirical, transient, and pseudo-2D fuel cell model with the cell voltages as inputs and current densities as outputs under various operational conditions taking thermal energy and two-phase transport phenomena into account. A reduced model was applied to the membrane with the assumption that the water content in a thin membrane is almost linear, which reduces the partial differential equation (PDE) of membrane water transport to an ordinary differential equation (ODE) as shown below,

$$\frac{d\lambda_d}{dt} = -\frac{EW}{\rho_{mem}\delta_{mem}}(N_{w,mem}^{ca} - N_{w,mem}^{an}) \quad (25)$$

where  $\lambda_d$  is the actual dissolved water content in ionomer in [kmol (H<sub>2</sub>O)•kmol(SO<sub>3</sub>H)<sup>-1</sup>]; EW denotes the equivalent weight of membrane in [kg•kmol(SO<sub>3</sub>H)<sup>-1</sup>];  $\rho_{mem}$  is the membrane density in [kg•m<sup>-3</sup>];  $\delta_{mem}$  is the thickness of membrane in [m]; and  $N_{w,mem}^{ca}$  and  $N_{w,mem}^{an}$  are the



(a) Pseudo-2D framework



(b) Numerical solution method

Fig. 5. Pseudo-2D PEM fuel cell model developed by Goshtasbi et al.: (a) Pseudo-2D model and (b) numerical solution method. (Adapted from [45] with permission of Electrochemical Society).

water flow rates across the membrane on the cathode and anode sides, respectively. The numerical implementation can affect computational speed, and the pseudo-2D framework is presented in Fig. 5a. The framework consists of 25 nodes along the channel and 43 nodes in the through-the-membrane direction. A weak spatial connection was established through boundary conditions accounting for the reactant and water transport in the through-the-membrane direction and the bulk flow in the along-the-channel direction. This approach enabled different numerical schemes for different problems, e.g., the backward Euler method (fully implicit) for temperature PDE and the BEAM and Warming implicit method for liquid water PDE. The implicit methods enabled a larger time step in comparison with explicit methods to avoid numerical stability issues and to reduce the computational time in comparison with the real-time operation. The differential algebraic equation (DAE) system was solved by Newton’s method. More details about the numerical solution methods can be found in Fig. 5b. In addition, this approach enabled parallel computing, which can further improve computing speed. Besides, the gas dynamics which are on the order of 0.01 s were ignored, and 0.1 s is selected as the time step for a balanced accuracy and computing speed. Therefore, this model enabled the computational speed twice to four times faster than real-time cell operation. Further, a bi-domain approach was applied to their model to distinguish the transport phenomena under the land and the channel [46]. The pseudo-2D model has been demonstrated for the first time to be a powerful tool for real-time control applications that incorporate as many physical and electrochemical phenomena as possible [45,46,126].

Yang et al. [91] established a comprehensive system model by integrating a pseudo-2D dynamic two-phase stack model, a 1D dynamic humidifier model, a 1D hydrogen pump model, a radiator model, and an air compressor model. The system configuration is shown in Fig. 6. Explicit numerical schemes were applied to PDEs, and a time step of  $10^{-6}$  s was selected for the numerical solution as a compromise of prediction accuracy and computing speed. This model has excellent capabilities of transient performance prediction and system optimization and control if the computational speed can be optimized.

### 3.2. Comparison of pseudo-two-dimensional numerical models

Many pseudo-2D numerical fuel cell models, which account for the composition changes along the flow channels and the physics in the through-the-membrane direction, have been developed in the past three decades. A summary and comparison of these models are presented in Table 3.

Most of these models utilize the relative humidity (RH), temperature, and pressure of the reactants, as well as the cell temperature,

stoichiometry ratio (or flow rates), and current density as the input variables, and the output variables are focused on the distribution of voltage, current density, temperature, reactant and water along the channels. It should be pointed out that the computational speed of the pseudo-2D model is dependent on the complexity of the transport and electrochemical phenomena being modeled, the numerical methods applied to solve the DAE systems, the required accuracy, and the selection of time steps [45,91,125,126]. The phenomena, including activation loss, ohmic loss, concentration loss, multispecies transport, membrane water, two-phase flow, non-isothermal effect, convection, diffusion, steady-state behavior, and transient behavior, have been fully or partially integrated into the pseudo-2D models in various studies such that the models can predict the real-time cell performance accurately over the entire operational ranges. It should be noted that these models are useful for small-size single fuel cells; however, the applicability to large fuel cells, especially for low stoichiometry ratio and low RH conditions, may not be appropriate [44].

Although the pseudo-2D model has not been widely implemented for the real-time control of PEM fuel cells, it can be used to control PEM fuel cells due to its balanced model fidelity and computing speed. By ignoring the gas dynamics, Goshtasbi et al.’s transient pseudo-2D model demonstrated twice faster computing speed than the actual physical process [45,126]. This implies the pseudo-2D model can be used to control the fuel cell real-time behaviors with proper assumptions.

## 4. One-dimensional numerical model

In this section, the 1D numerical model is defined as the PEM fuel cell models that address the transport and electrochemical phenomena discussed in Section 2 in the through-the-membrane direction in all essential components for all variables being solved.

### 4.1. Model development

Springer et al. [14] proposed a 1D mathematical model that is utilized to study the fuel cell performance accounting for the transport of gas species, water vapor, membrane water, and other effects. In their model, if the actual vapor partial pressure surpasses the saturated value, liquid water is considered in the continuity equation assuming the water exists in the form of uniformly dispersed droplets with zero volume in the computational domain such that it is deemed to have identical transport properties with water vapor. In addition, a classic correlation of the membrane water drag coefficient  $n_{drag} = 2.5\lambda/22$  was derived based on their experimental results. Bernardi and Verbrugge [49] established a 1D model to calculate the voltage losses due to anodic and

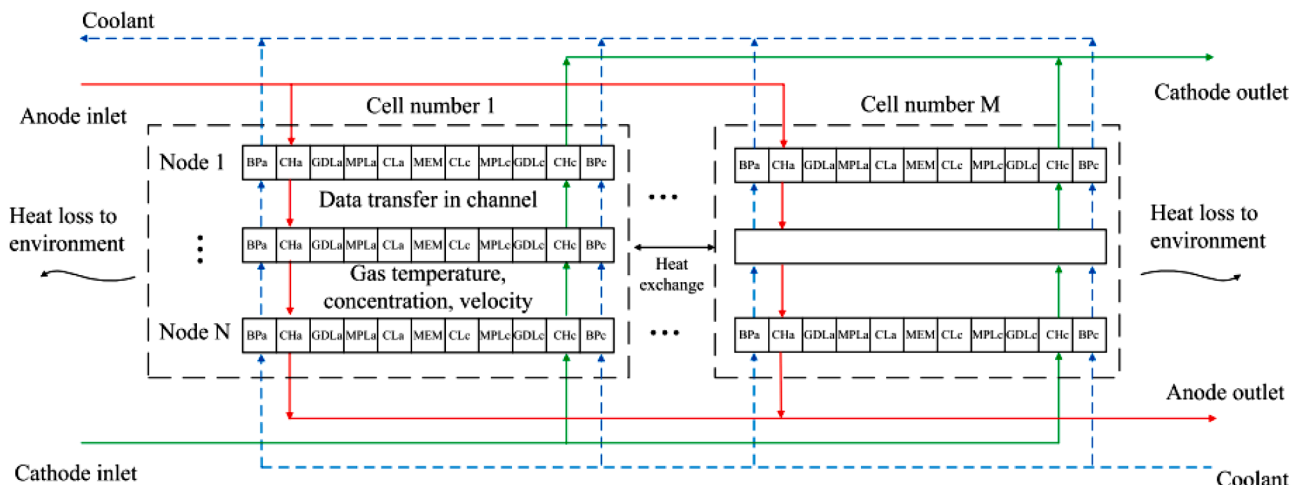


Fig. 6. Schematic of the pseudo-2D PEM fuel cell stack model by Yang et al. (Reprinted from [91] with permission of Elsevier).

**Table 3**  
Comparison of pseudo-two-dimensional numerical models for PEM fuel cells.

Model features	Fuller and Newman 1993	Nguyen and White 1993	Shamardina et al. 2010	Chupin et al. 2010	Goshtasbi et al. 2016–2019	Yang et al. 2019
<i>Type of Pseudo 2D model</i>	Channel	Channel	Channel	Channel	Channel	Channel
<i>Domain</i>						
Membrane	√	√	√	√	√	√
CL	√	√	√	×****	×****	√
GDL	√	√	√	√	√	√
Flow channel	√	√	√	√	√	√
Bipolar plate	×	√	×	√	√	√
Cooling channel	×	×	×	√	√	√
<i>Key input variables</i>						
Reactant RH	√**	√	-	√	√	√
Reactant temperature	√	√	-	-	√	√
Reactant pressure	√	√	√	√	√	√
Cell temperature	√	√	√	×***	√	√
Stoichiometry ratio/flow rate	√	√	√	√	√	√
Current density	×*	√	×*	×*	×*	√
<i>Physics included</i>						
Activation loss	-	√	√	√	√	√
Ohmic loss	√	√	√	√	√	√
Multispecies transport	√	√	√	√	√	√
Membrane water	√	√	×	√	√	√
Two-phase flow	×	√	×	√	√	√
Ice formation	×	×	×	×	×	√
Non-isothermal	√	√	×	√	√	√
Convection	×	×	×	×	×	×
Steady-state behavior	-	√	√	√	√	√
Transient behavior	-	×	×	×	√	√
Reactant crossover	×	×	√	×	√	×
Pressure drop	×	×	×	×	√	√
<i>Outputs reported</i>						
Voltage distribution	×*	√	×	×	×*	×
Current density distribution	√	√	×	√	×	×
Pressure distribution	×	×	×	×	×	×
Reactant distribution	√	√	×	×	×	×
Water distribution	√	√	×	√	√	√
Temperature distribution	√	√	×	√	√	√
<i>Validation</i>						
polarization curve	×	×	√	×	√	√
<i>Computation speed</i>						
	×	×	√	×	√	×
<i>References</i>	[39]	[40]	[123]	[124]	[45,126]	[91,125]

Note: √, ×, and – denote the features are included, excluded, and not mentioned in the corresponding studies, respectively, \* means the model utilizes voltage as input and current as output, \*\* means values are given indirectly, \*\*\* means coolant temperature is given, and \*\*\*\* means catalyst layer is treated as interface.

cathodic chemical reactions and the transport of protons and electrons. In their models, the CL was assumed macro-homogeneous and the membrane was fully hydrated. The transport of various species in the complicated structure of gas, liquid, and solid was modeled. Weisbrod et al. [50] enabled a detailed membrane model, in which the impact of water content on the physical and chemical properties of the membranes were mathematically described based on the experimental work by Springer et al. [14]. Baschuk and Li [51] modeled liquid water in CLs and GDLs, which enabled the simulation of water flooding in porous media of PEM fuel cells and evaluation of its effect on cell performance. The numerical implementation followed a procedure to consecutively solve the Nernst equation, mass transport equations, the Butler-Volmer equation (discretized by a quasi-linear approximation), and activation and ohmic overpotential equations. Wöhr et al. [52] developed a 1D mathematical model taking water and heat transport into account such that the dynamic responses of the PEM fuel cells after changes in electrical loads, gas flow rates, and humidification levels can be simulated. Rowe and Li [54] developed a 1D model based on non-isothermal phenomena in PEM fuel cells, and the anodic and cathodic humidification was incorporated in their work.

Falcão et al. [53] established a steady-state 1D fuel cell model taking thermal and water management into account. The heat transport is assumed to be conduction-dominated in GDLs, and the heat generation and consumption were modeled for CLs. The transport of water in membranes was treated as a combination of diffusion and electro-osmotic drag effects. Gao et al. [55] developed a multi-physics

1D fuel cell model for real-time simulation. In their model, the electrical, fluidic, and thermal domains were taken into account for each component, including membranes, CLs, GDLs, flow channels, bipolar plates, and cooling plates. However, the activation overpotential of cathode was calculated based on empirical correlations, which requires a stack polarization curve to determine the corresponding empirical coefficients. The reduced spatial dimensionality enabled the a fast computation speed (33% faster than the real time) while maintaining reasonable prediction of cell performance in respect of current density, RH, and gas species concentrations including oxygen, hydrogen, and water vapor. Abdin et al. [56] built a 1D mathematical model that directly integrates physical parameters into their model under some assumptions to reduce the computational load. Their model was composed of four sub-models, i.e., anode, cathode, membrane, and voltage. In each sub-model, the simplified conservation laws were applied such that the model can reveal the physical response corresponding to changes in operational conditions. This model can be implemented in the Matlab-Simulink environment with simplifications and assumptions, such as uniform current distribution, uniform temperature, water in the vapor phase at the membrane-electrode interface, no pressure gradient, and diffusion dominant. The modeling results agreed with experimental data acceptably with fairly light computing demand.

Bao et al. [10] developed an analytical control-oriented dynamic model for the fuel cell systems integrating air stream, and hydrogen flow recirculated by an injection pump. Their isothermal, steady-state model

was established for the understanding of mass transport in GDLs and water transport in membranes, where the liquid water accumulation due to finite-rate phase change and water flooding in cathode GDLs were modeled. Further, the transient phenomena in fuel cell systems were predicted by modeling the mechanical inertia of compressor and reactant supply in manifolds and single cells. In Bao et al. [10]’s model, the stoichiometric ratio (see Eq. (26)) is taken into account for the 1D model by introducing a logarithmic average of the molar fraction of oxygen between the inlets and outlets as the boundary condition of GDLs.

$$x_{O_2} = \frac{x_{O_2,in} - x_{O_2,out}}{\ln(x_{O_2,in}) - \ln(x_{O_2,out})} \quad (26)$$

Recently, aging effects have gained attention for fuel cell models with reduced spatial dimensions. Li et al. [47] established a 1D catalyst degradation model for PEM fuel cells taking Pt degradation and ECSA into account. Two major catalyst degradation modes - Ostwald ripening and Pt dissolution-re-precipitation - were modeled in their work (see Fig. 7). Their model can effectively capture the effect of temperature, RH, and reactant gas on the ECSA and performance deterioration, and the modeling results suggested that the severe catalyst degradation may be a limitation in the reduction of the Pt loading. Li and Wang [48] further extended the 1D physics-based agglomerate model to quantify the effects of catalyst degradation, in term of the loss in ECSA and the oxygen mass transport loss through the wrapped ionomer on the Pt particle surface, on the cell performance for a low Pt-loading PEM fuel cell. This agglomerate CL model was coupled with the performance model using the mixture approach, and this model enabled the investigation of non-uniform Pt degradation.

Jiang et al. [103] developed a 1D non-isothermal two-phase-flow fuel cell model taking into account the phase change phenomena, which was rarely included in previous studies. A switching function was constructed to determine the transport mechanism of liquid or vapor water, which enabled the coupling of liquid and vapor water in the same domain in one governing equation. The sensitivity analysis suggested the uncertainty in the model parameters has a strong effect on the model’s reliability and stability.

#### 4.2. Comparison of one-dimensional numerical models

The development of 1D numerical models has been promoted in the past three decades. A summary and comparison of these models are

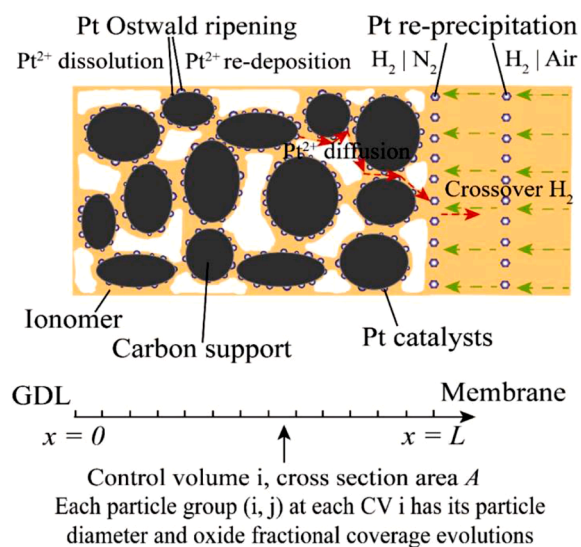


Fig. 7. Schematic of 1D Pt degradation model taking Pt Ostwald ripening and re-precipitation into account (Reprinted from [47] with permission of Electrochemical Society).

presented in Table 4. Most of these models utilize the RH, temperature, and pressure of the reactants, as well as the cell temperature, stoichiometry ratio (or flow rates), and current density as the input variables, and the output variables are focused on the cell voltage and other indicators such as outlet conditions and cell resistances. Li et al. [47,48] start to incorporate the aging effect into 1D models, by taking Pt degradation into account through modifying ECSA and the resistance to oxygen transport in the thin ionomer film covered on the catalyst surface. Further model development by incorporating the other aging effects including mechanical, thermal, chemical, and electrochemical degradations into the control-oriented models would enable the long-term performance prediction and control strategy adjustment. It should be pointed out that the computational speed of the control-oriented 1D model is dependent on the complexity of the transport and electrochemical phenomena being modeled. In other words, the computational speed can be enhanced by applying reasonable assumptions to simplify the governing equations. However, sufficient prediction accuracy should be maintained. The phenomena, including activation loss, ohmic loss, concentration loss, multispecies transport, membrane water, two-phase flow, electron transport, proton transport, non-isothermal effect, convection, diffusion, steady-state behavior, transient behavior, and aging effects, have been integrated or partially integrated into the 1D models in various studies such that the models are able to predict the short- and long-term performance accurately within the entire operational ranges. Further studies should also focus on the validation and calibration of the models against more physical variables other than just current-voltage curves, such as outlet conditions (including pressure, gas species concentrations, compositions, and flow rates), ohmic resistance, and temperature variations.

Although the implementation of 1D models in the actual fuel cell control is rarely reported, it can be potentially used to control PEM fuel cell operations due to its fast computing speed. Gao et al. [55] reported that the 1D models taking into account the electrical, fluidic, and thermal domains, including membranes, CLs, GDLs, flow channels, bipolar plates, and cooling plates, can be 33% faster than the real-time processes. This suggests the 1D model can be potentially used for the real-time control of PEM fuel cells.

#### 5. Zero-dimensional analytical model

0D analytical models, in this review, is defined as the models based on simplified conservation laws that do not require spatial dimensions for every component and every variable and do not require curve fitting to determine model coefficients. Many of these models were used in model-predictive control studies, which involve complete or partial fuel cell components as well as accessories [127–131]. Depending on the control objectives (e.g., energy efficiency, temperature, or pressure), many control-oriented 0D analytical models do not include all physics as depicted in Section 2, which may not be able to accurately predict the actual fuel cell dynamics. Therefore, the 0D analytical models that can be used to develop control strategies for different fuel cell components and systems are reviewed in this section.

##### 5.1. Model development

Many 0D analytical models have been utilized to develop control strategies; however, most of the models are over-simplified, and the validity requires further investigation [127–131]. Tirnovan and Giurgea [127] developed a control strategy to optimize the compressor speed and throttle opening of the air supply system to achieve the maximum energy efficiency of the fuel cell systems. The fuel cell model used to develop the control strategy consists of an empirical electrochemical model, a pressure drop model in pipes and channels based on flow rate and geometric parameters, and the energy balance of the fuel cell systems. The semi-empirical nature of the fuel cell models may introduce errors to the overall system model, which can be further improved.

**Table 4**  
Comparison of one-dimensional numerical models for PEM fuel cells.

Model features	Springer et al. 1991	Bernardi & Verbrugge 1992	Wöhr et al. 1998	Baschuk & Li 2000	Rowe & Li 2001	Bao et al. 2006	Falcão et al. 2009	Gao et al. 2010	Li et al. 2015–2017	Abdin et al. 2016	Jiang et al. 2018
<u>Domain</u>											
Membrane	✓	✓	✓	✓	✓	✓	✓	✓	✓	✓	✓
CL	✓	✓	✓	✓	✓	✓	✓	✓	✓	✓	✓
GDL	✓	✓	✓	✓	✓	✓	✓	✓	✓	✓	✓
Flow channel	✓	×	✓	✓	✓	×	✓	✓	✓	✓	✓
Bipolar plate	×	×	×	✓	×	✓	✓	✓	✓	✓	×
Cooling channel	×	×	×	×	×	×	×	✓	×	×	×
<u>Key input variables</u>											
Reactant RH	✓	✓	✓	✓	✓	✓	✓	✓	✓	✓	✓
Reactant temperature	✓	✓	✓	✓	✓	✓	✓	✓	✓	✓	✓
Reactant pressure	✓	✓	✓	✓	✓	✓	✓	✓	✓	✓	✓
Cell temperature	✓	✓	✓	✓	✓	✓	✓	✓	✓	✓	✓
Stoichiometry ratio/flow rate	✓	✓	✓	✓	✓	✓	✓	✓	✓	✓	✓
Current density	✓	✓	✓	✓	✓	✓	✓	✓	✓	✓	✓
<u>Physics included</u>											
Activation loss	✓	✓	✓	✓	✓	✓	✓	✓	✓	✓	✓
Ohmic loss	✓	✓	✓	✓	✓	✓	✓	✓	✓	✓	✓
Multispecies transport	✓	✓	✓	✓	✓	✓	✓	✓	✓	✓	✓
Membrane water	✓	✓	✓	✓	✓	✓	✓	✓	✓	✓	✓
Two-phase flow	×	✓	✓	✓	×	✓	×	×	✓	✓	✓
Electron transport	✓	✓	✓	✓	✓	×	×	×	✓	✓	✓
Proton transport	✓	✓	✓	✓	✓	✓	✓	✓	✓	✓	✓
Non-isothermal	×	×	✓	×	✓	×	✓	✓	✓	×	✓
Convection	×	×	✓	×	×	×	×	×	×	×	×
Steady-state behavior	✓	✓	✓	✓	✓	✓	✓	✓	✓	✓	✓
Transient behavior	×	×	✓	×	×	×	×	✓	✓	×	×
Aging effects	×	×	×	×	×	×	×	×	✓	×	×
<u>Outputs reported</u>											
Voltage	✓	✓	✓	✓	✓	✓	✓	✓	✓	✓	✓
Outlet pressure	×	×	×	×	×	✓	×	×	×	×	×
Outlet species composition	✓	×	×	×	×	×	×	×	×	×	×
Outlet species flow rate	✓	×	×	×	×	×	×	×	×	×	×
Temperature	×	×	×	×	×	×	×	✓	×	×	×
Resistance	✓	×	×	×	×	×	×	×	×	×	×
ECSA	×	×	×	×	×	×	×	×	✓	×	×
<u>Validation</u>											
Steady-state I-V curve	×	×	×	✓	✓	✓	✓	×	×	✓	✓
Transient voltage variation	×	×	×	×	×	×	×	✓	✓	×	×
Other physical variables	✓ resistance	×	×	×	×	×	×	✓ temp.	×	×	×
<u>Computation speed</u>											
Computation speed	×	×	×	×	×	×	×	✓	×	×	×
<u>References</u>											
References	[14]	[49]	[52]	[51]	[54]	[10]	[53]	[55]	[47,48]	[56]	[103]

Note: ✓ and × denote the features are included and excluded in the corresponding studies, respectively.

Matraji et al. [130] developed a control strategy to prevent permanent damage of fuel cells by regulating the anode and cathode pressures based on a nonlinear dynamic fuel cell model. The dynamic model was established based on the assumption that temperature and humidity were strictly controlled, and the pressure of various species was calculated based on mass conservation and ideal gas law. A MIMO controller based on second-order sliding mode and a ‘twisting algorithm’ is used to minimize the difference in anode and cathode pressures. However, the accuracy of the dynamic model was not evaluated, and its impact on the control performance remains unknown. Danzer et al. [131] developed a model predictive control strategy to avoid oxygen starvation, which is harmful to the fuel cell health, by controlling the pressure, current, and excess ratio of oxygen (i.e., stoichiometry ratio). A nonlinear fuel cell system model to estimate the dynamic responses of mass flow and pressure variation was established based on the flow resistance network. As the presented work was focused on testing the optimal control scheme, the fuel cell model was not validated, which may limit its practical application. Hong et al. [128] developed a multi-input multi-objective (MIMO) nonlinear strategy for fuel supply to the PEM fuel cells with anode recirculation and exhaust bleeding (see Fig. 8). The

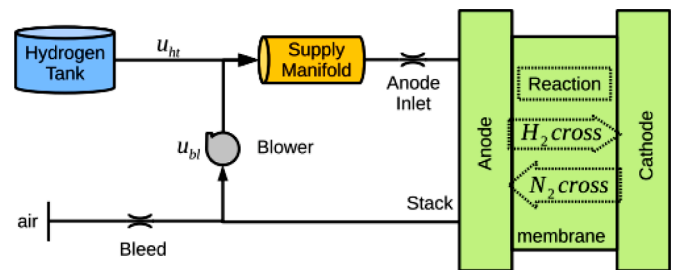


**Fig. 8.** Schematic of the fuel supply system for PEM fuel cell by Hong et al. (Reprinted from [128] with permission of Elsevier).

pressure dynamics of hydrogen and nitrogen in the anode was modeled based on mass conservation and ideal gas law, and the crossover of nitrogen and hydrogen was incorporated in the model. The emphasis of the presented work was placed on the controller performance, while the dynamic physical model was not validated.

As can be seen, many fuel cell models used for model-predictive

control are analytical, over-simplified, non-validated, and often focused on specific problems. Therefore, a comprehensive yet simple OD analytical model, including energy analysis, is scrutinized. Cownden et al. [21] established a OD analysis model by incorporating the second law of thermodynamics for the PEM fuel cell systems into a single cell model to investigate the performance of the fuel cell transportation system, which was composed of the stack, hydrogen supply, air compression, and coolant subsystems. It was found that the cell stack possesses the largest exergy destruction within the system, followed by the hydrogen ejector, air compressor, and radiator. Even though the details of the fuel cell model were not given, the thermodynamics analysis presented remains useful for the fuel cell system optimization using energy efficiency as the control objective. Kazim [22] also performed a OD exergy analysis for a 10 kW PEM fuel cell at various operational conditions, including pressure, air stoichiometry, temperature, and cell voltage. Exegetic efficiency, which is defined as the ratio of the output power to the overall exergy differences between the reactants and reaction products, of the PEM fuel cell system at various operational conditions was reported in their work; however, the exergy in individual cell components or auxiliaries were not considered. Hussain et al. [15] proposed a OD thermodynamic model of PEM fuel cell systems, integrating a fuel cell stack, an air compressor, a heat exchanger, two humidifiers, and a cooling pump and loop, as shown in Fig. 9. A parametric study was conducted to investigate the impact of operational conditions, including pressure, temperature, and stoichiometry ratio, on the energy and exergy efficiencies of the fuel cell systems, and the largest irreversibility was found to be from the stack which has drawn the greatest attention in research activities. Youssef et al. [23] established a lumped fuel cell model with linear algebra equations, which is employed to

evaluate the effect of operational and design parameters on the overall cell performance. Their model considered the mass conservation and energy balance, which does not necessarily require spatial dimensions, while thicknesses of GDLs and membranes were only considered for the calculation of ionic and electrode resistances. Many assumptions, such as constant membrane ionic conductivity and absence of phase change mechanisms, made this model less accurate to predict the cell performance over the entire range of operating conditions in comparison with those taking the dynamic membrane resistance and phase change into account.

Karimi et al. [26] developed a flow network model to investigate the distributions of pressure and flow rate for reactant streams. These distributions were subsequently incorporated into the single cell, which enabled the evaluation of the fuel cell performance at the stack level. Miotti et al. [27] proposed a control-oriented model for the automotive PEM fuel cell system by integrating an isothermal fuel cell model and auxiliary models (including a humidification chamber and a compressor) based on the “filling emptying” method. Shan and Choe [132] established a PEM fuel cell model considering the effects of (i) temperature gradients within the whole fuel cell, (ii) water redistribution in the membrane, (iii) proton redistribution in cathode CLs, and (iv) reactant redistribution in cathode GDLs. This allowed the model to estimate the dynamic performance of PEM fuel cells with acceptable accuracy. Musio et al. [28] established a generalized steady-state single fuel cell model, which was further developed to be a dynamic stack model by incorporating the pressure drop for a Z-shape flow configuration and thermal management and cooling sub-models. This model was less computationally expensive; however, the transient behaviors of the reactant transport, heat management, phase changes, and migration

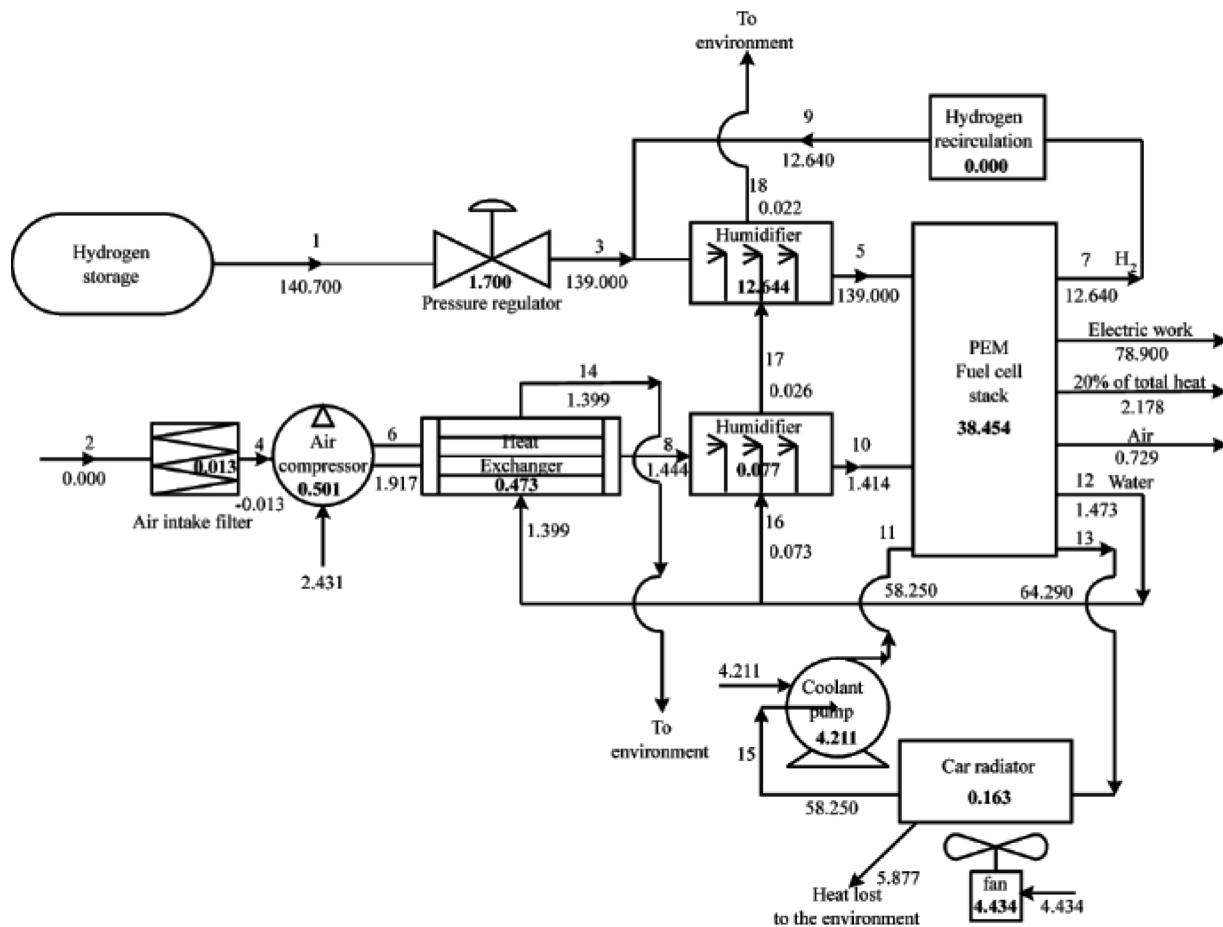


Fig. 9. Exergy flow diagram of the fuel cell system investigated at the operational conditions of  $I = 0.938 \text{ A}\cdot\text{cm}^{-2}$  and  $V = 0.466 \text{ V}$ . Bold values denotes the irreversibility rate in each component in the unit of kW (Adapted from [15] with permission of Elsevier).

of liquid and dissolved water were not included. Jung et al. [133] established a 0D analytical model by applying simple conservation laws of energy to a voltage model. The dynamic performance (including voltage, current density, oxygen excess ratio, and temperature) and computational speed were evaluated in their work. However, the transport of liquid water and other species was ignored.

Hosseinzadeh et al. [29] developed a 0D PEM fuel cell model to facilitate the water and thermal management for a forklift truck power system based on both theoretical and empirical equations. The balance of plant (BOP) was evaluated, including an air humidifier, a recirculation pump, a compressor, and a few heat exchangers, as shown in Fig. 10. For the fuel cell, an empirical model was employed taking oxygen partial pressure and membrane conductivity into account, while the concentration loss was not included since the high current density was not the research interest of their studies. The water transport mechanisms through the membranes via EOD effects and back-diffusion were modeled, and the mass conservation was applied. Hosseinzadeh and Rokni [30] further validated their 0D steady-state fuel cell model against stack data from Ballard Company, and parametric and sensitivity studies were performed for various operating parameters, including but not limited to anode inlet pressure, air and fuel stoichiometry ratios, and inlet coolant temperature. Long et al. [31] developed a 0D model for the hybrid system (see Fig. 11) consisting of a PEM fuel cell and a thermally regenerative electrochemical cycle to harvest the waste heat generated due to chemical reactions. The output power of the hybrid system was found to be 6–21% larger than the fuel cell system, thereby improving the performance by 3–8%.

These 0D analytical models based on simplified conservation laws were often computationally inexpensive. Although many of these models were used for energy and exergy analysis of the fuel cells or fuel cell systems, these models can be modified for model predictive control with different control objectives, e.g., energy efficiency, pressure, and temperature. However, the accuracy and the dynamic behaviors of these models remain uncertain as many of the time-dependent transport and electrochemical phenomena are not taken into account in these models.

## 5.2. Comparison of zero-dimensional analytical models

The development of 0D analytical models has been reported in various studies. A summary and comparison of these models are presented in Table 5. The majority of the 0D models are thermodynamic models to analyze the energy and exergy performance of the PEM fuel cell systems with various accessories. These models applied simple conservation laws to specific variables, and the system performance including energy conversion efficiency and exergy efficiency is evaluated, which is significant for fuel cell system design and optimization. Some studies also use 0D analytical models that do not necessarily require spatial dimensions but still need simple conservation laws to predict cell performance with fast computational speed.

These 0D analytical models based on simplified conservation laws are computationally efficient. Therefore, these models have been widely

reported in various model predictive control studies for PEM fuel cells. However, the accuracy and the dynamic behaviors remain the challenges as the spatio-temporal phenomena are not taken into account in these models [127–131].

## 6. Zero-dimensional empirical model

A 0D empirical model for PEM fuel cells in this review is classified by the involvement of curve fitting to determine the unknown coefficients of mathematical models based on experimental data.

### 6.1. Model development

Most of the empirical models attempt to establish a simple mathematical relation between the output voltage and operating current density, and most of the empirical models utilize the current density as the input and voltage as the output.

Many empirical models are developed based on the mechanistic Eq. (24) with a modification of the explicit expressions of thermodynamic potential as well as activation and ohmic over-potential, with the transport limitations incorporated into these three terms, to estimate the voltage at the low (or activation-dominated) and intermediate (or ohmic-loss-dominated) current density regions. Srinivasan et al. [24] developed the following correlation model of PEM fuel cells to predict the voltage,

$$V_{\text{cell}} = V_0 - b \cdot \log i - R \cdot i \quad (27)$$

where  $V_0 = V_r + b \cdot \log i_0$ ,  $V_r$  is the reversible cell potential,  $i_0$  and  $b$  represent the Tafel parameters that can be obtained from an experimental current-voltage curve via curve fitting, and  $R$  denotes the resistance leading to a linear change of cell potential against current density. The primary contribution to the resistance is the ohmic resistance of the membranes, followed by the charge-transfer resistance of HOR, the electronic resistance of the single cell testing facility, and the mass transport resistance in the intermediate current density region [24]. However, this equation overestimates the cell voltage at high current density regions, which is dominated by the mass transport limitation, as presented in Fig. 12. Therefore, the combination of a constant, a logarithm, and a linear term is not able to capture the rapid voltage drop at high current density regions.

Amphlett et al. [19] developed a mathematical correlation based on Ballard Mark IV fuel cell testing results, and the voltage losses were calculated based on the operational conditions, including current density, temperature, pressure, and concentration of gas species density. This enabled the empirical model with mechanistic characteristics in an attempt to optimize the performance prediction. Similarly, the cell voltage, defined as a function dependent on the thermodynamic potential, activation overpotential, and ohmic loss in their models, also accounts for the mass transport limitations being incorporated in the three terms. The activation overvoltage was dependent on temperature as well as oxygen, hydrogen, water vapor, and proton concentration.

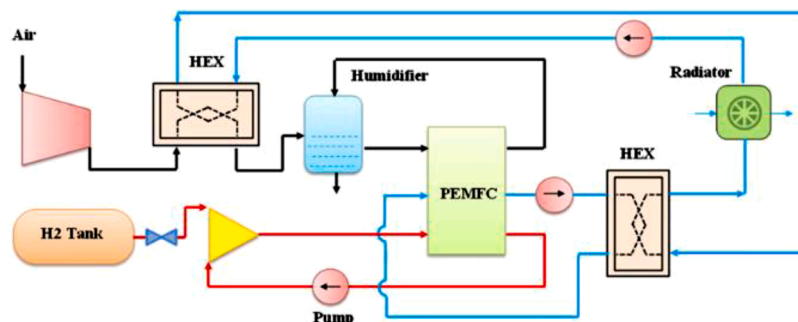


Fig. 10. Schematic of PEM fuel cell system (Reprinted from [29] with permission of Elsevier).



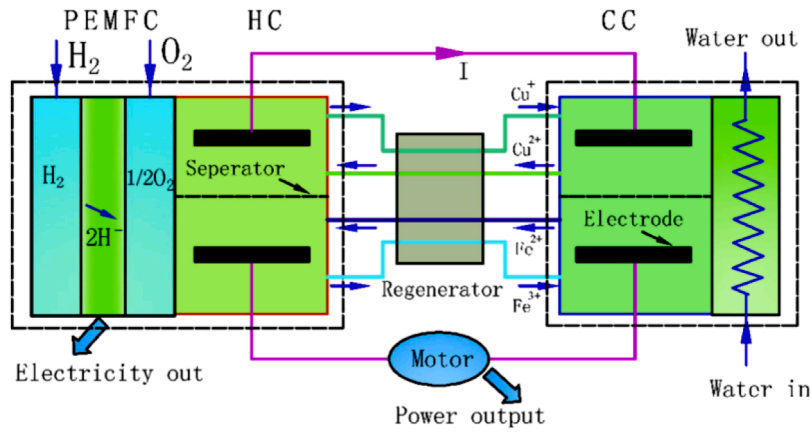


Fig. 11. Schematic of the hybrid system composed of a PEM fuel cell subsystem and a thermally regenerative electrochemical subsystem (Reprinted from [31] with permission of Elsevier).

Table 5  
Comparison of zero-dimensional analytical models for PEM fuel cells.

Model features	Cownden et al. 2001	Kazim 2004	Hussain et al. 2005	Karimi et al. 2005	Miotti et al. 2005	Elsayed Youssef et al. 2010	Musio et al. 2011	Hosseinzadeh et al. 2013	Long et al. 2015
<u>Domain</u>									
Membrane	-	-	√	-	√	√	√	-	√
CL	-	-	√	-	×	√	√	-	√
GDL	-	-	√	-	×	√	√	-	√
Flow channel	-	-	√	-	×	√	√	-	-
Bipolar plate	-	-	√	-	×	×	√	-	-
Cooling channel	-	-	√	-	×	×	√	-	√
Accessory	√	√	√	√	√	×	×	√	√
<u>Key Input variables</u>									
Reactant RH	-	√	√	√	√	√	√	√	-
Reactant temperature	-	√	√	√	×	√	√	√	-
Reactant pressure	-	√	√	√	√	√	√	√	-
Cell temperature	-	√	√	√	√	√	√	√	√
Stoichiometry ratio	-	√	√	√	√	√	√	√	-
Current density	-	√	√	√	√	√	√	√	√
<u>Physics included</u>									
Activation loss	-	-	×	-	×	√	√	-	√
Ohmic loss	-	-	×	-	×	√	√	-	√
Gas species	-	-	×	-	×	√	√	-	√
Membrane water	-	-	×	-	×	×	√	-	-
Liquid water	-	-	×	-	×	√	×	-	-
Electron transport	-	-	×	-	×	√	×	-	-
Proton transport	-	-	×	-	×	√	√	-	√
Non-isothermal	-	-	×	√	×	√	√	√	√
Convection	-	-	×	-	×	×	×	×	×
Steady-state behavior	√	√	√	√	×	√	√	√	√
Transient behavior	×	×	×	×	×	×	×	×	×
Aging effects	×	×	×	×	×	×	×	×	×
<u>Outputs reported</u>									
Voltage	-	√	√	√	√	√	√	-	√
Pressure drop	-	-	×	×	×	×	√	-	-
Energy/exergy efficiency	√	√	√	√	×	×	×	√	√
<u>Validation</u>									
Steady-state I-V curve	×	×	×	×	×	√	√	×	×
Transient voltage variation	×	×	×	×	×	×	×	×	×
Other physical variables	×	×	×	×	×	×	×	×	×
<u>Computation speed</u>	×	×	×	×	×	×	×	×	×
<u>References</u>	[21]	[22]	[15]	[26]	[27]	[23]	[28]	[29,30]	[31]

Note: √, ×, and - denote the features are included, excluded, and not mentioned in the corresponding studies, respectively.

With a few assumptions, the activation overvoltage was simplified as,

$$\eta_{act} = \xi_1 + \xi_2 T + \xi_3 T \left[ \ln(c_{O_2}^*) \right] + \xi_4 T [\ln(i)] \quad (28)$$

The ohmic overvoltage was defined as an Ohm's law expression,

$$\eta_{ohm} = iR^{internal} \quad (29)$$

where the internal ohmic resistance,  $R$ , is defined as a function of current and temperature. It should be pointed out that their models assumed that the water flooding and membrane dehydration effects were negligible, which may not be realistic for the conditions of high current density and high RH.

To further improve the performance prediction of the empirical

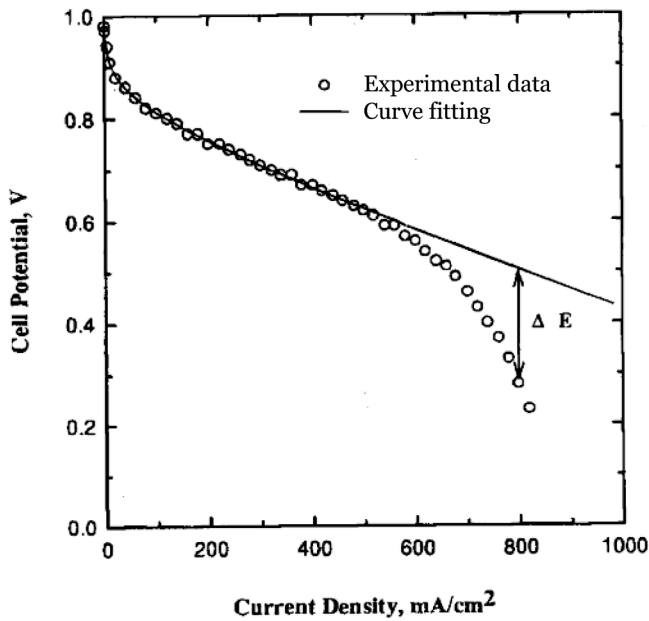


Fig. 12. Comparison of current-voltage curve predicted by Eq. (27) against experimental data - the line is Eq. (27) and the symbols are experimental data (Adapted from [18] with permission of Electrochemical Society).

models at high current density ranges by capturing the rapid voltage drop, many models introduced an artificial term to account for the impact of concentration polarization. The cell output voltage was thus modified as a function of the reversible cell potential as well as activation, ohmic, and concentration losses.

$$V_{\text{cell}} = V_{\text{rev}} - \eta_{\text{act}} - \eta_{\text{ohm}} - \eta_{\text{conc}} \quad (30)$$

The total activation loss can be calculated using the Tafel equation [16],

$$\eta_{\text{act}} = a + b \ln(i) \quad (31)$$

where  $a$  and  $b$  denote the coefficients that can be obtained by the experiment through curve fitting.

The ohmic loss is resulted from the resistance to the electron transport in electric conductors and proton migration through ionomers, and is expressed by Ohm's law [16],

$$\eta_{\text{ohm}} = (R_{\text{ele}} + R_{\text{ion}})i \quad (32)$$

where  $R_{\text{ele}}$  and  $R_{\text{ion}}$  are the electric and ionic resistances resulted from the charged species transport, and  $i$  is current density.

The concentration loss is reflected by the limiting current density [16]:

$$\eta_{\text{conc}} = \frac{RT}{2F} \ln\left(1 - \frac{i}{i_L}\right) \quad (33)$$

where  $i_L$  denotes the limiting current density, which can be determined from experimental results (see Fig. 3 for example).

With the current industry trends to run the PEM fuel cells with the high current density as a result of material breakthrough and optimization, the cell performance (voltage and power) has been steadily improved and the mass transport limitations are becoming more and more challenging. The limiting current density, as an important indicator for the overall cell performance, is limited by the capabilities of transporting the reactants in fuel cell components, and this parameter has been continuously enhanced over years as the fuel cell technology develops, as shown in Table 6.

Kim et al. [18] introduced an exponential term, compensating for the mass transport over-potential, into the voltage calculation as follows.

Table 6  
Limiting current density in different studies.

Reference	Year	Description	$i_L, \text{A}\cdot\text{cm}^{-2}$
[134]	1960	25 °C, 101 kPa, 100% RH	~0.001–0.02
[135]	1983	50 °C, 0.35 $\text{mg}_{\text{Pt}}\cdot\text{cm}^{-2}$	0.6
[136]	2000s	80 °C, 0.2 $\text{mg}_{\text{Pt}}\cdot\text{cm}^{-2}$	1.4
[137]	2006	65 °C, 310 kPa, 80%RH, high stoichiometry ratio.	3.4
[138]	2009	80 °C, 201 kPa, 100% RH, 1.5/3.0 stoich. ratio, 0.46 $\text{mg}_{\text{Pt}}\cdot\text{cm}^{-2}$	1.085
[139]	2013	Dynamic cycling	2.3
[140]	2018	80 °C, 150 kPa, 100% RH, 0.35(anode) + 0.035(cathode) $\text{mg}_{\text{Pt}}\cdot\text{cm}^{-2}$	5.4

Note:  $i_L$  denotes the limiting current density in  $\text{A}\cdot\text{cm}^{-2}$ .

$$E = E_0 - b \cdot \log i - R \cdot i - m \cdot \exp(n \cdot i) \quad (34)$$

where  $m$  and  $n$  represent the two new unknown coefficients that can be determined by curve fitting against the experimental data on cell voltage vs. current density. This model was demonstrated to show excellent correlation against the experimental data, after a careful determination of the unknown coefficients. Based on their correlation results, the values of  $m$  coefficient were in a wide range between  $10^{-19}$  and  $10^0$ , while the  $n$  coefficient remained in a narrow range. It was found that when concentration polarization is minimal, the  $m$  coefficients are between  $10^{-19}$  and  $10^{-9}$ . Therefore, high values of  $m$  and  $n$  clearly represent the over-potential dominated by mass-transport limitations.

Chu et al. [20] further extended the correlation models to a PEM fuel stack (See Eq. (35)), in which the electrode processes (activation, ohmic, and mass transfer) of the PEM fuel cell stack within the entire current density range were calculated. Their models followed a form similar to Kim et al. [18]'s work. When the current is smaller than the lower limit,  $i_d$ , which causes the output cell voltage to deviate from linearity as shown in Fig. 13, the exponential term representing the mass transport overvoltage will not be calculated; when the current exceeds the critical value,  $i_d$ , the mass transport overvoltage will be included accounting for the rapid cell performance degradation due to transport losses. It can be seen from Fig. 13 that Chu et al.'s model can better predict the output voltage than Srinivasan et al.'s models at high density regions, where concentration loss with highly non-linear behaviors is dominated.

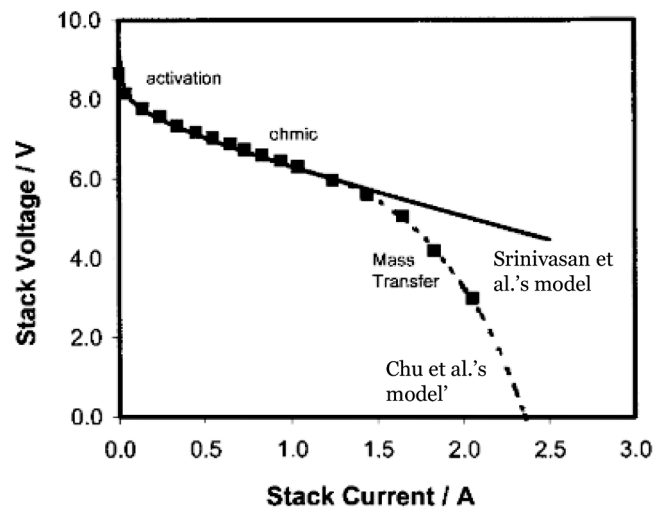


Fig. 13. Comparison with Srinivasan et al. [24]'s and Chu et al. [20]'s correlation models against experimental stack performance data (Adapted from [20] with permission of Springer).

$$E = E_0 - b \cdot \log 1000i - R \cdot i - i_m \cdot m \cdot \exp(n \cdot i_m) \begin{cases} i_m = i - i_d \text{ for } i > i_d \\ i_m = 0 \text{ for } i < i_d \end{cases} \quad (35)$$

Squadrito et al. [25] further modified the empirical model by the following equation, in which the effect of gas pressure and membrane thickness on the cell resistance was validated.

$$E = E_0 - b \cdot \log i - R \cdot i + \alpha \cdot i^k \cdot \ln(1 - \beta \cdot i) \quad (36)$$

Recently, to address the long-term performance degradation, a time-dependent term is introduced to Zhang et al.'s empirical model [16], in which the activation, ohmic, and concentration losses can be expressed in the following equations.

$$\eta_{act} = a_0 + \delta_a(\varphi)t + b_0 \ln(i) \quad (37)$$

$$\eta_{ohm} = (R_0 + \delta_R(\varphi)t)i \quad (38)$$

$$\eta_{conc} = \frac{RT}{nF} \ln\left(1 - \frac{i}{i_{L0} + \delta_L(\varphi)t}\right) \quad (39)$$

This extended PEM fuel cell model enabled the empirical models to predict the long-term performance degradation due to voltage and current cycling, even though the mechanisms were not fully addressed.

### 6.2. Comparison of zero-dimensional empirical models

Traditional empirical-correlation-based models are difficult to accurately predict all performance states of the fuel cell system with a high degree of freedom, and empirical correlations are limited in their range of applicability and validity due to the limited experimental data availability and the specific fuel cells used in the testing. In addition, the PEM fuel cell performance is sensitive to various operating conditions including current density, temperature, pressure, and RH, while most of the empirical models failed to take these factors into account, making it less representative for all operating states. A summary and comparison of these 0D empirical models are shown in Table 7. Further development of 0D empirical fuel cell models to estimate the cell performance within the whole range of operational conditions may necessitate a large number of experimental or benchmark data. However, temporal behavior modeling is one of the biggest challenges for the 0D models due to the lack of transient response mechanisms.

Although many forms of empirical correlation models have been

developed to investigate the highly dynamic and non-linear behaviors of PEM fuel cells, these models are not capable to rigorously predict the impact of different operational conditions on the cell performance, including humidity levels, pressure, temperature, and stoichiometry ratio, as well as structural parameters, including the thicknesses of components, porosity of electrodes, materials of membrane and catalyst [25]. Although these 0D empirical models can be used for real-time control of PEM fuel cells, they are only valid in a narrow operation region. In other words, these models may not be applicable to predict the cell performance over a wide operational range unless these models are rigorously validated within all operational ranges.

## 7. Data-driven model

As the experimental techniques are developed in the past several decades, a large amount of transient and steady-state experimental data have been accumulated, which allows the application of data-driven models to predict the fuel cell performances for control and diagnosis purposes [98]. The data-driven fuel cell models are classified as the models that directly learn from a large experimental data set without explicit knowledge of the physical PEM fuel cell systems. The data-driven (or non-physics-based) models can be generally classified into three categories for diagnosis purposes as shown in Fig. 14 - artificial intelligence (AI) models, statistical models, and signal-processing models. In this section, the emphasis is placed on the various artificial intelligence algorithms that can be implemented for fuel cell control applications as the application of the other two types of models in fuel cells is limited. As an alternative method, AI models can establish the relation between input variables and output performance of fuel cells by learning from existing data without knowing the physical fuel cell structure and knowledge [141,142].

### 7.1. Artificial neural network (ANN) model

The artificial neural network (ANN) model, inspired by the biological neural networks, is a powerful tool to capture the input and output relationship from a sufficiently large data set. This technology is demonstrated to be advantageous to predict the PEM fuel cell performance without knowledge of materials, structure, spatial dimensions, and complicated physical and electrochemical phenomena, and has been actively studied for the control and diagnosis of PEM fuel cells [58,

**Table 7**  
Comparison of zero-dimensional empirical models for PEM fuel cells.

Model features	Srinivasan et al.	Kim et al.	Amphlett et al.	Squadrito et al.	Chu et al.	Zhang et al.
Year	1988	1995	1995	1999	2000	2017
<u>Curve-fitting determined coefficients</u>						
# of unknowns	3	5	6	6	6	4 + 3
<u>Key input variables</u>						
Current density	√	√	√	√	√	√
Oxygen concentration	×	×	√	×	×	×
<u>Individual terms representing physics</u>						
Activation loss	√	√	√	√	√	√
Ohmic loss	√	√	√	√	√	√
Concentration loss	×	√	×	√	√	√
Aging effect	×	×	×	×	×	√
<u>Outputs</u>						
Voltage	√	√	√	√	√	√
Outlet pressure	×	×	×	×	×	×
Outlet species composition	×	×	×	×	×	×
Outlet species flow rate	×	×	×	×	×	×
Outlet temperature	×	×	×	×	×	×
<u>Validation/Evaluation</u>						
Steady-state I-V curve	√	√	√	√	√	√
Ohmic resistance	×	×	√	√	×	×
<u>Computation speed</u>						
Computation speed	×	×	×	×	×	×
<u>References</u>	[24]	[18]	[19]	[25]	[20]	[16]

Note: √ and × denote the features are included and excluded in the corresponding studies, respectively.

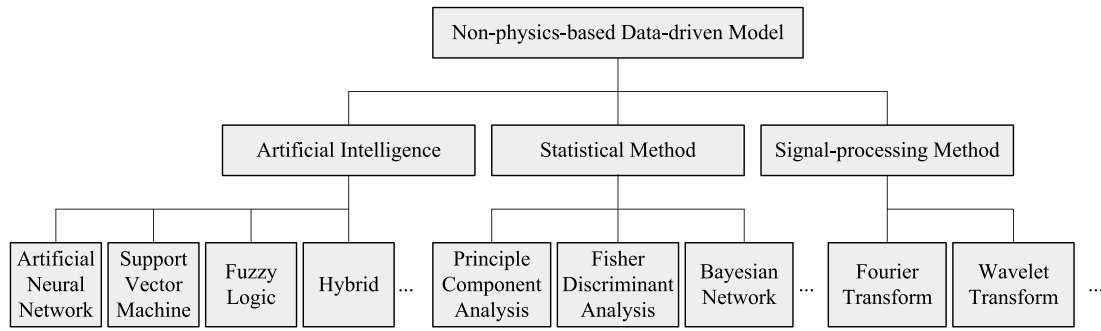


Fig. 14. Classification of non-physics-based data-driven fuel cell models for diagnosis purpose (Adapted from [58] with permission of Elsevier).

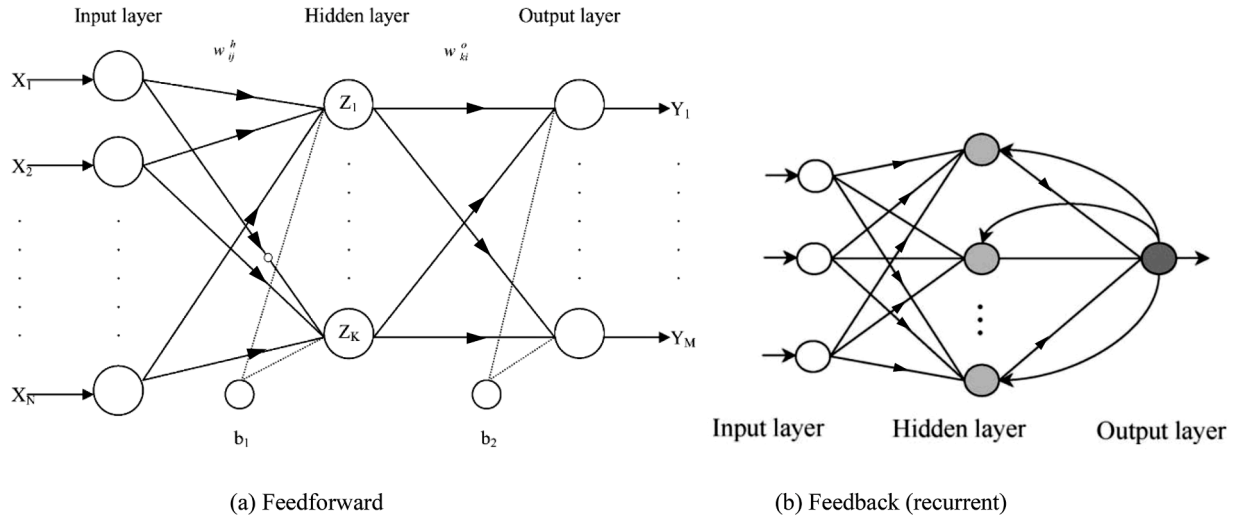


Fig. 15. Example of (a) feedforward multilayer neural network (Adapted from [143] with permission of Elsevier) and (b) recurrent (or feedback) neural network (RNN) architecture with a single hidden layer (Adapted from [147] with permission of Elsevier).

[143,144]. Various ANN models have been proposed for different energy applications. Based on the topology, the connections of neurons can be feedforward (see Fig. 15a) and feedback (or recurrent) (see Fig. 15b). Feedforward networks do not contain cycles in the connections of neurons, while feedback (or recurrent) connection includes cycles between neurons. The numbers of layers and neurons are dependent on the complexity of the problem being solved and determine the ANN prediction performance, which is often determined by trial and error during learning/training processes [143]. However, the trial and error method is time-consuming and skill-dependent. Recently, the method of neural architecture search (NAS) has been developed to automatically search for the most suitable neural network architecture [145]. The learning (or training) process of the ANNs can be supervised or unsupervised depending on if the learning requires a teacher. The supervised learning links the inputs with target outputs that supervise the learning process, while the unsupervised learning will recognize patterns in the input data, and a target output is not required. The input data are usually divided into two sets for the supervised learning – training dataset and testing/validation dataset. The training dataset is used for the ANN learning by adjusting the weights of links among different neurons, which are constantly updated as the learning proceeds. The testing/validation dataset is utilized to evaluate the performance of ANN models [17,57,146].

Various ANN architectures have been investigated for PEM fuel cell modeling. Sisworahardjo et al. [17] proposed a multilayer feedforward ANN fuel cell model with the training algorithm of back-propagation based on a 100 W portable PEM fuel cell, as shown in Fig. 16. Their model was trained for 10 thousand epochs (each epoch means the model

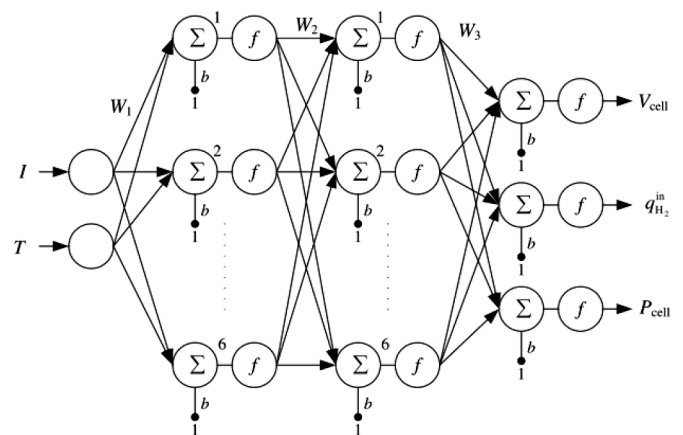


Fig. 16. Artificial neural network model based on a 100 W PEM fuel cell (Reprinted from [17] with permission of Elsevier).

is trained with the entire dataset once) and compared with a dynamic physics-based model and experimental data. Three statistical indices were defined to evaluate the accuracy, precision, and variation for cell voltage, output power, and flow rate of hydrogen. Their modeling results indicated that the ANN model is more advantageous in precision and accuracy but presents a bigger variation in the predicted variables in comparison with the dynamic model.

Ma et al. [144] developed a fuel cell degradation model adopting a

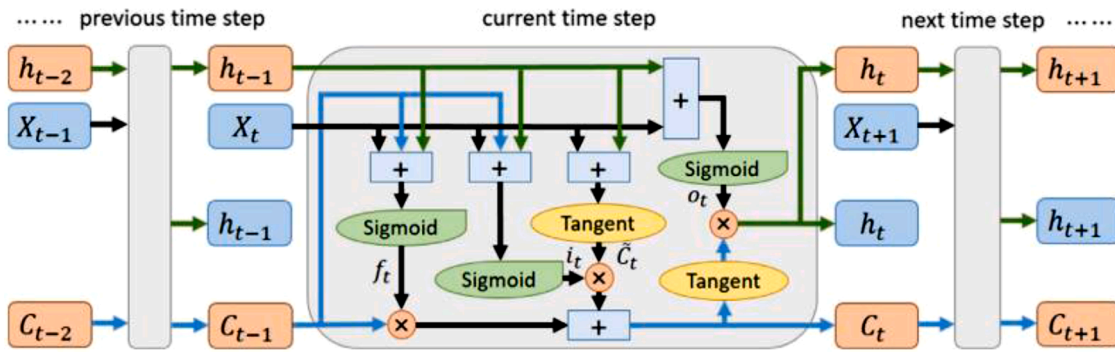


Fig. 17. Architecture for long short-term memory (LSTM) cell (Reprinted from [144] with permission of Elsevier).

Grid Long Short-Term Memory (G-LSTM) recurrent neural network (RNN) to avoid the problems of gradient exploding and vanishing in comparison with traditional RNN architecture, as shown in Fig. 17. This enabled the model to estimate the long-term cell performance, which was validated against three groups of fuel cell data from a Ballard Nexa fuel cell (1.2 kW) and two Proton Motor fuel cells (1 kW and 25 kW).

Sari et al. [57] developed a multilayer feedforward back-propagation ANN model utilizing the Levenberg-Marquardt algorithm for training (similar to Newton’s method), which is efficient and easy for implementation. The inputs of their models included fuel cell current ( $I_{FC}$ ), sampling delayed current, sampling delayed voltages ( $U_{FC}$ ), and the corresponding voltage and current differences, and the output was the cell voltage.

Chávez-Ramírez et al. [146] developed an ANN model with seven input variables (including current, air flow rate, hydrogen flow rates, nitrogen flow rates, cathode water injection, anode inlet temperature, and bulk water temperature) and two output variables (including stack voltage and cathode outlet temperature) to evaluate a 5 kW PEM fuel cell stack (see Fig. 18). The maximum output prediction errors were found to be around 9 % in the stack potential and 6% in the operating temperature, respectively.

Hatti et al. [148] developed an ANN model with four input variables (including temperature, current, hydrogen and oxygen pressures), a hidden layer of neurons, and an output variable (cell voltage) to study

the static performance of PEM fuel cells. The comparison with the empirical models suggested a good agreement with the current-voltage curves at various pressures; however, no quantitative evaluation of the ANN model performance was reported. Hatti and Tioursi [149] developed a dynamic neural network (DNN) by incorporating a delay line for the inputs, as shown in Fig. 19. This enabled the DNN model to predict the transient cell performance, even though the physical variables used for the inputs and outputs were not explicitly explained.

Vichard et al. [150] developed an Echo State Neural Network (ESNN) model (see Fig. 20), which is a type of RNN, to predict the long-term performance of PEM fuel cells based on their 5000 h experimental data. In their model, three variables, including environment temperature, operation time and stack voltage at previous state, were used as inputs. This enabled the prediction of stack voltage at the current state when the operation time was sufficiently long with a large dataset for training and testing. Their modeling results indicated that the learning rate (i.e., percentage of data used for training) had a significant impact on the modeling accuracy, as shown in Fig. 21. An obvious bias of voltage prediction was found after around 1600 h of operation when only 33% of the entire data were used for training (see Fig. 21a). When the training rate was increased to 60%, the predicted stack voltages agreed well with the experimental data after around 3200 h of operation (see Fig. 21b). It should be noted that the computation time for building their model was around 2 s in the environment of Windows 10 system

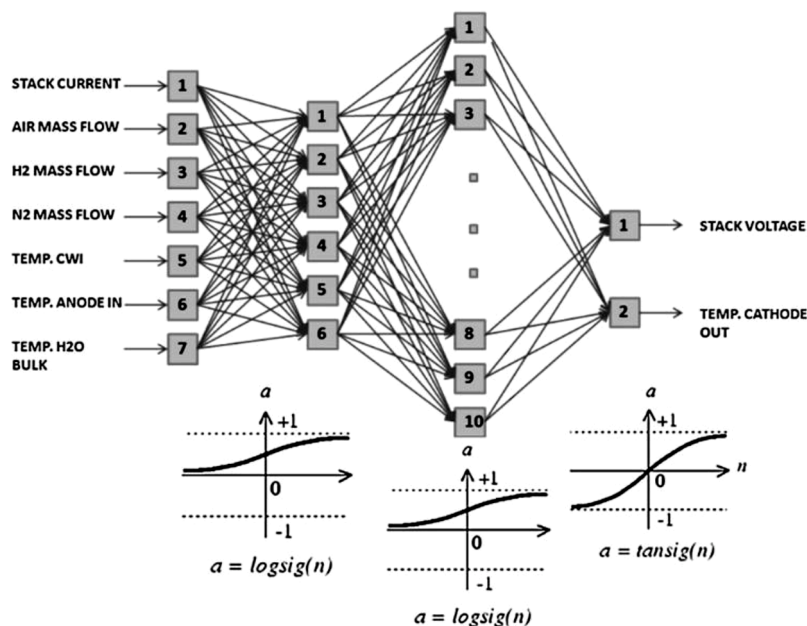


Fig. 18. An optimized architecture of artificial neural network for PEM fuel cell modeling with seven input variables, two hidden layers, and two output variables (Reprinted from [146] with permission of Elsevier).

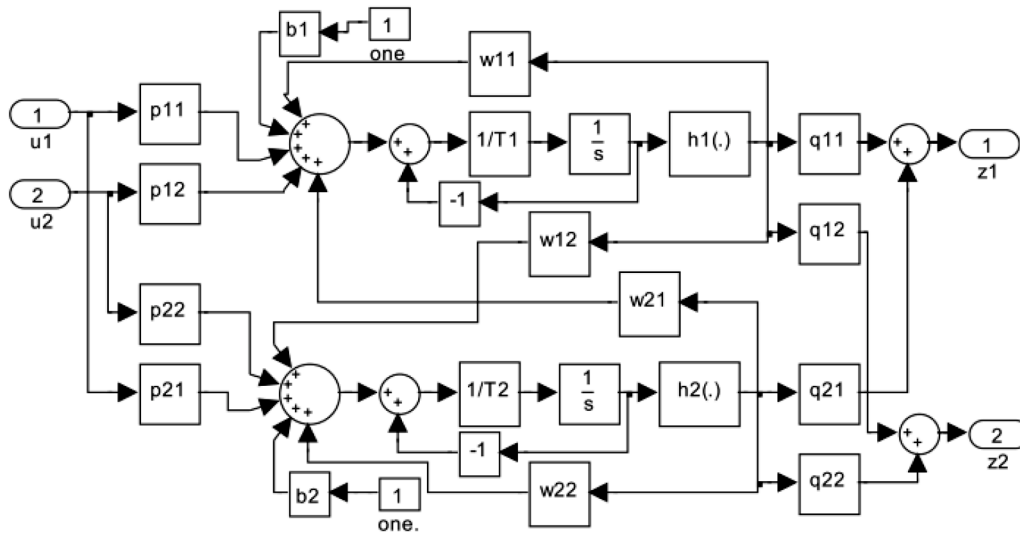


Fig. 19. The state diagram of dynamic neural network with two neurons, two inputs, and two outputs based on Matlab/Simulink (Reprinted from [149] with permission of Elsevier).

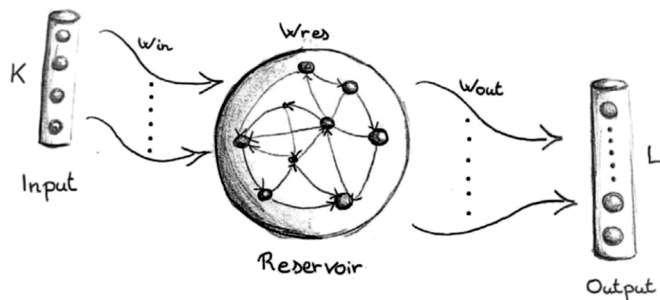


Fig. 20. Schematic of Echo State Neural Network (ESNN) (Reprinted from [150] with permission of Elsevier).

with a 3.4 GHz CPU, a NVIDIA GPU and 64 G memory, which is suitable for real-time control.

7.2. Fuzzy logic (FL) model

Data-driven fuzzy logic (FL) models can also be used for fuel cell

control and diagnosis [58]. The key idea of an FL model is to allocate the data points into several clusters and the data points possessing the most similarities will be assigned into the identical cluster. Fig. 22 shows a schematic of three fuzzy clusters ( $c_1, c_2$  and  $c_3$ ) on a 2D feature space ( $f_1$  and  $f_2$ ). In the fuel cell applications, each cluster can represent one type of failure mode, and each data point can be a vector of a certain amount of features related to the failure mode.

Tekin et al. [151] developed a new energy management approach for a 5 kW PEM fuel cell based on fuzzy logic algorithm. Two fuzzy logic controllers were investigated in their studies for efficient energy management strategies. The first fuzzy logic controller was used for the airflow control loop, which allows an energy consumption reduction in comparison with conventional linear-control strategies. The second fuzzy logic supervisor was adopted to determine the airflow set point. Five input variables (including voltage and its time derivative, current and its time derivative, and time derivative of the requested power), a fuzzy logic controller, and an output variable (airflow reference output) were involved in their model, which was advantageous in fault management and energy consumption of the fuel cell system.

Hissel et al. [152] developed a fuzzy-clustering method based on a 2D space of two variables extracted from the Nyquist plots of

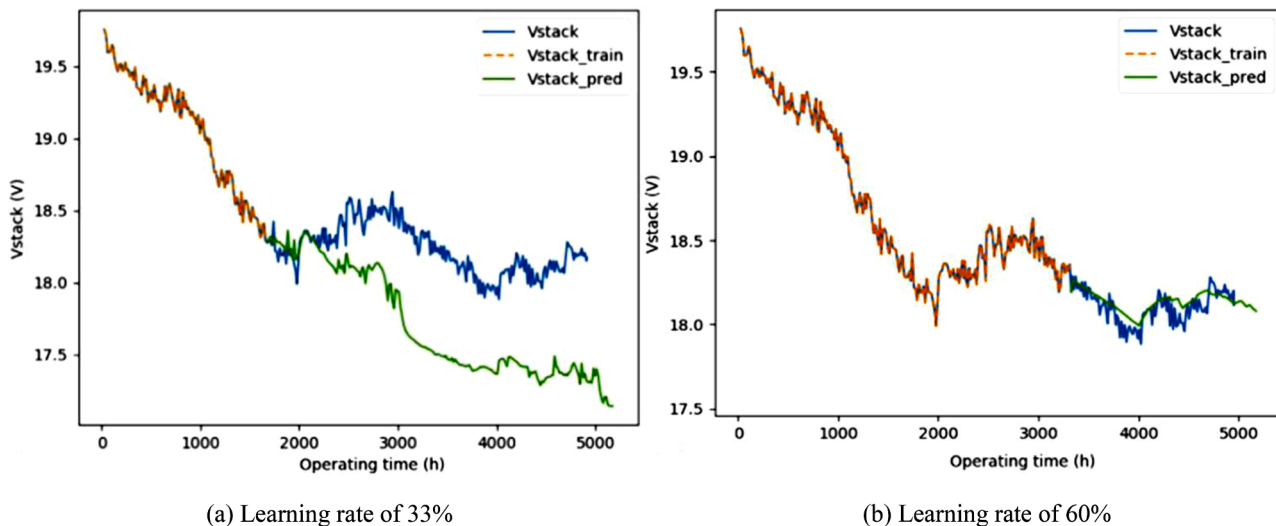


Fig. 21. Performance of Echo State Neural Network (ESNN) with various learning rates of (a) 33% and (b) 60% (Reprinted from [150] with permission of Elsevier).

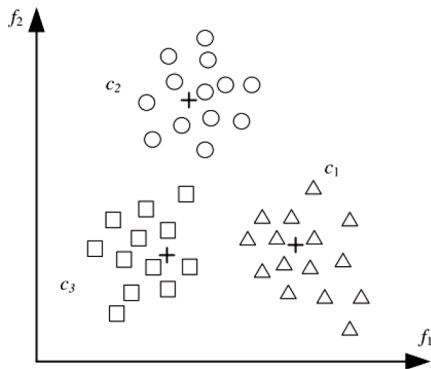


Fig. 22. Fuzzy clustering diagram (Reprinted from [58] with permission of Elsevier).

electrochemical impedance spectroscopy (EIS) results obtained from a steady-state current operation and a current-cycling operation based on real transportation loads of the PEM fuel cells. These two variables included the difference between voltage loss and internal resistances and the maximum absolute phase value of the Nyquist plots for the fuel cell stack under study. The fuzzy-clustering method was adopted to recognize the clusters related to specific aging effects. Their model was able to distinguish normal fuel cell operation, abnormal operation, and the states in transition. Therefore, it is of potential to be applied to the real-time control of PEM fuel cell powertrain [152].

### 7.3. Support vector machine (SVM) model

The support vector machine (SVM) model, as a supervised learning model, has been recently incorporated into fuel cell modeling for control purposes with designed inputs, including current, reactant flow rates, pressure, and temperature.

Zou et al. [153] developed a least squares support vector machine (LS-SVM) algorithm (see Fig. 23) for the high-temperature PEM fuel cells to investigate temperature distribution under dynamic operations. Ten thermocouples were placed in a fuel cell stack (see Fig. 24a) to record the temperature variation against time with sampling intervals of 20 s. The datasets T1,T2,T4,T5,T7,T8 and T10 were used for model training,

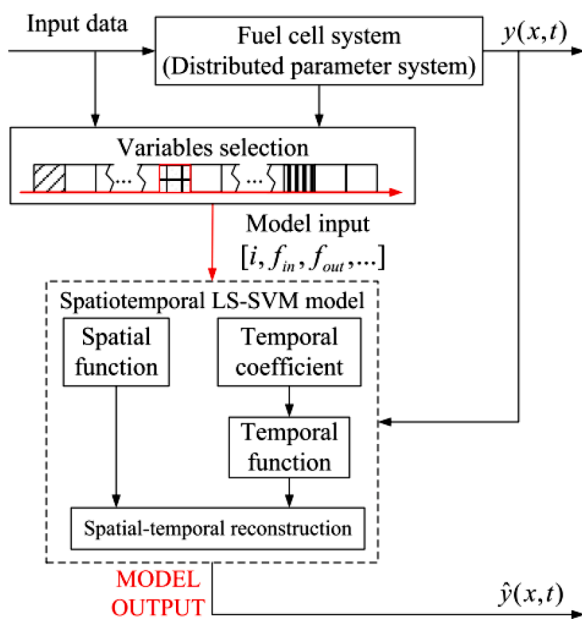


Fig. 23. Framework of spatiotemporal least square support vector machine (LS-SVM) method (Reprinted from [153] with permission of Elsevier).

and datasets T3,T6 and T9 are used for testing the prediction. It can be seen that the LS-SVM was able to capture the temporal behavior of the temperature evolution with very good accuracy (errors are typically lower than 1.2%), as shown in Fig. 24b and c.

Wu et al. [154,155] developed a self-adaptive approach of relevant vector machine (RVM) model which was trained against experimental data on cell voltage degradations based on a 1.2 kW and a 8 kW PEM fuel cell stack. In comparison with the classic SVM, the RVM method presents better predictive performance. For most cases, the prediction errors of RVM were reported 30%–40% lower than that of classic SVM. The improved performance of RVM in comparison with SVM was attributed to its probabilistic prediction, no limitation on kernel function selection, and efficient computation during regression or classification, making RVM particularly suitable for real-time control and prognosis [155].

### 7.4. Physics-informed data-driven model

The physics-informed data-driven model incorporates available and often incomplete physics knowledge into data-driven models to avoid unreliable results caused by improperly or insufficiently trained data-driven models and to accelerate the computing speed of physics-based models [156–159].

Raissi et al. [156] developed a physics-informed ANN model that is suitable for multi-physics multi-scale physical phenomenon modeling and model predictive control. Their results indicated that a physics-informed neural network is capable of encoding a physical phenomenon that is governed by partial differential equations, e.g., the Navier-Stokes equation in computational fluid dynamics. The method can be potentially used to investigate fuel cell performance by incorporating one or more governing equations, such as momentum equation, energy equations, reactant and water transport, and the Butler-Volmer equation, into the neural networks. The details of the major physical phenomena in PEM fuel cells that can be implemented by physics-informed models are summarized in [157]. Although these models have not been applied for PEM fuel cell performance simulation, they may be beneficial not only for fuel cell control but also for component design and optimization [157].

### 7.5. Data-driven reduced-order model

Data-driven reduced-order models can be composed of a computationally intensive offline phase and an efficient online phase that can be used for fast predictions of system characteristics [160]. Many model reduction techniques, including proper orthogonal decomposition (POD) [161,162], principal component analysis (PCA) [163], and the Karhunen-Loève method [164,165], have been developed in various applications [162,166]. These methods have a promising potential to accelerate the computing speed of original high-fidelity PEM fuel cell models.

Lei et al. [164] developed a reduced-order coarsening model by applying a Gaussian process stochastic function to address the Ostwald ripening mechanism of the catalyst particle growth. This model is used to estimate the microstructure evolution of the electrodes in solid oxide fuel cell (SOFC) with enhanced computing speed and excellent agreement with the experimental datasets. Li et al. [163] performed a comparative study on the data-driven diagnosis methods for PEM fuel cells. Four automatic feature extraction methods, including PCA, Fisher Discrimination Analysis (FDA), Kernel PCA, and Kernel FDA, combined with three classification methods, including Gaussian Mixture Model (GMM), k-Nearest Neighbor (kNN), and SVM are incorporated in the framework of the diagnosis approach (see Fig. 25) and compared in their studies. Based on the computing cost of online diagnosis performance (time for offline training was not considered), the models using FDA combined with SVM classifier are recommended for the best performance.

Although reduced-order models have not been widely applied to the

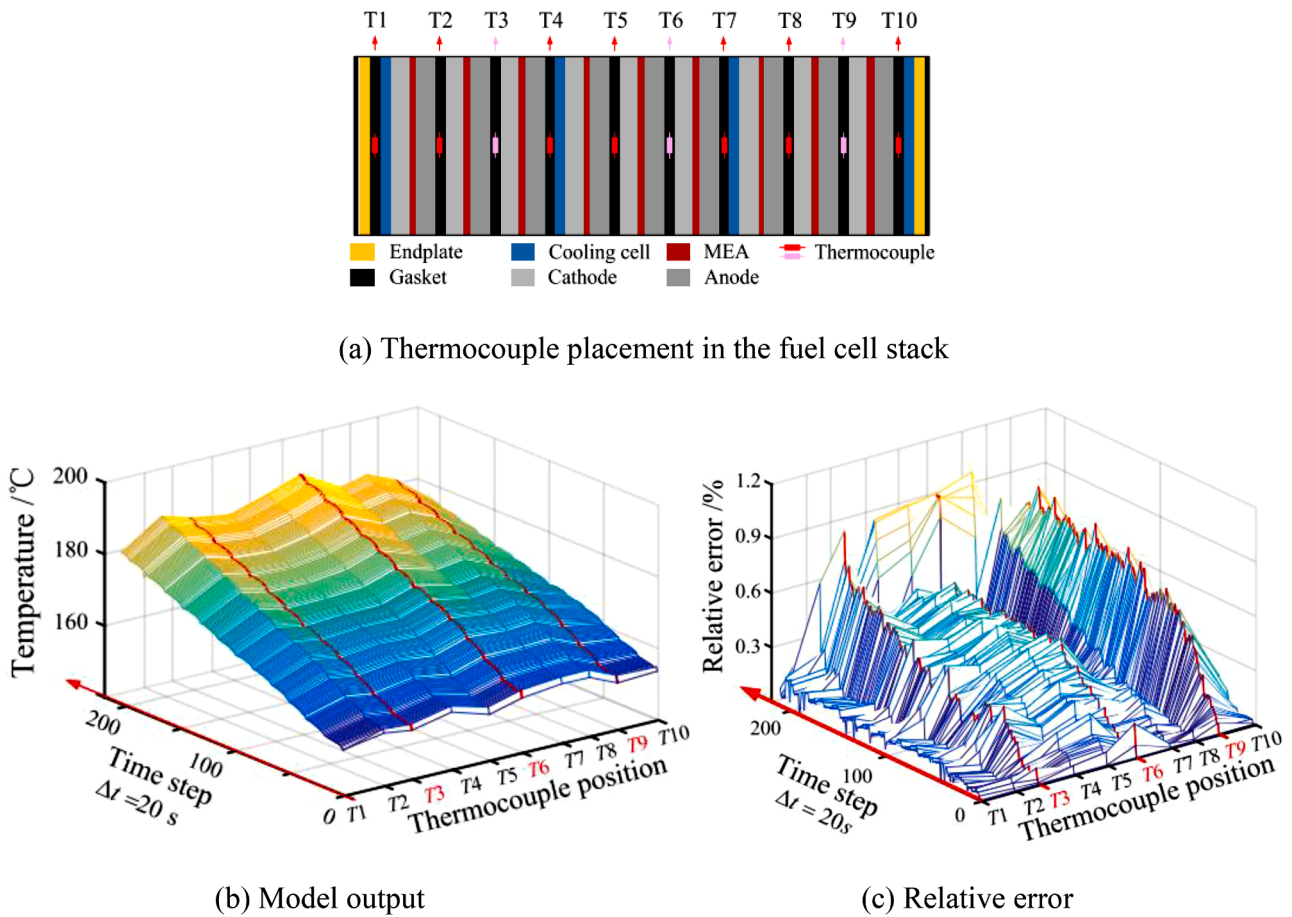


Fig. 24. Validation of spatiotemporal least square support vector machine (LS-SVM) method based on a PEM fuel cell stack with dynamic temperature distribution: (a) Thermocouple placement in the fuel cell stack, (b) Model output, and (c) Relative error (Training datasets: T1–T10; testing datasets: T3,T6,T9) (Reprinted from [153] with permission of Elsevier).

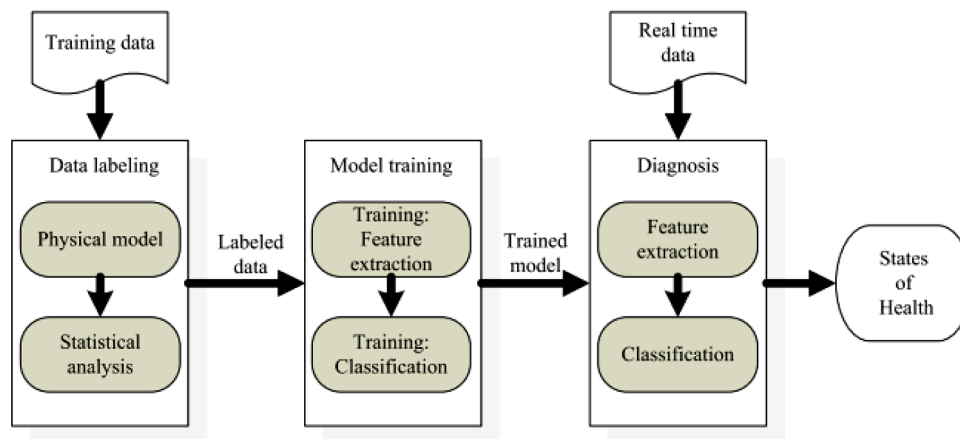


Fig. 25. The framework of the diagnosis approach proposed by Li et al. (Reprinted from [163] with permission of Elsevier).

real-time control of PEM fuel cells, they have become a viable option to minimize the required computing resources while predicting high-fidelity dynamic PEM fuel cell behaviors.

### 7.6. Comparison of data-driven models

Data-driven models, with an emphasis on artificial intelligence algorithms, are advantageous to build the input-output relationships of a given big dataset [167–169], which makes the real-time performance

prediction of PEM fuel cells possible. There exist various data-driven models developed for fuel cell control, and a summary and comparison of these models are presented in Table 8. It can be seen that data-driven models are advantageous in computational speed and prediction accuracy without the requirement of physical knowledge. Ou and Achenie [143] claim that the training time required for an ANN model is comparable to that needed to set up a physical model, but once trained, the ANN model will be much faster for computing. However, little information about the computational resources and time needed



**Table 8**  
Comparison of zero-dimensional data-driven models for the control of PEM fuel cells.

Model Features	Ou and Achenie	Hatti et al.	Tekin et al.	Hissel et al.	Sisworahardjo et al.	Chávez-Ramírez et al.	Sari et al.	Silva et al.	Wu et al.	Ma et al.	Zou et al.	Vichard et al.
Year	2005	2006	2007	2007	2010	2010	2013	2014	2016	2018	2019	2020
Algorithm	Neural-physical	ANN	Fuzzy logic	Fuzzy-clustering	ANN	ANN	ANN	Fuzzy Neural	RVM	RNN	SVM	ESNN
<u>Inputs</u>	6	4			2	7	8	4				3
Current density	√	√	-	-	√	√	√	-	-	-	-	×
Cell temperature	√	√	-	-	√	×	×	-	-	-	-	×
Concentration of methanol	√	×	-	-	×	×	×	-	-	-	-	×
Methanol flow rate	√	×	-	-	×	×	×	-	-	-	-	×
Pt loading	√	×	-	-	×	×	×	-	-	-	-	×
Pt/C ratio	√	×	-	-	×	×	×	-	-	-	-	×
Hydrogen pressure	×	√	-	-	×	×	×	-	-	-	-	×
Oxygen pressure	×	√	-	-	×	×	×	-	-	-	-	×
Air mass flow rate	×	×	-	-	×	√	×	-	-	-	-	×
Hydrogen mass flow rate	×	×	-	-	×	√	×	-	-	-	-	×
Nitrogen mass flow	×	×	-	-	×	√	×	-	-	-	-	×
Cathode water injection rate	×	×	-	-	×	√	×	-	-	-	-	×
Anode temperature	×	×	-	-	×	√	×	-	-	-	-	×
Bulk water temperature	×	×	-	-	×	√	×	-	-	-	-	×
Ambient temperature	×	×	×	×	×	×	×	×	×	×	-	√
Voltage	×	×	×	×	×	×	×	×	×	×	-	√
Time	×	×	×	×	×	×	×	×	×	×	-	√
<u>Outputs</u>	1	1			3	2	1	1				1
Cell voltage	√	√	-	-	√	√	√	-	-	-	-	√
Power	×	×	-	-	√	×	×	-	-	-	-	×
Hydrogen flow rate	×	×	-	-	√	×	×	-	-	-	-	×
Cathode temperature	×	×	-	-	×	√	×	-	-	-	-	×
Temperature	×	×	-	-	×	×	×	-	-	-	√	×
<u>Architecture</u>												
Number of hidden layers	1	1	-	-	2	2	2	3	-	-	-	-
Number of neurons	-	30	-	-	6 + 6	6 + 10	18 + 18	-	-	-	-	-
<u>Training and testing</u>												
Training data percentage	75%	-	-	-	-	50%	70%	-	-	-	70%	60%
Testing data percentage	25%	-	-	-	-	25 + 25%	30%	-	-	-	30%	40%
<u>Physics included</u>												
Steady-state behavior	√	√	-	-	×	×	×	-	-	-	-	×
Transient behavior	×	×	-	-	√	√	√	-	-	-	√	√
Aging effects/online learning	×	×	-	-	×	×	×	-	-	√	√	×
<u>Validation</u>												
Voltage	√	√	-	-	√	√	√	-	-	-	√	√
Other variables	×	×	-	-	√	√	×	-	-	-	-	×
<u>Computation speed</u>	×	×	×	×	×	×	×	×	×	×	×	√
<u>References</u>	[143]	[148]	[151]	[152]	[17]	[146]	[57]	[170]	[154, 155]	[144]	[153]	[150]

Note: √, ×, and – denote the features are included, excluded, and not mentioned in the corresponding studies, respectively. Model Accuracy and Computing Speed

for training is reported in the literature [17,143,148,151,152]. Further studies should take into account as many controllable operating variables and design parameters as possible for the data-driven model development. Models with capabilities to predict more output variables, including voltage, temperature, and outlet conditions, will be advantageous for the fuel cell stack and system control. Online learning algorithms will be of particular interest in industry such that the long-term performance can be estimated. However, the data-driven model development requires a large amount of experimental data, and the effect of

data quality on the data-driven model performance will be of particular research interest.

### 8. Model accuracy and computing speed

The prediction accuracy and computing speed are evaluated with different reported metrics in various fuel cell models, including physics-based and data-driven models. A detailed comparison of model accuracy and computing speed reported in literature is presented in Table 9.

**Table 9**  
Comparison of reported accuracy and computing speed of various PEM fuel cell models.

Ref.	Model	Computing resources	Computing speed	Accuracy evaluation	Remarks
[171]	3D	CPU: Intel (R) Xeon (R) E5-2650 v4 2.20 GHz 24 threads, Four-process parallel computing	8–12 h per scenario	N/A	331,800 structured volume grid cells; 4200 surface grid cells in the activation plane.
[67]	3D	Beowulf cluster system with 8 CPUs	1143–1317 min (assuming 1000 iterations)	N/A	Fluent; 25 parallel channels; 2.2 million nodes.
[172]	1D+3D	Intel Core i7-2600 K @ 3.40 GHz CPU (all 8 processes used) and 8 GB RAM	> 2 months	Polarization curve	Unsteady state; Volume of fluid (VOF) method for air-water two-phase flow in cathode channel.
[67]	2D	N/A	733–808 s/case	N/A	Comsol
[45]	Pseudo-2D	2.4 GHz CPU	~611 s (equivalent to 1200 seconds operating time)	Qualitative agreement with published experimental data	Transient model
[173]	Pseudo-2D	Linux PC cluster built by 10 P-4 CPUs with 20GB of main memory	~30 min	N/A	51 cells; U and Z stack configuration.
[55]	1D	Pentium-D Processor 2.2 GHz, memory 1 GB	33% faster than the real time (e. g., 344 s simulation time vs. 421 s real time)	Compared with experimental data on temperature and voltage variation	Dynamic model
[150]	RNN	CPU Intel core I7-6800k 3.40 GHz, GPU NVIDIA TITAN X, 64 GB of memory.	~2 s (equivalent to 2000 h operating time)	N/A	Degradation of fuel cell system
[174]	SVM	N/A	< 1 s for each polarization curve 10,000 times faster than physical model	root mean squared error, RMSE (0.99) squared correlation coefficient (0.06) mean percentage error (3.3%) maximum percentage error (7.7%)	compared with single cell 3D physical model
[171]	ANN and SVM	Lenovo X1 Yoga, CPU: Intel(R) Core i7-6600 U 2.60 GHz	< 1 s per scenario	root mean squared error, RMSE relative root mean square errors, rRMSE (3.88%- 24.80%)	5250 data points in the training set 1750 data points in the test set compared with 3D physical model
[175]	SVM	PIII 800 MHz computer	training time ~ 30 ms (1583 iterations) prediction time ~ 10 ms	No quantitative evaluation is reported.	~ 130 data points of voltage-current relation
[176]	N/A	80–300 MHz CPU speed 1.5–8 Mb flash memory	N/A	N/A	Bosch fuel cell controller

Most of the physics-based models evaluate the accuracy by comparing the I-V curve (polarization curve), which is known as the validation of models. For instance, Shamardina et al. [123] validated their pseudo-2D model by an experimentally measured polarization curve, while Yang et al. [91,125] validated their pseudo-2D transient model against two steady-state polarization curves under different stoichiometry ratios from published experimental data. The steady-state I-V curves are also commonly used for the validation of 1D models [10, 51,53,54,56,103] and 0D analytical models [23,28]. Some other variables are also used for model validation, including transient voltage [47, 48,91], coolant temperature [91], and resistance [14]. Although most physical models claimed that their modeling results agree well with experimental data, their models are only validated against one or a few polarization curves, which is often valid in a narrow range of fuel cell operational conditions. Moreover, most studies only present a comparison of modeling results with experimental data, while statistical indicators were rarely reported in the literature to quantify the errors in modeling work. The computing speed of a steady-state model can be evaluated by the computing time required to calculate a single case, while for a transient model, the computing speed can be quantified in comparison with the real operation time. For instance, Shamardina et al. [123]'s steady-state model requires a few seconds of computing time for a single case based on a personal computer, while Goshtasbi et al. [45, 126]'s transient pseudo-2D model takes 611 s to calculate a physical operation of fuel cell for 1200 s, which means the computing speed is two times faster than real-world applications. The computational time also depends on the fuel cell controller used for the control, while the actual physical time for a particular fuel cell set depends on the fuel cell design, structure and operation condition. However, the details of electronic control units and fuel cells are often kept confidential by the fuel cell developer.

0D empirical models rely on a relatively larger experimental dataset to determine empirical coefficients in various models, and the prediction performance is usually good within the narrow range of data used for

curve fitting [16,18–20,24,25]. Although most studies on 0D empirical models did not report the calculation speed, the computing speed is generally believed to be much faster than pseudo-2D numerical, 1D numerical, and 0D analytical models as most 0D empirical models only involve one or a few algebraic equations and do not resolve spatially dependent variables [45]. However, the simplistic nature of 0D empirical models makes them less trustworthy to predict the performance beyond the data range used for coefficient determination, and it is almost impossible to calculate other performance indicators other than voltage by 0D empirical models.

Data-driven models require the largest dataset for model training and testing among all the fuel cell models. Wang et al. [157] developed a data-driven surrogate SVM model trained with simulation data generated by a 3D fuel cell model taking CL agglomerate into account. 50 data points were used for training, and 15 data points were used for testing. The predicted current density,  $I_i$  [ $\text{A}\cdot\text{cm}^{-2}$ ], is evaluated by four parameters, including root mean squared error, RMSE [ $\text{A}\cdot\text{cm}^{-2}$ ], squared correlation coefficient ( $R^2$ ), mean percentage error,  $\delta_{\text{mean}}$ , and maximum percentage error,  $\delta_{\text{max}}$ , as shown below:

$$RMSE = \sqrt{\frac{1}{n} \sum_{i=1}^n (I_i - I'_i)^2} \quad (40)$$

$$R^2 = 1 - \frac{\sum_{i=1}^n (I_i - I'_i)^2}{\sum_{i=1}^n (I_i - \bar{I}_i)^2} \quad (41)$$

$$\delta_{\text{mean}} = \frac{1}{n} \sum_{i=1}^n \frac{|I_i - I'_i|}{I_i} \times 100\% \quad (42)$$

$$\delta_{\text{max}} = \max \left\{ \frac{|I_i - I'_i|}{I_i} \right\} \times 100\% \quad (43)$$

where the subscript  $i$  means the  $i^{\text{th}}$  data point,  $n$  is the total number of

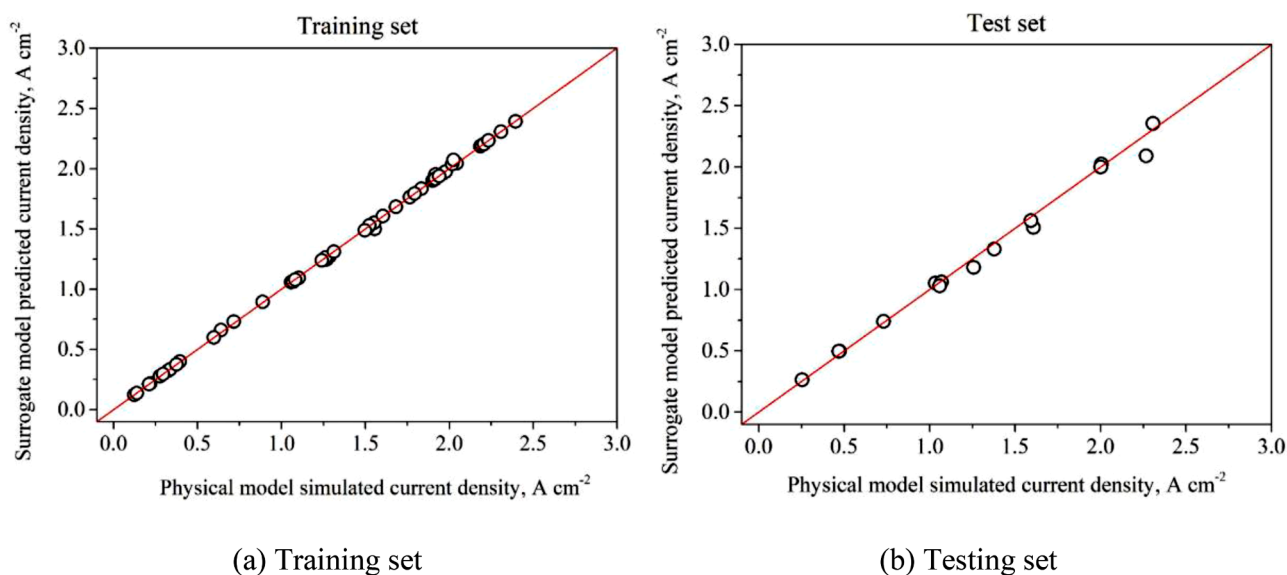


Fig. 26. Comparison of the current density predicted by data-driven model and physical model for (a) training set and (b) testing set by Wang et al. (Reprinted from [157] with permission of Elsevier).

data points,  $I_i$  is the current density predicted by the 3D model, and  $\bar{I}_i$  is the average current density in the dataset. The prediction performance is shown in Fig. 26. The  $R^2$  value in the training and testing datasets is 0.9996 and 0.9908, respectively, which are sufficiently high for most applications. The maximum percentage error is reported to be 7.7% in the test dataset and 3.6% in the training set. Therefore, the data-driven model demonstrates comparable accuracy with the physical model. Wang et al. [171] further built a two-hidden-layer ANN model and an SVM model to test a larger dataset generated by 3D models (5250 data points for training and 1750 data points for testing). The prediction results are evaluated by RMES and relative RMES, and both ANN and SVM demonstrate similar accuracy in comparison with 3D physical models. The computing time for data-driven models is within 1 s, while the 3D physical model requires 8–12 h per scenario by four-processor parallel computing (See Table 9 for more details). The computing speed of the data-driven models depends on not only the algorithm, but also the number of input and output variables, the size of the dataset, and the complexity of data structure. However, most of the data-driven models for fuel cells did not report the computing time for model training, and the computing speed is often reported when the model is used for performance prediction.

## 9. Challenges and future prospects

A typical PEM fuel cell stack, as a promising alternative power source, consists of hundreds of single cells, and the performance of a particular fuel cell system is determined by many operating variables, including but not limited to reactant composition, temperature, pressure, relative humidity, flow rate, and cooling conditions. Therefore, it is challenging to predict all states of this high degree of freedom system with sufficient accuracy and computing speed over the entire operational range, which requires significant improvement of the reduced-dimensional physics-based or data-driven models in the following aspects (see Fig. 27 and Table 10):

### a Model accuracy

For physics-based models, the accuracy depends on the details of multi-dimensional transport and electrochemical phenomena included in the model, such as two-phase flow, temperature variation, ice formation, and aging effect. Due to the limitation of computing resources

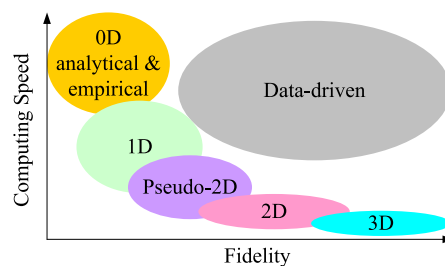


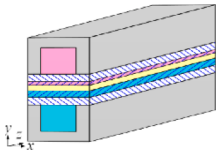
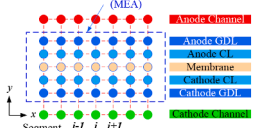
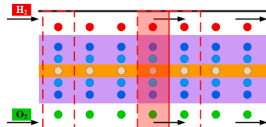
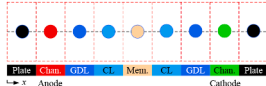
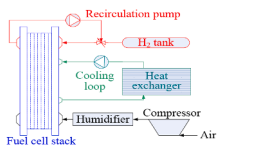
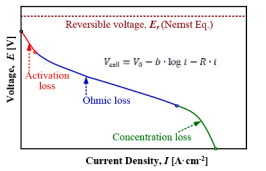
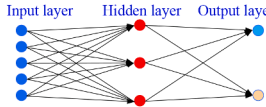
Fig. 27. Comparison of multi-dimensional physics-based and data-driven fuel cell models.

for the currently available electronic control unit (ECU) (see Table 9), significant simplifications have to be made to reduce the dimension of the physical problems and the complexity of the corresponding governing equations based on reasonable assumptions. It is expected that 3D and 2D models are generally able to predict with higher fidelity than 1D and 0D models since they are more realistic and can capture more details of the transport and electrochemical phenomena in the fuel cells. Model accuracy is also affected by various transport coefficients and properties in different fuel cell components, including membrane, catalyst layers, gas diffusion layers, flow channels, and distribution plates. These coefficients and properties significantly vary in different numerical studies, and further experimental efforts are required to eliminate this discrepancy. Furthermore, model accuracy can be improved by incorporating multiple aging effects, including mechanical, thermal, and electrochemical degradations, to predict performance degradation in a long-term manner.

For data-driven models, the accuracy depends on not only the training algorithm and model architecture but also the volume and quality of the training data. Once the model is well-trained, the prediction of cell performance is expected to be accurate within the range of training data. However, uncertainty remains when the fuel cell is operated under extreme conditions, such as cold start, degraded components, or unexpected scenarios that are not covered in the training data. Further efforts can be made to optimize data selection and pre-processing to avoid over-training or abnormal prediction.

### b Computing speed

**Table 10**  
Comparison of multi-dimensional PEM fuel cell performance models.

Model	Schematic	Advantages	Challenges
3D & Pseudo-3D		<ul style="list-style-type: none"> <li>• Best accuracy</li> <li>• Detailed 3D physical and electrochemical phenomena</li> <li>• Assistance to component design</li> <li>• Reduced experimental efforts</li> </ul>	<ul style="list-style-type: none"> <li>• Computationally expensive (from hours to months)</li> <li>• Accuracy relies on many transport and electrochemical properties and geometry of cell components</li> <li>• Not suitable for implementation on the available electronic control unit (ECU)</li> </ul>
2D		<ul style="list-style-type: none"> <li>• Faster calculation than 3D models (~ mins per steady-state case)</li> <li>• Reasonable accuracy under certain conditions</li> </ul>	<ul style="list-style-type: none"> <li>• Slow computational speed for ECU implementation</li> <li>• Transport phenomena in channels are simplified</li> <li>• More assumptions than 3D</li> <li>• Careful validation needed</li> </ul>
Pseudo-2D		<ul style="list-style-type: none"> <li>• Can be faster than the real time (reported to be 50% faster)</li> <li>• Reasonable accuracy under specific conditions</li> <li>• Potential direct implementation on ECU</li> </ul>	<ul style="list-style-type: none"> <li>• Requires strict validation against experimental data</li> <li>• Weak connection in the along-the-channel direction</li> </ul>
1D		<ul style="list-style-type: none"> <li>• Can be faster than the real time (reported to be 33% faster)</li> <li>• Reasonable accuracy under specific conditions</li> <li>• Potential direct implementation on ECU</li> </ul>	<ul style="list-style-type: none"> <li>• More assumptions required</li> <li>• Requires strict validation against experimental data</li> <li>• May not be able to predict the performance within the entire operational range with sufficient accuracy</li> </ul>
0D (analytical)		<ul style="list-style-type: none"> <li>• Theoretically faster than 1D models</li> <li>• System analysis and design</li> <li>• Thermodynamic analysis</li> <li>• Used for model predictive control studies</li> </ul>	<ul style="list-style-type: none"> <li>• Requires strict validation against experimental data</li> <li>• Trade-off relation between accuracy and computing speed</li> <li>• Accuracy over the entire range of operation may not be reliable</li> </ul>
0D (empirical)		<ul style="list-style-type: none"> <li>• Theoretically faster than 1D models</li> <li>• Good accuracy with proper curve fitting</li> <li>• Used for model predictive control studies</li> <li>• Direct implementation on ECU</li> </ul>	<ul style="list-style-type: none"> <li>• Requires well-structured experimental data for curve fitting to determine the unknown coefficient</li> <li>• Only valid for validated cases</li> <li>• Accuracy over the entire range of operation may not be reliable</li> </ul>
Data-driven		<ul style="list-style-type: none"> <li>• Fast calculation after training (&lt; a few seconds)</li> <li>• Excellent accuracy once properly trained</li> <li>• No requirement on the knowledge of the fuel cell design</li> <li>• No requirement on transport or electrochemical coefficients</li> </ul>	<ul style="list-style-type: none"> <li>• Algorithm and model architecture should be properly selected</li> <li>• A high volume of experimental data is required</li> <li>• Experimental data should be representative of typical operations</li> <li>• Uncertain accuracy when operating fuel cell in extreme conditions that are not trained</li> </ul>

For physics-based models, computing speed depends on the number of physical phenomena included and the accuracy required, which is inadequately investigated in literature. More incorporated phenomena and higher required accuracy mean longer computing time. Based on the available ECU, 3D and 2D models are computationally expensive for implementation, while 1D and 0D models have demonstrated the capability of direct implementation for control purposes. As can be seen in Table 9, the computing time required for 3D and 2D models varies from tens of minutes to a few months, while the pseudo-2D and 1D models are reported to be 33–50% faster than the real-time fuel cell dynamics. Technical pathways to enhance computational speed include reducing dimensionality, simplifying model formulation, ignoring non-dominant phenomena, and improving computing algorithms and resources. Further efforts can be made to evaluate the effect of these pathways on the computing speed of physics-based models.

For data-driven models, the computing speed can be enhanced by a few orders of magnitudes in comparison with physics-based models once the model is trained against sufficient experimental data, although the training time may be comparable to that of physical models. As shown in Table 9, the data-driven models only need a few seconds to estimate fuel cell behaviors after the models are well trained (the training time is rarely reported). Further studies to develop models with capabilities to predict more output variables, including voltage, temperature, and outlet reactant and product conditions, will benefit advanced system

control with limited ECU resources.

*c Balance between model accuracy and computing speed*

The implementation of physics-based fuel cell models on the ECU requires significant simplification of various transport and electrochemical phenomena. This simplification will inevitably sacrifice the modeling accuracy to some extent. Therefore, the computing speed and modeling accuracy of a fuel cell model are often in a trade-off relation. Further efforts can be made to explore the balance between modeling accuracy and computing speed for the real-time control of PEM fuel cells.

*d Aging mechanisms*

In an actual PEM fuel cell, the long-term performance can be aged due to various mechanisms, including mechanical, thermal, chemical, and electrochemical degradations [4,120–122] for all cell components, including membrane, CLs, GDLs, and bipolar plates. The major mechanical and thermal degradation of cell components arises from the structural deformation (both plastic and elastic) corresponding to the cell and stack assembly force, and the stress cycling arises from the volumetric and dimensional changes accompanying the changes in operational conditions, e.g., current density, humidity, and temperature

[177–179]. This type of degradation can be modeled through the changes in dimensions (e.g., thickness) and structure-determined parameters (e.g., porosity, effective ohmic resistance, effective diffusion coefficient, and capillary pressure) of the cell components [180], which can significantly affect the activation, ohmic, and concentration losses after a long-term operation [181]. Shen [180] developed a predictive 3D model incorporating the above aging mechanisms to evaluate the long-term performance degradation due to the cycling of assembly force, thermal, and humidity changes. The major chemical and electrochemical degradations occur because of the component corrosion caused by chemical and electrochemical reactions. The corrosion of ionomer and catalyst can be resulted from the attack of radical species (e.g., peroxide ( $\text{HO}^*$ ) and hydro peroxide ( $\text{HOO}^*$ )) resulted from anodic and cathodic chemical reactions [182,183]. The membrane thinning, which can cause a significant performance drop, can be caused by the contamination of trace metal ions (e.g.,  $\text{Cu}^{2+}$  and  $\text{Fe}^{2+}$ ) due to the corrosion of metal distribution plates or endplates [120,184]. The catalyst can lose activities due to the poisoning by the impurities in reactant gas [185,186] and the reduced electrochemical surface area (ECSA) resulted from the catalyst sintering, agglomeration, dissolution, detachment, and other degradation modes [187–190]. This type of degradation can be modeled via the changes in ohmic resistance and ECSA [38,47,191]. There exist quite a few review articles addressing the degradation mechanisms of various PEM fuel cell components [4,120,192,193]; however, incorporating these aging effects into the control-oriented models remains challenging.

#### e e Open-source database of PEM fuel cells

The role of experimental data on PEM fuel cells is mainly to validate the physics-based numerical models (including pseudo-2D, 1D numerical, OD analytical models) [8,33,46,34,39–45], to calibrate OD empirical models [16,18–20,24,25], or to train and test data-driven models [17,143,148,151,152]. The experimental data on the short- and long-term performance of PEM fuel cells may vary significantly depending on the design and manufacturing processes, and the performance data are often kept confidential with limited information available on how the data were measured for what details of the particular cell. Therefore, the availability of benchmark experimental data on PEM fuel cell performance is lacking in the open literature. Although many open-source databases have been developed for the structure and properties of molecules and solids in chemistry and material filed [157,194], such an open-source database for the fuel cells has not been available, which will be of particular interest in fuel cell modeling.

## 10. Summary and concluding remarks

The control-oriented polymer electrolyte membrane (PEM) fuel cell modeling of high computational speed and sufficient accuracy is urgently needed for the prediction of the transient and long-term performance over the entire range of operational conditions. These models can be physics-based and non-physics-based depending on whether transport and electrochemical phenomena within individual cell components are explicitly taken into account. In this review, recent progress on the development of control-oriented PEM fuel cell models, including physics-based models with reduced spatial dimensionalities (one-dimensional numerical and zero-dimensional analytical models) and non-physics-based models (zero-dimensional empirical and data-driven models), have been comprehensively scrutinized.

First, the transport and electrochemical phenomena in cell components as well as their corresponding mathematical description has been reviewed, including the conservation and transport of mass, momentum, energy, gas species, liquid and dissolved water, and charged species, as well as electrochemical kinetics, and cell potential. Based on these phenomena, numerical models with reduced spatial dimensions, which are of potential to be used for real-time control, have been reviewed and

compared. It is found that many efforts have been devoted into (i) integrating the single cell model with accessories to study the system performance, (ii) incorporating aging effects to enable the long-term performance prediction, and (iii) evaluating the computational speed. Zero-dimensional analytical and empirical models are also widely investigated in the literature in an attempt to be used for real-time control of PEM fuel cells due to their ease of implementation and fast computing speed. However, it remains challenging for these models to be used to control the PEM fuel cells over the entire range of operations.

Data-driven models, with an emphasis on artificial intelligence algorithms (including artificial neural network, fuzzy logic, support vector machine, and hybrid algorithms) have been reviewed. These models have demonstrated excellent accuracy and computational speed when the model is properly trained with a sufficiently large dataset. However, the factors affecting data-driven models rely on the amount and structure of the experimental data, which have not been thoroughly investigated so far, and further development of data-driven models with on-line learning features would be advantageous for the long-term performance prediction.

Future control-oriented modeling studies should balance between the model accuracy and computing speed based on the current limitation of computing resources. For the physics-based model, the accuracy can be improved by using experimentally determined transport coefficients or properties, validating against more indicators under more representative scenarios, and including as many physical phenomena as possible, while the computing speed can be enhanced by simplifying formulation, reducing dimensionality, simplified modeling of non-dominant phenomena (such as taking a sub-grid type of modeling approach, or even total neglect), and improving the numerical algorithm. For the data-driven models, efforts can be made to improve the training algorithm and model architecture as well as the data selection and pre-processing. These further research directions will help achieve the goals of the real-time control of PEM fuel cells with high modeling accuracy and low computing cost over the entire operational range.

## Declaration of Competing Interest

The authors declare that they have no known competing financial interests or personal relationships that could have appeared to influence the work reported in this paper.

## Acknowledgment

This work received financial support from Toyota Motor Engineering & Manufacturing North America, Inc., Toyota Motor Manufacturing Canada, and Natural Sciences and Engineering Research Council of Canada through a Collaborative Research and Development Grant with the project number of CRDPJ 543945–19.

## References

- [1] Li X. *Principles of fuel cells*. New York: Taylor & Francis Group; 2006.
- [2] Wang Y, Chen KS, Mishler J, Cho SC, Adroher XC. A review of polymer electrolyte membrane fuel cells: technology, applications, and needs on fundamental research. *Appl Energy* 2011;88:981–1007. <https://doi.org/10.1016/j.apenergy.2010.09.030>.
- [3] Jung ES, Kim H, Kwon S, Oh TH. Fuel cell system with sodium borohydride hydrogen generator for small unmanned aerial vehicles. *Int J Green Energy* 2018;15:385–92. <https://doi.org/10.1080/15435075.2018.1464924>.
- [4] Zhao J, Li X. A review of polymer electrolyte membrane fuel cell durability for vehicular applications: degradation modes and experimental techniques. *Energy Convers Manag* 2019;199:112022. <https://doi.org/10.1016/J.ENCONMAN.2019.112022>.
- [5] KoteswaraRao KV, Naga Srinivasulu G. Modeling, downsizing, and performance comparison of a fuel cell hybrid mid-size car with FCEV for urban and hill road driving cycles. *Int J Green Energy* 2019;16:115–24. <https://doi.org/10.1080/15435075.2018.1549996>.
- [6] U.S. Department of Energy. *Fuel cell technologies program multi-year research. Development, and Demonstration Plan; 2017*.

- [7] U.S. Department of Energy Fuel Cell Technologies Office. Record 18004: hydrogen R&D cost target calculation-2018 update; 2018. [https://www.hydrogen.energy.gov/pdfs/18004\\_h2\\_cost\\_target\\_calculation\\_2018.pdf](https://www.hydrogen.energy.gov/pdfs/18004_h2_cost_target_calculation_2018.pdf).
- [8] Zhao J, Li X. Oxygen transport in polymer electrolyte membrane fuel cells based on measured electrode pore structure and mass transport properties. *Energy Convers Manag* 2019;186:570–85. <https://doi.org/10.1016/j.enconman.2019.02.042>.
- [9] Daud WRW, Rosli RE, Majlan EH, Hamid SAA, Mohamed R, Husaini T. PEM fuel cell system control: a review. *Renew Energy* 2017;113:620–38. <https://doi.org/10.1016/j.renene.2017.06.027>.
- [10] Bao C, Ouyang M, Yi B. Modeling and control of air stream and hydrogen flow with recirculation in a PEM fuel cell system—I. Control-oriented modeling. *Int J Hydrog Energy* 2006;31:1879–96. <https://doi.org/10.1016/j.ijhydene.2006.02.031>.
- [11] Woo CH, Benziger JB. PEM fuel cell current regulation by fuel feed control. *Chem Eng Sci* 2007;62:957–68. <https://doi.org/10.1016/j.ces.2006.10.027>.
- [12] Wu D, Peng C, Yin C, Tang H. Review of system integration and control of proton exchange membrane fuel cells. *Electrochem Energy Rev* 2020;3:466–505. <https://doi.org/10.1007/s41918-020-00068-1>.
- [13] Das V, Padmanaban S, Venkitesamy K, Selvamuthukumar R, Blaabjerg F, Siano P. Recent advances and challenges of fuel cell based power system architectures and control - a review. *Renew Sustain Energy Rev* 2017;73:10–8. <https://doi.org/10.1016/j.rser.2017.01.148>.
- [14] Springer T, Zawodzinski T, Gottesfeld S. *Polymer electrolyte fuel cell model*. *J Electrochem Soc* 1991;138:2334–41.
- [15] Hussain MM, Baschuk JJ, Li X, Dincer I. Thermodynamic analysis of a PEM fuel cell power system. *Int J Therm Sci* 2005;44:903–11. <https://doi.org/10.1016/j.ijthermalsci.2005.02.009>.
- [16] Zhang X, Yang D, Luo M, Dong Z. Load profile based empirical model for the lifetime prediction of an automotive PEM fuel cell. *Int J Hydrog Energy* 2017;42:11868–78. <https://doi.org/10.1016/j.ijhydene.2017.02.146>.
- [17] Siswarahardjo NS, Yalcinoz T, El-Sharkh MY, Alam MS. Neural network model of 100W portable PEM fuel cell and experimental verification. *Int J Hydrog Energy* 2010;35:9104–9. <https://doi.org/10.1016/j.ijhydene.2010.05.124>.
- [18] Kim J, Lee S, Srinivasan S, Chamberlin CE. Modeling of proton exchange membrane fuel cell performance with an empirical equation. *J Electrochem Soc* 1995;142:2670–4. <https://doi.org/10.1149/1.2050072>.
- [19] Amphlett JC, Baumert RM, Mann RF, Peppley BA, Roberge PR, Harris TJ. Performance modeling of the Ballard Mark IV solid polymer electrolyte fuel cell II. Empirical model development. *J Electrochem Soc* 1995;142:9–15. <https://doi.org/10.1149/1.2043959>.
- [20] Chu D, Jiang R, Walker C. Analysis of PEM fuel cell stacks using an empirical current-voltage equation. *J Appl Electrochem* 2000;30:365–70. <https://doi.org/10.1023/A:1003905109007>.
- [21] Cownden R, Nahon M, Rosen M. Exergy analysis of a fuel cell power system for transportation applications. *Exergy Int J* 2001;1:112–21. [https://doi.org/10.1016/S1164-0235\(01\)00017-6](https://doi.org/10.1016/S1164-0235(01)00017-6).
- [22] Kazim A. Exergy analysis of a PEM fuel cell at variable operating conditions. *Energy Convers Manag* 2004;45:1949–61. <https://doi.org/10.1016/j.enconman.2003.09.030>.
- [23] Youssef ME, Al-Nadi KE, Khalil MH. Lumped model for proton exchange membrane fuel cell (PEMFC). *Int J Electrochem Sci* 2010;5:267–77.
- [24] Srinivasan S, Ticianelli EA, Derouin CR, Redondo A. Advances in solid polymer electrolyte fuel cell technology with low platinum loading electrodes. *J Power Sources* 1988;22:359–75. [https://doi.org/10.1016/0378-7753\(88\)80030-2](https://doi.org/10.1016/0378-7753(88)80030-2).
- [25] Squadrito G, Maggio G, Passalacqua E, Lufraño F, Patti A. An empirical equation for polymer electrolyte fuel cell (PEFC) behaviour. *J Appl Electrochem* 1999;29:1449–55. <https://doi.org/10.1023/A:1003890219394>.
- [26] Karimi G, Baschuk JJ, Li X. Performance analysis and optimization of PEM fuel cell stacks using flow network approach. *J Power Sources* 2005;147:162–77. <https://doi.org/10.1016/j.jpowsour.2005.01.023>.
- [27] Miotti A, di Domenico A, Guezennec YG, Rajagopalan S. Control-oriented model for an automotive PEM fuel cell system with imbedded 1+1D membrane water transport. In: Proceedings of the 2005 IEEE vehicle power and propulsion conference. IEEE; 2005. p. 611–8. <https://doi.org/10.1109/VPPC.2005.1554622>.
- [28] Musio F, Tacchi F, Omati L, Gallo Stampino P, Dotelli G, Limonta S, et al. PEMFC system simulation in MATLAB-Simulink® environment. *Int J Hydrog Energy* 2011;36:8045–52. <https://doi.org/10.1016/j.ijhydene.2011.01.093>.
- [29] Hosseinzadeh E, Rokni M, Rabbani A, Mortensen HH. Thermal and water management of low temperature proton exchange membrane fuel cell in fork-lift truck power system. *Appl Energy* 2013;104:434–44. <https://doi.org/10.1016/j.apenergy.2012.11.048>.
- [30] Hosseinzadeh E, Rokni M. Development and validation of a simple analytical model of the proton exchange membrane fuel cell (PEMFC) in a fork-lift truck power system. *Int J Green Energy* 2013;10:523–43. <https://doi.org/10.1080/15435075.2012.678525>.
- [31] Long R, Li B, Liu Z, Liu W. A hybrid system using a regenerative electrochemical cycle to harvest waste heat from the proton exchange membrane fuel cell. *Energy* 2015;93:2079–86. <https://doi.org/10.1016/j.energy.2015.09.132>.
- [32] Badduri SR, Srinivasulu GN, Rao SS. Experimental analysis of PEM fuel cell performance using lung channel design bipolar plate. *Int J Green Energy* 2019;16:1591–601. <https://doi.org/10.1080/15435075.2019.1677238>.
- [33] Falcão DS, Gomes PJ, Oliveira VB, Pinho C, Pinto A. 1D and 3D numerical simulations in PEM fuel cells. *Int J Hydrog Energy* 2011;36:12486–98. <https://doi.org/10.1016/j.ijhydene.2011.06.133>.
- [34] Li Y, Zhou Z, Liu X, Wu WT. Modeling of PEM fuel cell with thin MEA under low humidity operating condition. *Appl Energy* 2019;242:1513–27. <https://doi.org/10.1016/j.apenergy.2019.03.189>.
- [35] Pant LM, Gerhardt MR, Macauley N, Mukundan R, Borup RL, Weber AZ. Along-the-channel modeling and analysis of PEFCs at low stoichiometry: development of a 1+2D model. *Electrochim Acta* 2019;326:134963. <https://doi.org/10.1016/j.electacta.2019.134963>.
- [36] Zhang G, Bao Z, Xie B, Wang Y, Jiao K. Three-dimensional multi-phase simulation of PEM fuel cell considering the full morphology of metal foam flow field. *Int J Hydrog Energy* 2020. <https://doi.org/10.1016/j.ijhydene.2020.05.263>.
- [37] Macedo-Valencia J, Sierra JM, Figueroa-Ramírez SJ, Díaz SE, Meza M. 3D CFD modeling of a PEM fuel cell stack. *Int J Hydrog Energy* 2016;41:23425–33. <https://doi.org/10.1016/j.ijhydene.2016.10.065>.
- [38] Robin C, Gérard M, Quinaud M, d'Arbigny J, Bultel Y. Proton exchange membrane fuel cell model for aging predictions: simulated equivalent active surface area loss and comparisons with durability tests. *J Power Sources* 2016;326:417–27. <https://doi.org/10.1016/j.jpowsour.2016.07.018>.
- [39] Fuller TF, Newman J. Water and thermal management in solid-polymer-electrolyte fuel cells. *J Electrochem Soc* 1993;140:1218–25. <https://doi.org/10.1149/1.2220960>.
- [40] Nguyen TV, White RE. A water and heat management model for proton-exchange-membrane fuel cells. *J Electrochem Soc* 1993;140:2178–86. <https://doi.org/10.1149/1.2220792>.
- [41] van Bussel H, Koene FGH, Mallant R. Dynamic model of solid polymer fuel cell water management. *J Power Sources* 1998;71:218–22. [https://doi.org/10.1016/S0378-7753\(97\)02744-4](https://doi.org/10.1016/S0378-7753(97)02744-4).
- [42] Chen Q, Wang Y, Yang F, Xu H. Two-dimensional multi-physics modeling of porous transport layer in polymer electrolyte membrane electrolyzer for water splitting. *Int J Hydrog Energy* 2020;45:32984–94. <https://doi.org/10.1016/j.ijhydene.2020.09.148>.
- [43] Wang Y, Wang CY. Two-phase transients of polymer electrolyte fuel cells. *J Electrochem Soc* 2007;154:B636. <https://doi.org/10.1149/1.2734076>.
- [44] Um S, Wang C, Chen K. Computational fluid dynamics modeling of proton exchange membrane fuel cells. *J Electrochem Soc* 2000;147:4485–93.
- [45] Goshtasbi A, Pence BL, Ersal T. Computationally efficient pseudo-2D Non-isothermal modeling of polymer electrolyte membrane fuel cells with two-phase phenomena. *J Electrochem Soc* 2016;163:F1412–32. <https://doi.org/10.1149/2.0871613jes>.
- [46] Goshtasbi A, Pence BL, Ersal T. A real-time pseudo-2D bi-domain model of PEM fuel cells for automotive applications. In: Proceedings of the ASME 2017 dynamic systems and control conference; 2017. p. 1–10.
- [47] Li Y, Moriyama K, Gu W, Arisetty S, Wang CY. A One-dimensional Pt degradation model for polymer electrolyte fuel cells. *J Electrochem Soc* 2015;162:F834–42. <https://doi.org/10.1149/2.0101508jes>.
- [48] Li Y, Wang CY. Modeling of transient platinum degradation in a low Pt-loading PEFC under current cycling. *J Electrochem Soc* 2017;164:F171–9. <https://doi.org/10.1149/2.0081704jes>.
- [49] Bernardi DM, Verbrugge MW. A mathematical model of the solid-polymer-electrolyte fuel cell. *J Electrochem Soc* 1992;139:2477–91. <https://doi.org/10.1149/1.2221251>.
- [50] Weisbrod KR, Grot SA, Vanderborgh NE. Through-the-electrode model of a proton exchange membrane fuel cell. *ECS Proc Vol* 1995;1995-23:152–66. <https://doi.org/10.1149/199523.0152PV>.
- [51] Baschuk J, Li X. Modelling of polymer electrolyte membrane fuel cells with variable degrees of water flooding. *J Power Sources* 2000;86:181–96. [https://doi.org/10.1016/S0378-7753\(99\)00426-7](https://doi.org/10.1016/S0378-7753(99)00426-7).
- [52] Wöhr M, Bolwin K, Schnurnberger W, Fischer M, Neubrand W, Eigenberger G. Dynamic modelling and simulation of a polymer membrane fuel cell including mass transport limitation. *Int J Hydrog Energy* 1998;23:213–8. [https://doi.org/10.1016/S0360-3199\(97\)00043-8](https://doi.org/10.1016/S0360-3199(97)00043-8).
- [53] Falcão DS, Oliveira VB, Rangel CM, Pinho C, Pinto A. Water transport through a PEM fuel cell: a one-dimensional model with heat transfer effects. *Chem Eng Sci* 2009;64:2216–25. <https://doi.org/10.1016/j.ces.2009.01.049>. Contents.
- [54] Rowe A, Li X. Mathematical modeling of proton exchange membrane fuel cells. *J Power Sources* 2001;102:82–96. [https://doi.org/10.1016/S0378-7753\(01\)00798-4](https://doi.org/10.1016/S0378-7753(01)00798-4).
- [55] Gao F, Blunier B, Miraoui A, El Moudni A. A multiphysics dynamic 1-D model of a proton-exchange-membrane fuel-cell stack for real-time simulation. *IEEE Trans Ind Electron* 2010;57:1853–64. <https://doi.org/10.1109/TIE.2009.2021177>.
- [56] Abdin Z, Webb CJ, Gray EMA. PEM fuel cell model and simulation in Matlab-Simulink based on physical parameters. *Energy* 2016;116:1131–44. <https://doi.org/10.1016/j.energy.2016.10.033>.
- [57] Sari A, Balıkcı A, Taskin S, Aydın S. A proposed artificial neural network model for PEM fuel cells. In: Proceedings of the 2013 8th international conference on electrical and electronics engineering (ELECO). IEEE; 2013. p. 205–9. <https://doi.org/10.1109/ELECO.2013.6713832>.
- [58] Zheng Z, Petrone R, Péra MC, Hissel D, Becherif M, Pianese C, et al. A review on non-model based diagnosis methodologies for PEM fuel cell stacks and systems. *Int J Hydrog Energy* 2013;38:8914–26. <https://doi.org/10.1016/j.ijhydene.2013.04.007>.
- [59] Yin Y, Wang X, Zhang J, Shanguan X, Qin Y. Influence of sloping baffle plates on the mass transport and performance of PEMFC. *Int J Energy Res* 2018;1–13. <https://doi.org/10.1002/ER.4306>.
- [60] Heidary H, Kermani MJ, Dabir B. Influences of bipolar plate channel blockages on PEM fuel cell performances. *Energy Convers Manag* 2016;124:51–60. <https://doi.org/10.1016/j.enconman.2016.06.043>.

- [61] Jiao K, Li X. Water transport in polymer electrolyte membrane fuel cells. *Prog Energy Combust Sci* 2011;37:221–91. <https://doi.org/10.1016/j.pecs.2010.06.002>.
- [62] Wang CY. Fundamental models for fuel cell engineering. *Chem Rev* 2004;104:4727–66. <https://doi.org/10.1021/CR020718S>.
- [63] Kim GS, Sui PC, Shah AA, Djilali N. Reduced-dimensional models for straight-channel proton exchange membrane fuel cells. *J Power Sources* 2010;195:3240–9. <https://doi.org/10.1016/j.jpowsour.2009.11.110>.
- [64] Luo Y, Jiao K. Cold start of proton exchange membrane fuel cell. *Prog Energy Combust Sci* 2018;64:29–61. <https://doi.org/10.1016/j.pecs.2017.10.003>.
- [65] Zhang G, Fan L, Sun J, Jiao K. A 3D model of PEMFC considering detailed multiphase flow and anisotropic transport properties. *Int J Heat Mass Transf* 2017;115:714–24. <https://doi.org/10.1016/j.ijheatmasstransfer.2017.07.102>.
- [66] Ye Q, Van NT. Three-dimensional simulation of liquid water distribution in a PEMFC with experimentally measured capillary functions. *J Electrochem Soc* 2007;154:B1242. <https://doi.org/10.1149/1.2783775>.
- [67] Wu H, Li X, Berg P. On the modeling of water transport in polymer electrolyte membrane fuel cells. *Electrochim Acta* 2009;54:6913–27. <https://doi.org/10.1016/j.electacta.2009.06.070>.
- [68] Xing L, Mamlouk M, Kumar R, Scott K. Numerical investigation of the optimal Nafion® ionomer content in cathode catalyst layer: an agglomerate two-phase flow modelling. *Int J Hydrog Energy* 2014;39:9087–104. <https://doi.org/10.1016/j.ijhydene.2014.03.225>.
- [69] Wu H, Li X, Berg P. Numerical analysis of dynamic processes in fully humidified PEM fuel cells. *Int J Hydrog Energy* 2007;32:2022–31. <https://doi.org/10.1016/j.ijhydene.2006.09.046>.
- [70] Kulikovskiy AA. Quasi-3D modeling of water transport in polymer electrolyte fuel cells. *J Electrochem Soc* 2003;150:A1432–9. <https://doi.org/10.1149/1.1611489>.
- [71] Hinatsu JT, Mizuhata M, Takenaka H. Water uptake of perfluorosulfonic acid membranes from liquid water and water vapor. *J Electrochem Soc* 1994;141:1493–8. <https://doi.org/10.1149/1.2054951>.
- [72] Wang Y, Wang CY. Transient analysis of polymer electrolyte fuel cells. *Electrochim Acta* 2005;50:1307–15. <https://doi.org/10.1016/j.electacta.2004.08.022>.
- [73] Yan Q, Toghiani H, Lee YW, Liang K, Causey H. Effect of sub-freezing temperatures on a PEM fuel cell performance, startup and fuel cell components. *J Power Sources* 2006;160:1242–50. <https://doi.org/10.1016/j.jpowsour.2006.02.075>.
- [74] Liu H, Si D, Ding H, Wang S, Zhang J, Liu Y. Cold start capability and durability of electrospun catalyst layer for proton exchange membrane fuel cell. *Int J Hydrog Energy* 2020;1–10. <https://doi.org/10.1016/j.ijhydene.2020.06.032>.
- [75] Carryg NB, Pant LM, Mitra S, Secanell M. Knudsen diffusivity and permeability of PEMFC microporous coated gas diffusion layers for different polytetrafluoroethylene loadings. *J Electrochem Soc* 2013;160:F81–9. <https://doi.org/10.1149/2.036302jes>.
- [76] Park J. Serial compression effects on porosity, diffusion, permeability, and water droplet contact angle of the gas diffusion layer in polymer electrolyte membrane fuel cells. Serial compression effects on porosity, diffusion, permeability, and water droplet contact angle of the gas diffusion layer in polymer electrolyte membrane fuel cells. University of Waterloo; 2020.
- [77] Zhao J, Shahgaldi S, Alaefour I, Xu Q, Li X. Gas permeability of catalyzed electrodes in polymer electrolyte membrane fuel cells. *Appl Energy* 2018;209:203–10. <https://doi.org/10.1016/j.apenergy.2017.10.087>.
- [78] Wu HW. A review of recent development: transport and performance modeling of PEM fuel cells. *Appl Energy* 2016;165:81–106. <https://doi.org/10.1016/j.apenergy.2015.12.075>.
- [79] Yang Z, Du Q, Huo S, Jiao K. Effect of membrane electrode assembly design on the cold start process of proton exchange membrane fuel cells. *Int J Hydrog Energy* 2017;42:25372–87. <https://doi.org/10.1016/j.ijhydene.2017.08.106>.
- [80] Zamel N, Li X. Effective transport properties for polymer electrolyte membrane fuel cells -with a focus on the gas diffusion layer. *Prog Energy Combust Sci* 2013;39:111–46.
- [81] Zhao J, Shahgaldi S, Alaefour I, Yang S, Li X. Pore structure and effective diffusion coefficient of catalyzed electrodes in polymer electrolyte membrane fuel cells. *Int J Hydrog Energy* 2018;43:3776–85. <https://doi.org/10.1016/j.ijhydene.2018.01.019>.
- [82] Wu H, Berg P, Li X. Non-isothermal transient modeling of water transport in PEM fuel cells. *J Power Sources* 2007;165:232–43. <https://doi.org/10.1016/j.jpowsour.2006.11.061>.
- [83] Tsushima S, Hirai S. *In situ* diagnostics for water transport in proton exchange membrane fuel cells. *Prog Energy Combust Sci* 2011;37:204–20. <https://doi.org/10.1016/j.pecs.2010.06.001>.
- [84] Wu H, Berg P, Li X. Steady and unsteady 3D non-isothermal modeling of PEM fuel cells with the effect of non-equilibrium phase transfer. *Appl Energy* 2010;87:2778–84. <https://doi.org/10.1016/j.apenergy.2009.06.024>.
- [85] Zhang G, Jiao K. Multi-phase models for water and thermal management of proton exchange membrane fuel cell: a review. *J Power Sources* 2018;391:120–33. <https://doi.org/10.1016/j.jpowsour.2018.04.071>.
- [86] Kumbur EC, Sharp KV, Mench MM. Validated Leverett approach for multiphase flow in PEFC diffusion media: III. Temperature effect and unified approach. *J Electrochem Soc* 2007;154:B1315. <https://doi.org/10.1149/1.2784286>.
- [87] Leverett MC. Capillary behavior in porous solids. *Transac AIME* 1941;142:152–69. <https://doi.org/10.2118/941152-g>.
- [88] Newman JS, Thomas-Alyea KE. *Electrochemical systems. Electrochemical systems*. 3rd ed. New Jersey: Hoboken: John Wiley & Sons; 2012.
- [89] Karimi G, Li X. Electroosmotic flow through polymer electrolyte membranes in PEM fuel cells. *J Power Sources* 2005;140:1–11. <https://doi.org/10.1016/j.jpowsour.2004.08.018>.
- [90] Baschuk JJ, Li X. Modeling of ion and water transport in the polymer electrolyte membrane of PEM fuel cells. *Int J Hydrog Energy* 2010;35:5095–103. <https://doi.org/10.1016/j.ijhydene.2009.10.032>.
- [91] Yang Z, Du Q, Jia Z, Yang C, Xuan J, Jiao K. A comprehensive proton exchange membrane fuel cell system model integrating various auxiliary subsystems. *Appl Energy* 2019;256:113959. <https://doi.org/10.1016/j.apenergy.2019.113959>.
- [92] Akroot A, Ekici Ö, Köksal M. Process modeling of an automotive pem fuel cell system. *Int J Green Energy* 2019;16:778–88. <https://doi.org/10.1080/15435075.2019.1641105>.
- [93] Zhou J, Shukla S, Putz A, Secanell M. Analysis of the role of the microporous layer in improving polymer electrolyte fuel cell performance. *Electrochim Acta* 2018;268:366–82. <https://doi.org/10.1016/j.electacta.2018.02.100>.
- [94] Qin Y, Yin Y, Jiao K, Du Q. Effects of needle orientation and gas velocity on water transport and removal in a modified PEMFC gas flow channel having a hydrophilic needle. *Int J Energy Res* 2018;1–12. <https://doi.org/10.1002/er.4116>.
- [95] Niu Z, Wu J, Wang Y, Jiao K. Investigating the in-/through-plane effective diffusivities of dry and partially-saturated gas diffusion layers. *J Electrochem Soc* 2018;165:F986–93. <https://doi.org/10.1149/2.119181jes>.
- [96] Yin Y, Wang X, Shanguan X, Zhang J, Qin Y. Numerical investigation on the characteristics of mass transport and performance of PEMFC with baffle plates installed in the flow channel. *Int J Hydrog Energy* 2018;43:8048–62. <https://doi.org/10.1016/j.ijhydene.2018.03.037>.
- [97] Huang J, Li Z, Zhang J. Review of characterization and modeling of polymer electrolyte fuel cell catalyst layer: the blessing and curse of ionomer. *Front Energy* 2017;11:334–64. <https://doi.org/10.1007/s11708-017-0490-6>.
- [98] Khan SS, Shareef H, Mutlag AH. Dynamic temperature model for proton exchange membrane fuel cell using online variations in load current and ambient temperature. *Int J Green Energy* 2019;16:361–70. <https://doi.org/10.1080/15435075.2018.1564141>.
- [99] Dickinson E, Hinds G. The Butler-Volmer equation for polymer electrolyte membrane fuel cell (PEMFC) electrode kinetics: a critical discussion. *J Electrochem Soc* 2019;166:F221–31. <https://doi.org/10.1149/2.0361904jes>.
- [100] Guidelli R, Compton RG, Felici JM, Gileadi E, Lipkowsky J, Schmickler W, et al. Definition of the transfer coefficient in electrochemistry (IUPAC recommendations 2014). *Pure Appl Chem* 2014;86:259–62. <https://doi.org/10.1515/pac-2014-5025>.
- [101] Parsons R. Electrode reaction orders, transfer coefficients and rate constants: Amplification of definitions and recommendations for publication of parameters. *Electrochimica Acta* 1981;26:1869–74. [https://doi.org/10.1016/0013-4686\(81\)85177-8](https://doi.org/10.1016/0013-4686(81)85177-8).
- [102] Barbir F. Fuel Cell Electrochemistry. *PEM Fuel Cells* 2005:33–72. <https://doi.org/10.1016/b978-012078142-3/50004-5>.
- [103] Jiang Y, Yang Z, Jiao K, Du Q. Sensitivity analysis of uncertain parameters based on an improved proton exchange membrane fuel cell analytical model. *Energy Convers Manag* 2018;164:639–54. <https://doi.org/10.1016/j.enconman.2018.03.002>.
- [104] Qin Y, Du Q, Fan M, Chang Y, Yin Y. Study on the operating pressure effect on the performance of a proton exchange membrane fuel cell power system. *Energy Convers Manag* 2017;142:357–65. <https://doi.org/10.1016/j.enconman.2017.03.035>.
- [105] Zhao J. Catalyst layers in polymer electrolyte membrane fuel cells: formation, characterization and performance. University of Waterloo; 2019.
- [106] Hussaini IS, Wang CY. Measurement of relative permeability of fuel cell diffusion media. *J Power Sources* 2010;195:3830–40.
- [107] Weber AZ, Borup RL, Darling RM, Das PK, Dursch TJ, Gu W, et al. A critical review of modeling transport phenomena in polymer-electrolyte fuel cells. *J Electrochem Soc* 2014;161:F1254–99. <https://doi.org/10.1149/2.0751412jes>.
- [108] Kusoglu A, Weber AZ. New insights into perfluorinated sulfonic-acid ionomers. *Chem Rev* 2017;117:987–1104. <https://doi.org/10.1021/acs.chemrev.6b00159>.
- [109] Vetter R, Schumacher JO. Experimental parameter uncertainty in proton exchange membrane fuel cell modeling. part I: scatter in material parameterization. *J Power Sources* 2019;438:227018. <https://doi.org/10.1016/j.jpowsour.2019.227018>.
- [110] Vetter R, Schumacher JO. Experimental parameter uncertainty in proton exchange membrane fuel cell modeling. part II: sensitivity analysis and importance ranking. *J Power Sources* 2019;439:126529. <https://doi.org/10.1016/j.jpowsour.2019.04.057>.
- [111] Zamel N, Li X, Shen J. Correlation for the effective gas diffusion coefficient in carbon paper diffusion media. *Energy Fuels* 2009;23:6070–8.
- [112] Ryan EM, Mukherjee PP. Mesoscale modeling in electrochemical devices—a critical perspective. *Prog Energy Combust Sci* 2019;71:118–42. <https://doi.org/10.1016/j.pecs.2018.11.002>.
- [113] Goswami N, Mistry AN, Grunewald JB, Fuller TF, Mukherjee PP. Corrosion-induced microstructural variability affects transport-kinetics interaction in PEM fuel cell catalyst layers. *J Electrochem Soc* 2020;167:084519. <https://doi.org/10.1149/1945-7111/ab927c>.
- [114] Mukherjee PP, Kang Q, Wang CY. Pore-scale modeling of two-phase transport in polymer electrolyte fuel cells—progress and perspective. *Energy Environ Sci* 2011;4:346–69. <https://doi.org/10.1039/b926077c>.
- [115] Grunewald JB, Mistry AN, Verma A, Goswami N, Mukherjee PP, Fuller TF. Mesoscale physics in the catalyst layer of proton exchange membrane fuel cells. *J Electrochem Soc* 2019;166:F3089–92. <https://doi.org/10.1149/2.0111907jes>.

- [116] Shojaefard MH, Molaieamaneh GR, Nazemian M, Moqaddari MR. A review on microstructure reconstruction of PEM fuel cells porous electrodes for pore scale simulation. *Int J Hydrog Energy* 2016;41:20276–93. <https://doi.org/10.1016/j.ijhydene.2016.08.179>.
- [117] Sabharwal M, Pant LM, Putz A, Susac D, Jankovic J, Secanell M. Analysis of catalyst layer microstructures: from imaging to performance. *Fuel Cells* 2016;16:734–53. <https://doi.org/10.1002/fuce.201600008>.
- [118] Edwards RL, Demuren A. Regression analysis of PEM fuel cell transient response. *Int J Energy Environ Eng* 2016;7:329–41. <https://doi.org/10.1007/s40095-016-0209-1>.
- [119] Mueller F, Brouwer J, Kang S, Kim HS, Min K. Quasi-three dimensional dynamic model of a proton exchange membrane fuel cell for system and controls development. *J Power Sources* 2007;163:814–29. <https://doi.org/10.1016/j.jpowsour.2006.09.089>.
- [120] Wu J, Yuan XZ, Martin JJ, Wang H, Zhang J, Shen J, et al. A review of PEM fuel cell durability: degradation mechanisms and mitigation strategies. *J Power Sources* 2008;184:104–19. <https://doi.org/10.1016/j.jpowsour.2008.06.006>.
- [121] Ren P, Pei P, Li Y, Wu Z, Chen D, Huang S. Degradation mechanisms of proton exchange membrane fuel cell under typical automotive operating conditions. *Prog Energy Combust Sci* 2020;80. <https://doi.org/10.1016/j.pecs.2020.100859>.
- [122] Novotny P, Tomas M, Nemeč T, Kullova L, Marsik F. On/off cycling test of low-temperature PEM fuel cell at fully humidified conditions. *Int J Green Energy* 2019;16:1189–95. <https://doi.org/10.1080/15435075.2019.1671394>.
- [123] Shamardina O, Chertovich A, Kulikovskiy AA, Khokhlov AR. A simple model of a high temperature PEM fuel cell. *Int J Hydrog Energy* 2010;35:9954–62. <https://doi.org/10.1016/j.ijhydene.2009.11.012>.
- [124] Chupin S, Colinart T, Didierjean S, Dubé Y, Agbossou K, Maranzana G, et al. Numerical investigation of the impact of gas and cooling flow configurations on current and water distributions in a polymer membrane fuel cell through a pseudo-two-dimensional diphasic model. *J Power Sources* 2010;195:5213–27. <https://doi.org/10.1016/j.jpowsour.2010.03.027>.
- [125] Yang Z, Du Q, Jia Z, Yang C, Jiao K. Effects of operating conditions on water and heat management by a transient multi-dimensional PEMFC system model. *Energy* 2019;183:162–476. <https://doi.org/10.1016/j.energy.2019.06.148>.
- [126] Goshtasbi A, Chen J, Waldecker JR, Hirano S, Ersal T. On parameterizing PEM fuel cell models. In: *Proceedings of the 2019 American control conference (ACC)*; 2019. p. 903–8.
- [127] Timovan R, Giurgea S. Efficiency improvement of a PEMFC power source by optimization of the air management. *Int J Hydrog Energy* 2012;37:7745–56. <https://doi.org/10.1016/j.ijhydene.2012.02.029>.
- [128] Hong L, Chen J, Liu Z, Huang L, Wu Z. A nonlinear control strategy for fuel delivery in PEM fuel cells considering nitrogen permeation. *Int J Hydrog Energy* 2017;42:1565–76. <https://doi.org/10.1016/j.ijhydene.2016.07.240>.
- [129] Promislow K, St-Pierre J, Wetton B. A simple, analytic model of polymer electrolyte membrane fuel cell anode recirculation at operating power including nitrogen crossover. *J Power Sources* 2011;196:10050–6. <https://doi.org/10.1016/j.jpowsour.2011.08.070>.
- [130] Matraji I, Laghrouche S, Wack M. Pressure control in a PEM fuel cell via second order sliding mode. *Int J Hydrog Energy* 2012;37:16104–16. <https://doi.org/10.1016/j.ijhydene.2012.08.007>.
- [131] Danzer MA, Wittmann SJ, Hofer EP. Prevention of fuel cell starvation by model predictive control of pressure, excess ratio, and current. *J Power Sources* 2009;190:86–91. <https://doi.org/10.1016/j.jpowsour.2008.12.089>.
- [132] Shan Y, Choe SY. A high dynamic PEM fuel cell model with temperature effects. *J Power Sources* 2005;145:30–9. <https://doi.org/10.1016/J.JPOWSOUR.2004.12.033>.
- [133] Jung JH, Ahmed S, Enjeti P. PEM fuel cell stack model development for real-time simulation applications. *IEEE Trans Ind Electron* 2011;58:4217–31. <https://doi.org/10.1109/TIE.2010.2098365>.
- [134] Grubb WT, Niedrach LW. Batteries with solid ion-exchange membrane electrolytes II. low-temperature hydrogen-oxygen fuel cells. *J Electrochem Soc* 1960;107:131–5.
- [135] Ticianelli EA, Derouin CR, Redondo A, Srinivasan S. Methods to advance technology of proton exchange membrane fuel cells. *J Electrochem Soc* 1983;135:2209–14. <https://doi.org/10.1149/1.2096240>.
- [136] M.S. Wilson Membrane catalyst layer for fuel cells. No. US 5234777. Los Alamos National Lab.(LANL), Los Alamos, NM (United States), 1993.
- [137] Baker DR, Wieser C, Neyerlin KC, Murphy MW. The use of limiting current to determine transport resistance in PEM fuel cells. *ECS Trans* 2019;3:989–99. <https://doi.org/10.1149/1.2356218>.
- [138] Chaparro AM, Gallardo B, Folgado MA, Martín AJ, Daza L. PEMFC electrode preparation by electrospray: optimization of catalyst load and ionomer content. *Catal Today* 2009;143:237–41. <https://doi.org/10.1016/j.cattod.2008.12.003>.
- [139] Liu M, Wang C, Xie F, Mao Z. A polymer electrolyte fuel cell life test using accelerating degradation technique. *Int J Hydrog Energy* 2013;38:11011–6. <https://doi.org/10.1016/j.ijhydene.2013.02.086>.
- [140] Chong L, Wen J, Kubal J, Sen FG, Zou J, Greeley J, et al. Ultralow-loading platinum-cobalt fuel cell catalysts derived from imidazolate frameworks. *Science* 2018;362:1276–81. <https://doi.org/10.1126/science.aau0630>.
- [141] Zhang G, Wu L, Jiao K, Tian P, Wang B, Wang Y, et al. Optimization of porous media flow field for proton exchange membrane fuel cell using a data-driven surrogate model. *Energy Convers Manag* 2020;226:113513. <https://doi.org/10.1016/j.enconman.2020.113513>.
- [142] Tian P, Liu X, Luo K, Li H, Wang Y. Deep learning from three-dimensional multiphysics simulation in operational optimization and control of polymer electrolyte membrane fuel cell for maximum power. *Appl Energy* 2021;288:116632. <https://doi.org/10.1016/j.apenergy.2021.116632>.
- [143] Ou S, Achenin LEK. A hybrid neural network model for PEM fuel cells. *J Power Sources* 2005;140:319–30. <https://doi.org/10.1016/J.JPOWSOUR.2004.08.047>.
- [144] Ma R, Yang T, Breaz E, Li Z, Briois P, Gao F. Data-driven proton exchange membrane fuel cell degradation prediction through deep learning method. *Appl Energy* 2018;231:102–15. <https://doi.org/10.1016/j.apenergy.2018.09.111>.
- [145] Jaafra Y, Luc Laurent J, Deruyver A, Saber Naceur M. Reinforcement learning for neural architecture search: a review. *Image Vis Comput* 2019;89:57–66. <https://doi.org/10.1016/j.imavis.2019.06.005>.
- [146] Chávez-Ramírez AU, Muñoz-Guerrero R, Durón-Torres SM, Ferraro M, Brunaccini G, Sergi F, et al. High power fuel cell simulator based on artificial neural network. *Int Journal Hydrog Energy* 2010;35:12125–33. <https://doi.org/10.1016/j.ijhydene.2009.09.071>.
- [147] Chiang YM, Chang LC, Chang FJ. Comparison of static-feedforward and dynamic-feedback neural networks for rainfall-runoff modeling. *J Hydrol* 2004;290:297–311. <https://doi.org/10.1016/j.jhydrol.2003.12.033>.
- [148] Hatti M, Tioussi M, Nouibat W. Static modelling by neural networks of a PEM fuel cell. In: *Proceedings of the IECON (industrial electronics conference)*. IEEE Computer Society; 2006. p. 2121–6. <https://doi.org/10.1109/IECON.2006.347589>.
- [149] HATTI M, TIoussi M. Dynamic neural network controller model of PEM fuel cell system. *Int J Hydrog Energy* 2009;34:5015–21. <https://doi.org/10.1016/J.IJHYDENE.2008.12.094>.
- [150] Vichard L, Harel F, Ravey A, Venet P, Hissel D. Degradation prediction of PEM fuel cell based on artificial intelligence. *Int J Hydrog Energy* 2020. <https://doi.org/10.1016/j.ijhydene.2020.03.209>.
- [151] Tekin M, Hissel D, Pera MC, Kauffmann JM. Energy-management strategy for embedded fuel-cell systems using fuzzy logic. *IEEE Trans Ind Electron* 2007;54:595–603.
- [152] Hissel D, Candusso D, Harel F. Fuzzy-clustering durability diagnosis of polymer electrolyte fuel cells dedicated to transportation applications. *IEEE Trans Veh Technol* 2007;56:2414–20. <https://doi.org/10.1109/TVT.2007.898389>.
- [153] Zou W, Froning D, Lu XJ, Lehnert W. An online spatiotemporal temperature model for high temperature polymer electrolyte fuel cells. *Energy Convers Manag* 2019;199:111974. <https://doi.org/10.1016/J.ENCONMAN.2019.111974>.
- [154] Wu Y, Breaz E, Gao F, Paire D, Miraoui A. Nonlinear performance degradation prediction of proton exchange membrane fuel cells using relevance vector machine. *IEEE Trans Energy Convers* 2016;31:1570–82. <https://doi.org/10.1109/TEC.2016.2582531>.
- [155] Wu Y, Breaz E, Gao F, Miraoui A. A modified relevance vector machine for PEM fuel-cell stack aging prediction. *IEEE Trans Ind Appl* 2016;52:2573–81. <https://doi.org/10.1109/TIA.2016.2524402>.
- [156] Raissi M, Perdikaris P, Karniadakis GE. Physics-informed neural networks: A deep learning framework for solving forward and inverse problems involving nonlinear partial differential equations. *J Comput Phys* 2019;378:686–707. <https://doi.org/10.1016/j.jcp.2018.10.045>.
- [157] Wang Y, Seo B, Wang B, Zamel N, Jiao K, Adroher XC. Fundamentals, materials, and machine learning of polymer electrolyte membrane Fuel Cell Technology. *Energy AI* 2020;1:74. <https://doi.org/10.1016/j.egyai.2020.100014>.
- [158] Doan NAK, Polifke W, Magri L. Physics-informed echo state networks. *J Comput Sci* 2020;47:101237. <https://doi.org/10.1016/j.jocs.2020.101237>.
- [159] Zhang R, Liu Y, Sun H. Physics-informed multi-LSTM networks for metamodelling of nonlinear structures. *Comput Methods Appl Mech Eng* 2020;369:113226. <https://doi.org/10.1016/j.cma.2020.113226>.
- [160] Peherstorfer B, Willcox K. Dynamic data-driven reduced-order models. *Comput Method Appl Mech Eng* 2015;291:21–41. <https://doi.org/10.1016/j.cma.2015.03.018>.
- [161] Pawar S, Ahmed SE, San O, Rasheed A. Data-driven recovery of hidden physics in reduced order modeling of fluid flows. *Phys Fluids* 2020;32. <https://doi.org/10.1063/5.0002051>.
- [162] Koronaki ED, Nikas AM, Boudouvis AG. A data-driven reduced-order model of nonlinear processes based on diffusion maps and artificial neural networks. *Chem Eng J* 2020;397:125475. <https://doi.org/10.1016/j.cej.2020.125475>.
- [163] Li Z, Oubib R, Hissel D, Giurgea S. Data-driven diagnosis of PEM fuel cell: a comparative study. *Control Eng Pract* 2014;28:1–12. <https://doi.org/10.1016/j.conengprac.2014.02.019>.
- [164] Lei Y, Le CT, Mebane DS, Wen YH. Reduced-order model for microstructure evolution prediction in the electrodes of solid oxide fuel cell with dynamic discrepancy reduced modeling. *J Power Sources* 2019;416:37–49. <https://doi.org/10.1016/j.jpowsour.2019.01.046>.
- [165] Masoudi R, McPhee J. Application of Karhunen–Loève decomposition and piecewise linearization to a physics-based battery model. *Electrochim Acta* 2021;365:137093. <https://doi.org/10.1016/j.electacta.2020.137093>.
- [166] Xiao D, Fang F, Buchan AG, Pain CC, Navon IM, Muggeridge A. Non-intrusive reduced order modelling of the Navier-Stokes equations. *Comput Methods Appl Mech Eng* 2015;293:522–41. <https://doi.org/10.1016/j.cma.2015.05.015>.
- [167] Mellit A, Kalogirou SA. Artificial intelligence techniques for photovoltaic applications: a review. *Prog Energy Combust Sci* 2008;34:574–632. <https://doi.org/10.1016/j.pecs.2008.01.001>.
- [168] Mellit A, Kalogirou SA, Hontoria L, Shaari S. Artificial intelligence techniques for sizing photovoltaic systems: a review. *Renew Sustain Energy Rev* 2009;13:406–19. <https://doi.org/10.1016/j.rser.2008.01.006>.
- [169] Kalogirou SA. Artificial intelligence for the modeling and control of combustion processes: a review. *Prog Energy Combust Sci* 2003;29:515–66. [https://doi.org/10.1016/S0360-1285\(03\)00058-3](https://doi.org/10.1016/S0360-1285(03)00058-3).



- [170] Silva RE, Gouriveau R, Jemei S, Hissel D, Boulon L, Agbossou K, et al. Proton exchange membrane fuel cell degradation prediction based on Adaptive Neuro-Fuzzy Inference Systems. *Int J Hydrog Energy* 2014;39:11128–44. <https://doi.org/10.1016/j.ijhydene.2014.05.005>.
- [171] Wang B, Zhang G, Wang H, Xuan J, Jiao K. Multi-physics-resolved digital twin of proton exchange membrane fuel cells with a data-driven surrogate model. *Energy AI* 2020;1:100004. <https://doi.org/10.1016/j.egyai.2020.100004>.
- [172] Ferreira RB, Falcão DS, Oliveira VB, Pinto A. 1D + 3D two-phase flow numerical model of a proton exchange membrane fuel cell. *Appl Energy* 2017;203:474–95. <https://doi.org/10.1016/j.apenergy.2017.06.048>.
- [173] Park J, Li X. Effect of flow and temperature distribution on the performance of a PEM fuel cell stack. *J Power Sources* 2006;162:444–59. <https://doi.org/10.1016/J.JPOWSOUR.2006.07.030>.
- [174] Wang B, Xie B, Xuan J, Jiao K. AI-based optimization of PEM fuel cell catalyst layers for maximum power density via data-driven surrogate modeling. *Energy Convers Manag* 2020;205:112460. <https://doi.org/10.1016/j.enconman.2019.112460>.
- [175] Zhong ZD, Zhu XJ, Cao GY. Modeling a PEMFC by a support vector machine. *J Power Sources* 2006;160:293–8. <https://doi.org/10.1016/j.jpowsour.2006.01.040>.
- [176] Robert Bosch GmbH. Bosch Mobility Solutions. <https://www.bosch-mobility-solutions.com/en/solutions/powertrain/fuel-cell-electric/fuel-cell-control-unit/> (accessed September 10, 2021).
- [177] Chang Y, Liu J, Li R, Zhao J, Qin Y, Zhang J, et al. Effect of humidity and thermal cycling on the catalyst layer structural changes in polymer electrolyte membrane fuel cells. *Energy Convers Manag* 2019;189:24–32. <https://doi.org/10.1016/J.ENCONMAN.2019.03.066>.
- [178] Chang Y, Zhao J, Shahgaldi S, Qin Y, Yin Y, Li X. Modelling of mechanical microstructure changes in the catalyst layer of a polymer electrolyte membrane fuel cell. *Int J Hydrog Energy* 2018;1–13. <https://doi.org/10.1016/j.ijhydene.2018.10.157>.
- [179] Zhao J, Shahgaldi S, Li X, Liu ZS. Experimental observations of microstructure changes in the catalyst layers of proton exchange membrane fuel cells under wet-dry cycles. *J Electrochem Soc* 2018;165:F3337–45. <https://doi.org/10.1149/2.0391806jes>.
- [180] Shen Y. Mechanical degradation of membrane electrode assemblies in proton exchange membrane fuel cells. *Mechanical degradation of membrane electrode assemblies in proton exchange membrane fuel cells*. University of Waterloo; 2017.
- [181] Zhao J, Shahgaldi S, Ozden A, Alaefour IE, Li X, Hamdullahpur F. Effect of catalyst deposition on electrode structure, mass transport and performance of polymer electrolyte membrane fuel cells. *Appl Energy* 2019;255:113802. <https://doi.org/10.1016/J.APENERGY.2019.113802>.
- [182] Ramaswamy N, Arruda TM, Wen W, Hakim N, Saha M, Gullá A, et al. Enhanced activity and interfacial durability study of ultra low Pt based electrocatalysts prepared by ion beam assisted deposition (IBAD) method. *Electrochim Acta* 2009;54:6756–66. <https://doi.org/10.1016/J.ELECTACTA.2009.06.040>.
- [183] Mittal VO, Kunz HR, Fenton JM. Membrane degradation mechanisms in PEMFCs. *J Electrochem Soc* 2007;154:B652–6. <https://doi.org/10.1149/1.2734869>.
- [184] Huang X, Solasi R, Zou Y, Feshler M, Reifsnider K, Condit D, et al. Mechanical endurance of polymer electrolyte membrane and PEM fuel cell durability. *J Polym Sci Part B Polym Phys* 2006;44:2346–57. <https://doi.org/10.1002/polb.20863>.
- [185] Valdés-López VF, Mason T, Shearing PR, Brett DJL. Carbon monoxide poisoning and mitigation strategies for polymer electrolyte membrane fuel cells -a review. *Prog Energy Combust Sci* 2020;79. <https://doi.org/10.1016/j.pecs.2020.100842>.
- [186] Zamel N, Li X. Effect of contaminants on polymer electrolyte membrane fuel cells. *Prog Energy Combust Sci* 2011;37:292–329. <https://doi.org/10.1016/j.pecs.2010.06.003>.
- [187] Sharma R, Andersen SM. An opinion on catalyst degradation mechanisms during catalyst support focused accelerated stress test (AST) for proton exchange membrane fuel cells (PEMFCs). *Appl Catal B Environ* 2018;239:636–43. <https://doi.org/10.1016/J.APCATB.2018.08.045>.
- [188] Chung CG, Kim L, Sung YW, Lee J, Chung JS. Degradation mechanism of electrocatalyst during long-term operation of PEMFC. *Int J Hydrog Energy* 2009;34:8974–81. <https://doi.org/10.1016/j.ijhydene.2009.08.094>.
- [189] Zhang Y, Chen S, Wang Y, Ding W, Wu R, Li L, et al. Study of the degradation mechanisms of carbon-supported platinum fuel cells catalyst via different accelerated stress test. *J Power Sources* 2015;273:62–9. <https://doi.org/10.1016/J.JPOWSOUR.2014.09.012>.
- [190] Wang C, Zhao Q, Zhou X, Wang J, Tang Y. Degradation characteristics of membrane electrode assembly under drive cycle test protocol. *Int J Green Energy* 2019;16:789–95. <https://doi.org/10.1080/15435075.2019.1641712>.
- [191] Baschuk JJ, Li X. Modelling CO poisoning and O<sub>2</sub> bleeding in a PEM fuel cell anode. *Int J Energy Res* 2003;27:1095–116. <https://doi.org/10.1002/er.934>.
- [192] Yousfi-Steiner N, Moçotéguy P, Candusso D, Hissel D. A review on polymer electrolyte membrane fuel cell catalyst degradation and starvation issues: causes, consequences and diagnostic for mitigation. *J Power Sources* 2009;194:130–45. <https://doi.org/10.1016/j.jpowsour.2009.03.060>.
- [193] Yuan XZ, Zhang S, Sun JC, Wang H. A review of accelerated conditioning for a polymer electrolyte membrane fuel cell. *J Power Sources* 2011;196:9097–106. <https://doi.org/10.1016/J.JPOWSOUR.2011.06.098>.
- [194] Butler KT, Davies DW, Cartwright H, Isayev O, Walsh A. Machine learning for molecular and materials science. *Nature* 2018;559:547–55. <https://doi.org/10.1038/s41586-018-0337-2>.